Engineering Intratumoral Cytokine Therapies for Cancer

by

Emi A. Lutz

B.S. Bioengineering
University of Washington, Seattle, 2016

SUBMITTED TO THE DEPARTMENT OF BIOLOGICAL ENGINEERING IN PARTIAL FULFILLMENT OF THE REQUIREMENTS FOR THE DEGREE OF

DOCTOR OF PHILOSOPHY IN BIOLOGICAL ENGINEERING
AT THE
MASSACHUSETTS INSTITUTE OF TECHNOLOGY

SEPTEMBER 2022

Signature of Author: _____
Emi Alexandra Lutz
Department of Biological Engineering, MIT
June 21, 2022

Certified by: _____
K. Dane Wittrup, PhD
C. P. Dubbs Professor of Chemical Engineering and Biological Engineering, MIT
Thesis Advisor

Accepted by: _____
Darrell J. Irvine, PhD
Professor of Materials Science & Engineering and Biological Engineering, MIT
Thesis Committee Chair

Thesis Committee Members

K. Dane Wittrup, PhD
Carbon P. Dubbs Professor of Chemical Engineering and Biological Engineering, MIT
Thesis Advisor

Darrell J. Irvine, PhD
Professor of Materials Science & Engineering and Biological Engineering, MIT
Thesis Committee Chair

Stefani Spranger, PhD
Howard S. and Linda B. Stern Career Development Professor
Assistant Professor of Biology, MIT

Philip J. Kranzusch, PhD
Associate Professor of Microbiology, Harvard Medical School
Associate Professor of Cancer Immunology and Virology, Dana-Farber Cancer Institute

Engineering Intratumoral Cytokine Therapies for Cancer

by
Emi A. Lutz

Submitted to the Department of Biological Engineering
on June 21, 2022 in partial fulfillment of the requirements for the degree of
Doctor of Philosophy in Biological Engineering

Abstract

Immunotherapies enable effective, long-lasting anti-tumor immunity for some cancer patients. Cytokines are key signaling proteins that help activate and sustain critical immune cells during this process. Unfortunately, traditional cytokine therapies suffer from low efficacy and high systemic toxicity. As one strategy to improve therapeutic index, intratumorally administered and retained cytokines have been demonstrated to improve both safety and efficacy. However, further research on intratumoral cytokine therapies is needed to uncover optimal design strategies and considerations when eliciting strong, localized cytokine exposure. Towards this goal, we first test if intratumoral administration and retention is an effective strategy for type I interferons (IFN). Significant enhancement in tumor retention of IFNα and IFNβ, mediated by anchoring these IFNs to co-injected aluminum-hydroxide (alum) particles, greatly improved their tolerability and efficacy. The improved efficacy of alum-anchored IFNs could be attributed to sustained pleiotropic effects on tumor cells, immune cells, and non-hematopoietic cells. Alum-anchored IFN therapies were curative upon combination with either anti-PD-1 or interleukin-2 (IL-2). However, only the anti-PD-1 combination led to protection against tumor rechallenge, demonstrating that overstimulation of cytokine signaling can dampen memory response. Second, we research design criteria for intratumorally administered IL-2 fused to tumor-specific nanobodies. Using yeast surface display, we develop IL-2 fusions with a range of affinities to the tumor-specific EIIIB domain of fibronectin. Such IL-2 fusions enabled strong anti-tumor efficacy, provided both intratumoral administration and sufficient affinity to EIIIB. Third, we explore intratumoral therapies that activate the cGAS-STING pathway, which leads to type I IFN production. Specifically, we design DNA-based agonists of cGAS that delay tumor growth in mice. Together, this thesis furthers our understanding of how to effectively elicit localized cytokine responses at the tumor for cancer immunotherapy.

Thesis Advisor: K. Dane Wittrup, Ph.D.
Carbon P. Dubbs Professor of Chemical Engineering and Biological Engineering, MIT

Contents

Acknowledgments

First and foremost, I would like to thank my advisor, Prof. Dane Wittrup, for all of his mentorship and time. Dane gave me constant support and kind guidance, and I am grateful for everything he taught me during graduate school. I would like to thank my thesis committee, Prof. Darrell Irvine, Prof. Stefani Spranger, and Prof. Philip Kranzusch, for their advice and encouragement. Thank you also to Prof. Richard Hynes and Dr. Justin K. Murray for mentoring me during my time as a graduate student.

I am extremely thankful to key collaborators that helped enable the projects in this thesis. Noor Momin and Noor Jailkhani were fantastic collaborators and mentors and it was a pleasure to have worked besides them towards our joint research presented in Chapter 3. Yash Agarwal was another wonderful collaborator and instrumental in Chapter 2.

I am very thankful to the entire Wittrup lab for all of their support, advice, and friendship. Ryan, Monique, Naveen, Adrienne, Alison, Noor and Byong welcomed me into the lab and taught me critical skills. I am glad to have had the opportunity work with students that have joined the lab since: Yash, Joseph, Sarah, Alli, Keith, Bri, Anthony, Luciano, Jordan, Megan, Owen, Lauren, David, Liz, Bill, Vlada, and Janice. You have all made the lab a fun place to work, and I appreciate each of you for the times we shared and the help you provided. I am especially grateful to a lot of mentorship early on in graduate school from Noor, Naveen, and Adrienne. Thank you to undergraduate researcher Vlada, who researched with me for three years, made valuable project contributions, and was a fun collaborator. Thank you to Noor and Yash for the countless hours spent discussing and encouraging this research.

Thank you to the supportive community at the Koch Institute for helping with the research presented here, including Ellen Duong from the Spranger lab, Ying Huang from the Hynes lab, and Mariann Murray. This research was also enabled by the expertise and equipment from the Koch Institute's Swanson Biotechnology Center, the MIT Biology Biophysical Instrumentation Facility, and the Division of Comparative Medicine. Thank you to all of the funding sources for this research, which are specifically acknowledged at the end of each chapter.

Thank you to the faculty and staff in the MIT Department of Biological Engineering for their support throughout the graduate school journey. The BE class of 2016 also provided a warm community. Last, I am extremely thankful to my friends and family for the adventures, love, and support.

List of Figures and Tables

Chapter 1. Introduction

The immune system is a powerful tool to fight cancer and can promote long-lasting cures for oncology patients if effectively harnessed. There are many intricate steps in establishing a productive anti-tumor immune response (*1*). The cancer-immunity cycle first relies on the release of cancer cell antigens alongside immunogenic signals. These antigens are presented by antigen-presenting cells in order to prime and activate T cells. T cells then traffic to and infiltrate tumors to promote cancer cell killing. Cancer immunotherapies aim to initiate or strengthen one or more of these steps (*1*). For example, therapies that address early steps in the anti-tumor immune response include cancer vaccines to help elicit responses to personal tumor neoantigens (*2*, *3*). If anti-tumor T cells already exist, checkpoint blockade antibodies can counter inhibitory signals that dampen or exhaust T cell activity (*2*, *4*). T cells with high tumor-reactivity can also be prepared *ex vivo* and administered to patients during adoptive T cell transfer (*2*, *5*).

Another promising class of cancer immunotherapies are cytokines, which can be used alone or in combination with any of the above approaches (*6*). Cytokines are small signaling proteins that are critical in activating and sustaining immune cells throughout the cancer-immunity cycle, especially during antigen presentation, T cell priming and activation, and cancer-cell killing (*1*). In the 1980s and 1990s, therapeutic cytokines, specifically interferon alpha (IFNα) (*7*), and interleukin-2 (IL-2) (*8*, *9*), began gaining approval from the US Food and Drug Administration for the treatment of various cancers. Unfortunately, safe and effective therapeutic use of cytokines has proven to be challenging (*6*, *10*). One initial problem for cytokine therapies was their inherent poor half-life. Many strategies have since been developed to extend cytokine half-life, including PEGylation (*11*, *12*) and albumin fusions (*13*, *14*). Even with the ability to extend half-life, challenges with cytokine therapies persisted. A central issue is that cytokine receptors are widely expressed, and receptor engagement leads to a wide range of downstream events (*10*). Engaging cytokine signaling with specific immune cells (such as dendritic cells or CD8+ T cells) in specific locations (such as at the tumor or tumor draining lymph node) can be extremely powerful. However, cytokine signaling on unintended cell types or at undesired locations leads to dangerous toxicities. The biggest challenge of cytokine therapies is thus constraining the effects of these potent molecules to elicit only the desired phenotypes in the right places. This is an active area of study, and there has been substantial effort to improve cytokine therapies by tumor-targeting (*15–19*), immune-targeting (*20*, *21*), and conditional activation at the tumor site (*22–25*), among other strategies (*10*, *26*, *27*). Although progress has been made in each area, effective control of cytokine signaling is still challenging in the clinic.

One approach to spatially constrain cytokine signaling to the tumor site is intratumoral administration. Cytokines are traditionally administered systemically, but intratumoral injection inherently enables a higher relative concentration of drug at the tumor. Intratumoral injections have become feasible in the clinic for many cancer types and anatomical locations (*28–30*). However, after intratumoral administration, unmodified cytokines can leak out of the tumor within a day (*31*). Thus, various retention strategies have been developed to prevent rapid

leakage out of the tumor to maximize tumor exposure for improved efficacy. Strategies that afford extended retention to locally-injected cytokines include tethering to the extracellular matrix (*31–34*), cellular targets (*35–37*), or various biomaterials (*38–41*). Using these strategies to intratumorally administer and retain cytokines like IL-2, IL-12, and TNF has demonstrated safer, more effective control of primary tumors, metastases, and distant untreated lesions (*32–41*).

However, intratumoral cytokine therapies warrant further study. Only a limited number of cytokines have been tested in this context, and more research is required to test the potential benefit for a wider range of cytokines. In addition, there is a need for a better understanding of optimal design formats for eliciting strong, localized cytokine exposure. This thesis addresses these research areas with three separate projects.

In chapter 2, we test if intratumoral administration and retention is an effective strategy for type I interferons (IFN). Endogenous type I IFNs are critical to anti-tumor immunity (*42–44*), but it was unclear whether sustained IFN signaling at the tumor would promote or inhibit anti-tumor responses. It was also unclear which IFN subtype would be optimal for intratumoral therapies. To study these questions, we generated type I IFNs that stay in the tumor long-term by binding to co-injected aluminum hydroxide (alum) particles, a strategy recently developed in the Wittrup and Irvine labs (*38*). We find that intratumoral retention of type I IFNs generally improved anti-tumor efficacy and toxicity in multiple immunocompetent tumor models in mice. However, combination with extended half-life IL-2 demonstrated that over-activation of T cells can harm memory response against rechallenge tumors.

In chapter 3, we address how to design intratumoral nanobody-cytokine fusions. We developed interleukin-2 fusions to nanobodies that bind the tumor-specific EIIIB domain of fibronectin. We used yeast surface display to generate cytokine fusions with a range of affinities to EIIIB. We find that intratumoral administration of such cytokines leads to strong anti-tumor efficacy, provided sufficient affinity to EIIIB. We also compared nanobody-cytokine fusions with intratumoral or intravenous administration, and find that intratumoral administration provides a large degree of benefit. Chapter 3 was a collaborative effort between the Wittrup lab (Emi Lutz and Noor Momin) and the Hynes lab (Noor Jailkhani).

Last, in chapter 4, we explore alternative methods to elicit strong cytokine signatures in the tumor. We focus on intratumoral therapies to activate the cGAS-STING pathway, which leads to type I interferon production. Specifically, we design DNA-based agonists of cGAS, and show that they can delay tumor growth in mice.

Together, this thesis furthers our understanding of how to effectively elicit localized cytokine responses at the tumor for cancer immunotherapy. Carefully designed intratumoral cytokine therapies hold great promise for controlling effective anti-tumor immunity.

Chapter 2. Alum-anchored intratumoral retention improves the tolerability and anti-tumor efficacy of type I interferon therapies

This chapter, with some modifications, was submitted for publication.

Abstract

Effective anti-tumor immunity in mice requires activation of the type I interferon (IFN) response pathway. Type I IFN therapies have proven promising in humans, but suffer from limited efficacy and high toxicity. Intratumoral IFN retention ameliorates systemic toxicity, but given the complexity of IFN signaling, it was unclear whether long-term intratumoral retention of type I IFNs would promote or inhibit anti-tumor responses. To this end, we compared the efficacy of IFNα and IFNβ that exhibit either brief or sustained retention after intratumoral injection in syngeneic mouse tumor models. Significant enhancement in tumor retention, mediated by anchoring these IFNs to co-injected aluminum-hydroxide (alum) particles, greatly improved both their tolerability and efficacy. The improved efficacy of alum-anchored IFNs could be attributed to sustained pleiotropic effects on tumor cells, immune cells, and non-hematopoietic cells. Alum-anchored IFNs achieved high cure rates of B16F10 tumors upon combination with either anti-PD-1 antibody or extended half-life interleukin-2. Interestingly however, these alternative combination immunotherapies yielded disparate T cell phenotypes and differential resistance to tumor rechallenge, highlighting important distinctions in adaptive memory formation for combinations of type I IFNs with other immunotherapies.

Introduction

Type I interferons (IFN), comprised of IFNα subtypes and IFNβ, are potent cytokines with significant impacts on anti-tumor immunity, angiogenesis, and tumor growth (*45*, *46*). Endogenous type I IFNs are critical to anti-tumor immunity (*42–44*), and effective modulation of the type I IFN pathway holds great promise for improving cancer immunotherapies. Starting in the 1980s, IFNα gained approval from the US Food and Drug Administration (FDA) for the treatment of various cancers (*7*). IFNα is rapidly cleared, so extended half-life PEGylated IFNα was also FDA-approved (*11*, *12*). However, both IFNα and PEGylated IFNα suffer from low efficacy and high toxicity, in part because almost all cells in the body express the IFN-α/β receptor (IFNAR) (*10*). The challenges of type I IFN therapies have been recognized for decades, and there has been substantial effort to improve IFNs by tumor-targeting (*15–17*), immune-targeting (*20*, *21*), and conditional activation at the tumor site (*22–24*), among other strategies (*10*).

We hypothesized that intratumorally injecting type I IFNs and retaining them in the tumor long-term could improve on-target activity while reducing systemic toxicity. Intratumoral administration is feasible in the clinic (*28–30*), and local retention of other cytokines has safely promoted strong anti-tumor responses (*32*, *33*, *38*). In support of this hypothesis, inducing tumors to overexpress type I IFNs using gene transduction has enabled tumor regression in

mice (*47–50*). On the other hand, some studies suggest that sustained IFN signaling in the tumor can be detrimental, particularly in the context of anti-PD-1 (αPD1) therapy (*51–53*). However, recombinant type I IFN therapies with long-term intratumoral retention have yet to be studied extensively in immunocompetent mice.

When intratumorally injecting cytokines, a retention strategy can prevent rapid leakage out of the tumor and thus maximize tumor exposure for improved efficacy (*31*). Recently, the Wittrup and Irvine labs anchored cytokines within tumors for weeks by introducing strong affinity to co-injected aluminum hydroxide (alum) particles (*38*). Alum is a safe, commonly-used material that is FDA-approved as a vaccine adjuvant. Agarwal et al demonstrated in mice that alum-anchored interleukin-12 (IL-12) stayed at the tumor for weeks, reduced treatment-related toxicity, and promoted cures at primary tumors, metastases, and distant untreated lesions. Alum-anchoring enhanced the therapeutic efficacy of interleukin-2 (IL-2) as well (*38*).

In this chapter, we compared IFNα, extended half-life IFNα, and alum-anchored IFNα in syngeneic mouse tumor models. The impact of type I IFN subtype on treatment efficacy remains poorly defined (*54–56*), so we also developed IFNβ counterparts. Intratumoral retention improved the efficacy of type I IFNs as monotherapy. Optimal type I IFN subtype was context-dependent. In combination with extended half-life IL-2, alum-anchored IFNs reduced toxicity and achieved high cure rates at the primary tumor, but suffered poor resistance to rechallenge tumors. When combined with αPD1, IFN therapies were generally highly effective both at eliminating the primary tumor and protecting from subsequent tumor rechallenge. We investigated the mechanisms behind these therapeutic outcomes and discuss how these results can inform effective design strategies for type I IFN therapies.

Results

Development of a panel of type I IFNs

We developed five murine type I IFNs with different signaling strengths and pharmacokinetics (**Fig. 2-1, Table 2-1**) We recombinantly expressed murine IFNα subtype A (referred to here as IFNα), and murine IFNβ, which is an order of magnitude more potent than IFNα (*57*). Since PEGylated IFNα is used in the clinic (*11*, *12*), we also generated an extended-half-life format of IFNα by fusion to mouse serum albumin (MSA). Albumin extends cytokine half-life by FcRn-mediated recycling and reducing renal clearance, and albumin-IFNα fusions have been previously validated (*10*, *13*, *14*).

Next, we employed a system that Agarwal et al recently developed to enable long-term retention of intratumorally-injected cytokines (*38*). This strategy relies on aluminum hydroxide (alum) particles that are retained at their injection site as a physical depot for weeks. By fusion to an alum-binding peptide (ABP), ABP-cytokines that are mixed and co-injected with alum are also retained long-term. The design of ABP contains serine motifs that are phosphorylated upon co-expression with the Fam20C kinase (*38*) because phosphates bind tightly to alum through a ligand exchange reaction with surface hydroxyls (*58*, *59*). Indeed, ABP-IFNs co-expressed with

Fam20C had higher phosphorylation (**Fig. 2-2A**) compared to IFNs without ABP. ABP-IFNα had on average ~1 phosphate per protein, while ABP-IFNβ had on average ~2.5 phosphates per protein. These phosphorylation levels are lower than the theoretical maximum of 4 phosphorylation sites on ABP. Increasing the linker length between ABP and IFN from GGGS to $(G_4S)_3$ did not improve phosphorylation levels, so we continued to work with the original GGGS linker format (**Fig. 2-2B**). We optimized the percentage of kinase used in the transfection procedure to ~5% to balance between IFN yield and phosphorylation levels (**Fig. 2-2C**). Despite having fewer than 4 phosphates per protein, ABP-IFNs still demonstrated tighter alum-binding *in vitro* compared to IFNs without ABP (**Fig. 2-2D**). Last, to test translatability, we confirmed that human IFNα2b could also be expressed (**Fig. 2-1B**) and phosphorylated (**Fig. 2-2A**) as an ABP-fusion.

All five murine IFNs activated RAW-Lucia ISG cells *in vitro*, an IFN-responsive macrophage line, albeit with a mild increase in EC_{50} for fusion proteins (**Fig. 2-3A**). IFNβ constructs were an order of magnitude more potent than IFNα constructs, and ABP-IFNs maintained their activity in the presence of alum (**Fig. 2-3A**). The five murine IFNs also demonstrated anti-proliferative activity on MC38 colon adenocarcinoma cells *in vitro* (**Fig. 2-3B**).

To evaluate pharmacokinetics, we injected AF647-labeled IFNs intratumorally (i.t.) into apigmented B16F10 tumors and tracked their retention at the tumor for five days (**Fig. 2-4 A and B**). Upon co-injection with alum, ABP-IFNα and ABP-IFNβ were retained in the tumor for all five days. In contrast, IFNα, IFNβ, and MSA-IFNα leaked out of the tumor within one day. Five days after treatment, AF647-IFN levels in homogenized organs were measured by fluorescence spectroscopy. ABP-IFNs were highly specific for the tumor, with no signal detected in the serum, spleen, liver, lung, or kidney (**Fig. 2-4C**). Serum fluorescence levels confirmed that MSA-IFNα had extended circulation, while the other IFNs were not detected in the serum at the time-points tested (**Fig. 2-4D**).

Intratumoral retention improves type I IFN monotherapy

The five IFNs were tested for therapeutic efficacy as a single agent. Mice bearing established MC38 colon carcinoma tumors (**Fig. 2-5**) or B16F10 melanoma tumors (**Fig. 2-6**) were treated with 0.5 nmol IFN i.t. on days 5, 11, and 17. Tumor growth (**Fig. 2-5A, Fig. 2-6A**) and survival (**Fig. 2-5B, Fig. 2-6B**) demonstrated that IFNα had poor efficacy in both tumor models and only extended median survival by four to five days compared to the Tris-buffered saline (TBS) control. IFNβ was not significantly different than IFNα ($P = 0.18$ for MC38, $P = 0.81$ for B16F10), indicating that increasing signaling strength alone was insufficient to improve efficacy.

Intratumoral retention improved survival from type I IFN therapies. Alum + ABP-IFNα significantly extended survival over IFNα ($P = 0.0005$ for MC38, $P = 0.01$ for B16F10). Similarly, Alum + ABP-IFNβ was more efficacious than IFNβ ($P = 0.0005$ for MC38, $P < 0.0001$ for B16F10). As a control, even large doses of alum alone did not slow B16F10 growth, indicating that the efficacy was IFN-mediated (**Fig. 2-6D**) (*38*). In immunologically cold B16F10 tumors,

the more potent Alum + ABP-IFNβ was more efficacious than Alum + ABP-IFNα (P = 0.004). In contrast, in the MC38 model, the less potent Alum + ABP-IFNα was more efficacious than Alum + ABP-IFNβ (P = 0.002), showing that optimal type I IFN signaling can be tumor-dependent. MSA-IFNα had similar efficacy to Alum + ABP-IFNα in both models (P = 0.48 for MC38, P = 0.43 for B16F10). However, mice treated with MSA-IFNα experienced mild body weight loss that was not observed from the alum-anchored IFNs, raising toxicity concerns for prolonging half-life without intratumoral retention (**Fig. 2-6C**).

Next, we asked how intratumoral retention improved type I IFN therapies, focusing on the poorly inflamed B16F10 model, which showed the strongest tumor growth delay with alum-anchored IFNβ (**Fig. 2-6A**). Type I IFNs are pleiotropic and can have a wide range of impacts on tumor cells, endothelial cells, and immune cells (*45*, *46*). We examined each of these compartments to uncover the therapeutic mechanism behind Alum + ABP-IFNβ in B16F10 tumors.

Alum + ABP-IFNβ therapy alters tumor cells

To study impacts on tumor cells, B16F10 tumors were treated with TBS, IFNβ, or Alum + ABP-IFNβ, followed four days later by flow cytometry of live tumor cells (**Fig. 2-7**). In addition to wild-type (WT) mice, we included Ifnar1$^{-/-}$ mice whose host cells are deficient in type I IFN sensing so only the implanted B16F10 cells can directly respond to IFN treatment.

Type I IFNs can alter how tumor cells interact with immune cells via transcriptional regulation of thousands of genes (*46*). Importantly, type I IFNs upregulate MHC-I on tumor cells, improving immune recognition (*60*). Alum + ABP-IFNβ led to a greater proportion of B16F10 cells with high MHC-I expression in both WT mice (P = 0.04 compared to TBS) and Ifnar1$^{-/-}$ mice (P = 0.009 compared to TBS) (**Fig. 2-8A**). The altered MHC-I phenotype was substantial even in Ifnar1$^{-/-}$ mice, suggesting that alum-anchored payloads were unexpectedly uniformly accessible throughout the tumor. TBS-treated WT mice had greater %MHC-I^{high} levels than TBS-treated Ifnar1$^{-/-}$ mice (P = 0.02), highlighting that endogenous type I IFN signaling also impacts B16F10 cells considerably in this therapy. Type I IFNs can also upregulate PD-L1 on tumor cells, which suppresses T-cell function by binding to the PD-1 receptor expressed on activated T cells (*17*). In WT mice, Alum + ABP-IFNβ increased median PD-L1 levels, and increased the percentage of B16F10 cells with high PD-L1 expression (**Fig. 2-8B**). Although not significant, PD-L1 levels also trended upwards in treated Ifnar1$^{-/-}$ mice.

Type I IFNs can be anti-proliferative and pro-apoptotic to tumor cells (*46*). No anti-proliferative activity was observed in tumor cells as measured by Ki67 (**Fig. 2-8C**). However, Alum + ABP-IFNβ caused live tumor cells in WT mice to be more apoptotic, as measured by Apotracker Green, which detects phosphatidylserine residues on the cell surface (P = 0.0001 compared to TBS, **Fig. 2-8D**). No changes in Apotracker Green levels occurred in Ifnar1$^{-/-}$ mice (P = 0.77), indicating that the pro-apoptotic effect observed in WT mice was mediated indirectly.

This study showed that Alum + ABP-IFNβ altered tumor cells, both directly (MHC-I and PD-L1 levels) and indirectly (apoptosis). The direct effects on tumor cells were impactful, and led to an increase in total $CD45^+$ immune cells in the tumor in $Ifnar1^{-/-}$ mice (**Fig. 2-8E**). However, the direct effects on tumor cells alone were insufficient to slow tumor growth. Both the strong efficacy of Alum + ABP-IFNβ and the mild efficacy of IFNβ in WT mice (**Fig. 2-6 A and B**) was completely lost when the treatment regimen was repeated in $Ifnar1^{-/-}$ mice (**Fig. 2-9**), indicating that interactions with IFN-responsive host cells are essential for efficacy.

Alum + ABP-IFNβ relies on non-hematopoietic cells

Endothelial cells are an important consideration because type I IFNs are anti-angiogenic (*45*, *47*). In order to examine the role of non-hematopoietic cells in treatment efficacy, bone marrow chimeras were generated. WT and $Ifnar1^{-/-}$ hosts were lethally irradiated, then reconstituted with bone marrow (BM) from congenically marked WT donors. Thus, in the $Ifnar1^{-/-}$ hosts, the non-immune compartment is deficient in type I IFN sensing. After six weeks, BM engraftment was confirmed (**Fig. 2-10A**). Mice were inoculated with B16F10 tumors, followed by TBS or Alum + ABP-IFNβ treatments. As expected, survival (**Fig. 2-10B**) and tumor growth (**Fig. 2-10C**) showed strong therapeutic efficacy in WT hosts ($P = 0.001$). The treatment still promoted tumor growth delay and extended survival in $Ifnar1^{-/-}$ hosts ($P = 0.001$). However, comparing the two Alum + ABP-IFNβ groups revealed significant reduction in efficacy by removing the non-hematopoietic compartment's ability to respond to type I IFNs ($P = 0.0004$).

Alum + ABP-IFNβ activates dendritic cells and CD8+ T cells

To begin assessing the immune compartment, B16F10 tumors were treated with TBS, IFNβ, or Alum + ABP-IFNβ, and tumor lysates were analyzed four days later for chemokines and cytokines. All concentrations are reported (**Fig. 2-11**), and a heatmap visualizes fold change compared to TBS (**Fig. 2-12**). Compared to TBS, Alum + ABP-IFNβ significantly increased CXCL10 (14-fold, $P < 0.0001$), IFNγ (7.4-fold, $P = 0.0009$), RANTES (5.8-fold, $P < 0.0001$), MCP-1 (3.2-fold, $P = 0.0002$), IL-12 (2.6-fold, $P = 0.0003$), IL-10 (1.7-fold, $P = 0.0009$), TNFα (1.7-fold, $P = 0.047$), IL-1β (1.5-fold, $P = 0.01$), and GM-CSF (1.4-fold, $P = 0.003$). Compared to unanchored IFNβ, Alum + ABP-IFNβ had significantly higher CXCL10 ($P < 0.0001$), RANTES ($P = 0.001$), and MCP-1 ($P = 0.001$), highlighting that intratumoral retention induced a stronger chemokine signature.

To understand which immune cells play a role, the Alum + ABP-IFNβ treatment regimen was repeated using mice lacking specific immune compartments via genetic knockout or confirmed antibody-mediated depletions (**Fig. 2-13**). Depleting NK cells and neutrophils did not harm efficacy (**Fig. 2-14A**). The Nlrp3 inflammasome, which can be activated by alum, was also dispensable (**Fig. 2-14B**) (*61*). However, treatment efficacy was significantly reduced in mice lacking Batf3 dendritic cells (DCs) (**Fig. 2-14C**) or CD8+ T cells (**Fig. 2-14A**). The type I IFN pathway plays a pivotal role in DC antigen presentation and CD8+ T cell priming and expansion (*42–44*). Indeed, four days after treatment with Alum + ABP-IFNβ, there was a greater proportion and total count of $Ly6C^-$ $MHCII^+$ $CD24^+$ DCs in the tumor draining lymph node (tdLN)

that expressed activation marker CD86 (**Fig. 2-15A**). In addition, six days after treatment with Alum + ABP-IFNβ, there were more CD8+ T cells per mg tumor and a greater proportion of CD8+ T cells in the tumor were activated compared to TBS, as measured by Ki67 (P = 0.003), TIM3 (P = 0.002), and TCF1 (P = 0.01) (**Fig. 2-15B**).

These experiments revealed a pleiotropic mechanism of action in B16F10 tumors. Alum + ABP-IFNβ induced important changes in tumor cells, and therapeutic efficacy relied on non-hematopoietic cells, DCs, and CD8+ T cells. After investigating how Alum + ABP-IFNβ interacted with the tumor microenvironment as a single agent, we moved on to study if combining IFNs with other immunotherapies could enable tumor cures.

IFNs in combination with MSA-IL2 of αPD1

First, we combined the panel of IFNs with an extended half-life form of IL-2 (MSA-IL2) (*62*). IFNα and IL-2 are currently the only two FDA-approved cytokines for cancer. Although IFNα and IL-2 play complementary roles in the cancer immunity cycle (*1*, *63*, *64*), their combination has been generally unsuccessful in the clinic to date (*65*–*67*). B16F10 tumors were treated on days 5, 11, and 17 with IFNs (i.t.), previously shown not to be curative as a single agent (**Fig. 2-6**). 30 μg MSA-IL2 (i.p.) was dosed concurrently. Survival (**Fig. 2-16A**) and tumor growth (**Fig. 2-16B**) showed that MSA-IL2 alone only delayed median survival by two days. Almost complete cure rates were achieved when MSA-IL2 was combined with Alum + ABP-IFNα (6/6 cures) or Alum + ABP-IFNβ (6/7 cures). In stark contrast, no mice were cured when MSA-IL2 was combined with IFNα, MSA-IFNα, or IFNβ. The Wittrup lab and others have observed that cytokine combinations can exacerbate treatment-related toxicities (*32*, *68*, *69*). Extended half-life MSA-IFNα combined with MSA-IL2 led to substantial weight-loss, and 4 out of 7 mice were euthanized due to toxicity (**Fig. 2-16C**). In contrast, alum-localized IFNs combined with MSA-IL2 avoided this overt toxicity.

The Wittrup lab has previously shown that the relative timing of IFNα, extended half-life IL-2, and tumor-targeting antibodies is critical to treatment efficacy and toxicity (*63*, *68*). In this new treatment setting where a tumor-targeting antibody is no longer present, a pilot experiment indicated that staggering IFNα after MSA-IL-2 did not have a large impact on efficacy (**Fig. 2-17**). We did not continue to explore the relative timing between IFNs and MSA-IL2 in this thesis.

Second, we combined IFNs with αPD1, in part motivated by the PD-L1 upregulation on tumor cells following localized IFN treatment (**Fig. 2-8B**). There are also many reports of improved anti-tumor efficacy in mice from combining type I IFN pathway agonists with αPD1 or aPD-L1 (*16*, *17*, *70*, *71*). Mice bearing B16F10 tumors were treated on days 5, 11, and 17 with IFNs (i.t.) and 200 μg αPD1 (i.p.). Survival (**Fig. 2-18A**) and tumor growth (**Fig. 2-18B**) demonstrated that αPD1 alone could not cure B16F10 tumors. Mice were cured when αPD1 was combined with IFNα (5/6 cures), Alum + ABP-IFNα (6/6 cures), IFNβ (4/6 cures), or Alum + ABP-IFNβ (4/5 cures). Mice did not lose body weight (**Fig. 2-18C**).

Combination immunotherapies yield contrasting memory responses.

After 100 - 110 days, cured mice were rechallenged with 0.1 M B16F10 cells in the opposite flank, and monitored for an additional 100 days. We observed poor resistance to rechallenge in mice cured from MSA-IL2 combined with Alum + ABP-IFNα (1/6 survivors) or Alum + ABP-IFNβ (1/6 survivors) (**Fig. 2-19A**). Mice cured from αPD1 + Alum + ABP-IFNβ also had poor resistance to rechallenge (1/4 survivors) (**Fig. 2-19B**). In contrast, we observed strong resistance to rechallenge in mice cured from αPD1 combined with IFNα (4/5 survivors), IFNβ (4/4 survivors), or Alum + ABP-IFNα (5/6 survivors) (**Fig. 2-19B**). We were specifically intrigued by the difference between Alum + ABP-IFNα in combination with MSA-IL2 compared to αPD1. Both therapies achieved 100% cures at the primary tumor (**Fig. 2-16A and 2-18A**) but led to starkly different resistance to rechallenge (**Fig. 2-19**).

To investigate this mechanism, B16F10 tumors were treated on day 5 and 11 with Alum + ABP-IFNα, either alone, with MSA-IL2, or with αPD1. On day 13, spleens were excised, and T cells were analyzed by flow cytometry (**Fig. 2-20**). Markers KLRG1 and CD127 (a subunit of IL-7R) predict if CD8+ T cells are short-lived effector cells (SLECs) or memory precursor effector cells (MPECs) (*72*–*75*). Alum + ABP-IFNα alone did not appreciably raise the percentage of $CD3^+$ $CD8^+$ $CD44^+$ effector T cells that were SLECs (%SLECs), which may explain why Alum + ABP-IFNα failed to achieve cures as a single agent (**Fig. 2-20B and Fig. 2-21**). In contrast, the MSA-IL2 combination substantially increased %SLECs ($P < 0.0001$ compared to untreated), helping explain the 6/6 cure rate at the primary tumor. However, the increase in %SLECs came at the cost of a drastic decrease in %MPECs ($P < 0.0001$ compared to untreated), consistent with the poor rechallenge results from the MSA-IL2 combination. On the other hand, the αPD1 combination increased %SLECs compared to untreated ($P = 0.03$), but to a lesser extent than the MSA-IL2 combination ($P = 0.02$). Conversely, the αPD1 combination had mild reduction in %MPECs compared to untreated ($P = 0.03$), but still maintained high %MPEC compared to the MSA-IL2 combination ($P < 0.0001$). The αPD1 combination appears to have achieved T cell phenotypes that enabled both 6/6 cures at the primary tumor and 5/6 survivors in the rechallenge setting.

The MSA-IL2 combination had several additional key differences compared to the αPD1 combination (**Fig. 2-20C and Fig. 2-22**). The MSA-IL2 combination-treated mice had enlarged spleens ($P < 0.0001$) (**Fig. 2-22A**), although there was no significant increase in total CD8+ T cells in the spleen (**Fig. 2-22B**) (*76*). The MSA-IL2 combination also increased the proportion of CD8+ T cells that expressed CD25 ($P < 0.0001$), proliferation marker Ki67 ($P = 0.01$) and exhaustion marker TIM3 ($P = 0.0001$) (**Fig. 2-22C**). Of note, excessive CD25 expression and prolonged IL-2 signaling has been reported to make T cells prone to terminal differentiation (*77*). All treatments increased TCF1 levels compared to untreated (**Fig. 2-22D**). Overall, the MSA-IL2 combination with poor rechallenge data had spleens with a dramatic increase in SLECs, reduction in MPECs, and over-activation of T cells.

Abscopal response from intratumoral IFN therapies

Another important consideration for intratumoral therapies is if treatment at one tumor can lead to anti-tumor efficacy at untreated lesions. To test this, we inoculated subcutaneous tumors on the right and left flanks, but only performed intratumoral treatments at the right tumor (**Fig. 2-23 and Fig. 2-24**). Treatment with Alum + ABP-IFNβ (i.t.) alone (**Fig. 2-23A**) or Alum + ABP-IFNβ (i.t.) combined with MSA-IL2 (i.p.) (**Fig. 2-23B**) did not substantially delay tumor growth at the untreated tumor for the aggressive B16F10 model. We also tested mice bearing B16OVA tumors, which express the model tumor antigen ovalbumin (**Fig. 2-24**). In this model, mice treated with Alum + ABP-IFNα (i.t.) and αPD1 (i.p.) had significantly smaller untreated tumors compared to mice treated with αPD1 (i.p.) only (**Fig. 2-24C**), showing that localized IFN treatments can promote systemic anti-tumor immunity. However, no mice were cured (**Fig. 2-24A**), motivating future research to continue improving our ability to elicit strong responses against multiple tumor sites and metastases.

Discussion

Cytokines can initiate potent anti-tumor immune responses, but their use is hindered by poor therapeutic indices (*10*). Systemic delivery of cytokines is challenging because cytokine receptors are widely expressed throughout the body, leading to high receptor engagement in the periphery, even if tumor-targeting is attempted (*18*). Consequently, a growing body of cytokine therapeutic development has begun shifting from systemic to intratumoral administration. Local delivery enables high cytokine concentration at the tumor initially, but unanchored proteins can rapidly leak out (*31*). Strategies that afford some retention to locally-injected cytokines include tethering to the extracellular matrix (*31*–*34*), cellular targets (*35*–*37*), or various biomaterials (*39*–*41*). Of note, the Wittrup and Irvine labs recently enabled particularly long-term intratumoral retention for weeks by using the FDA-approved material alum, which forms intratumoral depots and serves as an anchor for alum-binding cytokines (*38*). Together, these strategies have demonstrated that intratumorally injecting and retaining cytokines like IL-2, IL-12, and TNF can dramatically improve toxicity and initiate potent systemic anti-tumor immunity. However, it was unclear whether recombinant type I IFNs would similarly benefit from intratumoral retention in immunocompetent mice. In this chapter, we engineered intratumorally retained IFNs and characterized their therapeutic potential and mechanism.

We developed five IFNs with different signaling strengths and pharmacokinetics: IFNα, IFNβ, extended half-life MSA-IFNα, alum-anchored ABP-IFNα, and alum-anchored ABP-IFNβ. Compared to IFNα or IFNβ alone, alum-anchored IFNs improved anti-tumor efficacy as an MC38 monotherapy, B16F10 monotherapy, and B16F10 combination therapy with MSA-IL2. When combined with αPD1, all IFNs tested exhibited a high B16F10 cure rate. Extended half-life IFNα is also clinically relevant (*11*, *12*). Compared to extended half-life MSA-IFNα, alum-anchoring improved tolerability as measured by weight loss, and demonstrated superior efficacy when combined with MSA-IL2. These results show that alum-anchoring enabled high efficacy from type I IFNs while maintaining safe tolerability in mice.

We examined the mechanism behind Alum + ABP-IFNβ monotherapy in B16F10 tumors in detail. With regards to tumor cells, others have observed that hydrogel-retained human IFNα moderately slowed the growth of xenograft tumors in nude mice (*78–81*), and tumors exhibited decreased proliferation and increased apoptosis *in vivo* (*78*, *79*). In our immunocompetent tumor model, alum-anchored IFNβ did not directly slow the growth of B16F10 tumors, but did indirectly increase apoptosis on tumor cells. Alum-anchored IFNβ also led to tumors upregulating MHC-I, which improves immune recognition, and upregulatingPD-L1, which increases the likelihood of T cell exhaustion. Combining IFNs with αPD1 successfully alleviated this stress on T cells and enabled high cure rate. We did not test other potential impacts of IFNs on tumor cells, such as altering the cell cycle or the epithelial-to-mesenchymal transition (*46*).

Alum-anchored IFNβ heavily relied on non-hematopoietic cells for efficacy. A previous study also observed the importance of non-hematopoietic cells for local IFNβ. Gajewski and colleagues generated B16 tumor cells that over-expressed IFNβ, which caused tumors to regress (*47*). Regression depended on IFNAR expression in vascular endothelial cells. Consistent with type I IFN's anti-angiogenic properties (*45*), IFNβ-expressing B16 tumors had lower blood vessel density (*47*). Type I IFNs can also cause endothelial cells to produce chemokines like CXCL10 that play roles in inhibiting angiogenesis, as well as in recruiting and activating immune cells (*82*, *83*). We indeed observed much higher CXCL10 levels from alum-anchored IFNβ compared to unanchored IFNβ, although we did not directly measure blood vessel density.

Another component of alum-anchored IFNβ's mechanism was immune-mediated. Alum + ABP-IFNβ elicited a strong inflammatory signature with increased levels of many cytokines and chemokines. Batf3 DCs and CD8+ T cells were critical to therapy, both of which had improved activation upon treatment, consistent with the role of type I IFNs in DC antigen presentation and CD8+ T cell priming and expansion (*42–44*). Although we investigated the major immune cells implicated in IFN therapies including DCs, CD8+ T cells, NK cells and neutrophils, studying additional cell types like Tregs and macrophages may reveal additional mechanisms (*45*, *46*).

Overall, alum-anchored IFNβ orchestrated a pleiotropic mechanism of action with impacts on tumor cells, non-hematopoietic cells, and immune cells. The complex downstream effects of alum-anchored IFN cooperated here to generally achieve significant anti-tumor efficacy. Nevertheless, the inherent pleiotropic nature of cytokines can be challenging in the clinic (*10*). Alum-anchoring offers a way to confine cytokine pleiotropy in a spatial manner by concentrating effects to the tumor microenvironment. Others have constrained IFN pleiotropy at a cellular level by reducing IFN signaling strength such that it is effective only if a coupled targeting moiety localizes the attenuated cytokine to a cell of interest (*20*, *21*). Further control of IFN pleiotropy may be achieved by using both spatial and cellular strategies to constrain IFN signaling.

Alum-anchored IFNs in combination with MSA-IL2 or αPD1 were highly efficacious at the primary tumor, but had distinct response to rechallenge tumors, which could be explained by T

cell phenotypes in the periphery (*72*–*77*). T cells exposed to alum-anchored IFNs can be enhanced by a secondary agent, but over-activation renders them useless in a rechallenge setting. Alum-anchored IFNα combined with MSA-IL2 had poor resistance to rechallenge, correlating with a drastic increase in SLECs, reduced MPECs, and excessive T cell activation. In contrast, alum-anchored IFNα combined with αPD1 had strong resistance to rechallenge. Further investigation is needed to see if effective immunological memory can be regained for the IL-2 combination by reducing the MSA-IL2 dose or by using tumor-localized IL-2. It will also be useful to continue studying abscopal tumors or metastases, which may require a different balance of MPECs, SLECs, and tumor-specificity.

Throughout this chapter, testing IFNs with different signaling strengths revealed further nuances of type I IFN therapies. IFNα and IFNβ performed similarly in all settings. However, Alum + ABP-IFNα differed from Alum + ABP-IFNβ in a few contexts. As a B16F10 monotherapy, the more potent Alum + ABP-IFNβ had the highest efficacy, while as an MC38 monotherapy, the less potent Alum + ABP-IFNα had superior efficacy. MC38 tumors have higher basal type I IFN signaling and immune-infiltration compared to immunologically cold B16F10 tumors (*84*–*86*). There may be a threshold for productive type I IFN signaling, and over-stimulating the pathway may be detrimental in tumors with pre-existing high IFN signatures. Future studies with more tumor models are needed to test this hypothesis. Alum + ABP-IFNα also had stronger resistance to rechallenge over Alum + ABP-IFNβ after B16F10 tumors were cured from IFNs combined with αPD1. Others have reported that over-stimulation of IFN signaling can harm response to αPD1 therapy (*51*–*53*) or MPEC formation (*87*). Although all IFNs achieved high cure rates from αPD1 at the primary tumor, the reduced resistance to rechallenge for Alum + ABP-IFNβ reflects inferior adaptive immunity from excessive type I IFN signaling. In general, Alum + ABP-IFNα achieved strong anti-tumor responses in a variety of contexts, and may be a more widely-applicable therapy. Alum + ABP-IFNβ can have added benefit, but its use is better reserved for contexts where extra IFN signaling is specifically warranted. More studies that compare type I IFN subtypes will be useful. Reducing our Alum + ABP-IFN dose from three doses to one dose may provide further insight into an effective compromise between brief and sustained signaling. Ultimately, rational design of type I IFN signaling strength, local retention, and temporal dynamics holds great promise for controlling effective anti-tumor immunity.

Figures

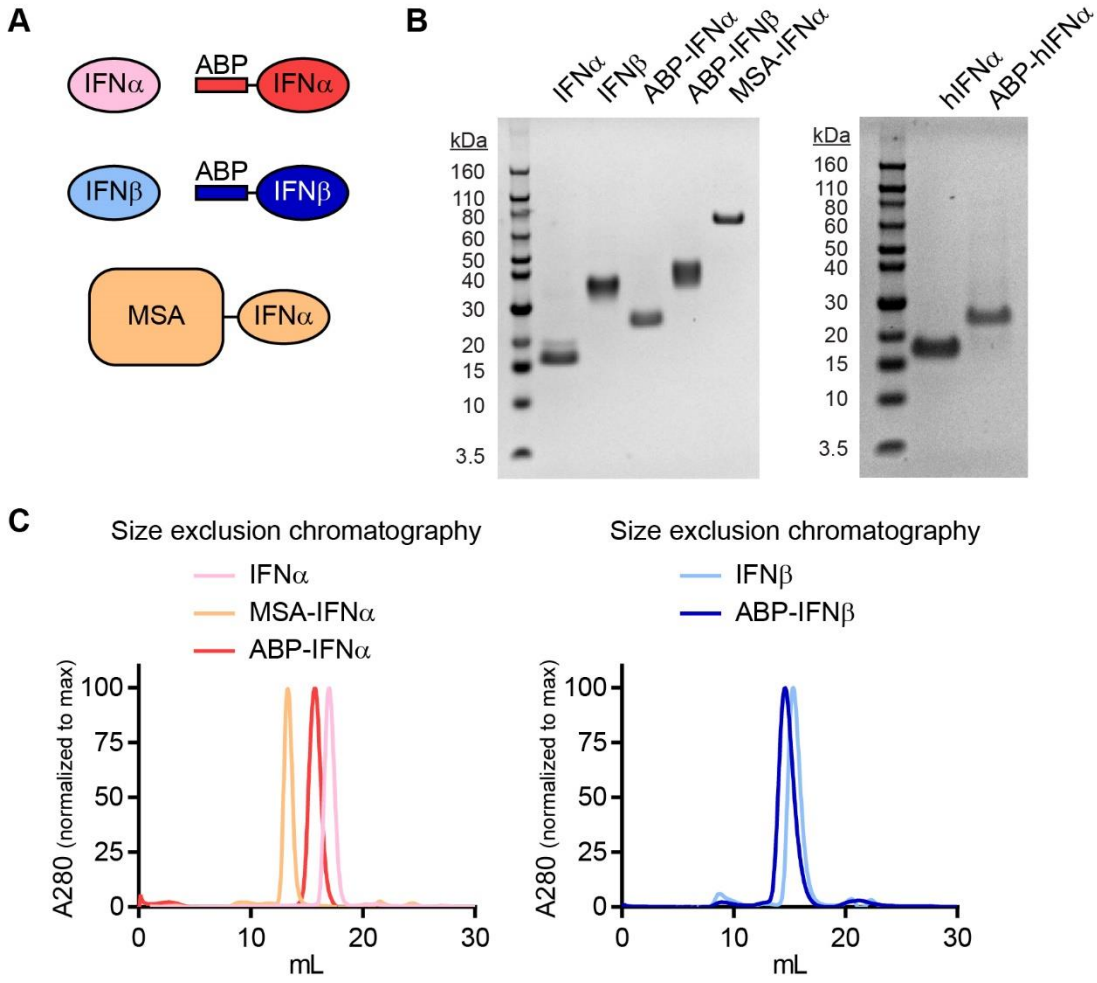

Figure 2-1: Expression of type I IFN fusions.
(**A**), Schematic of type I IFN fusion proteins. (**B**), Purified murine IFNs (left) and human IFNs (right) on a non-reducing SDS-PAGE gel with Coomassie blue stain. (**C**), Size exclusion chromatograms of 100 μg of purified murine IFNs using a Superdex200 Increase 10/300 GL column.

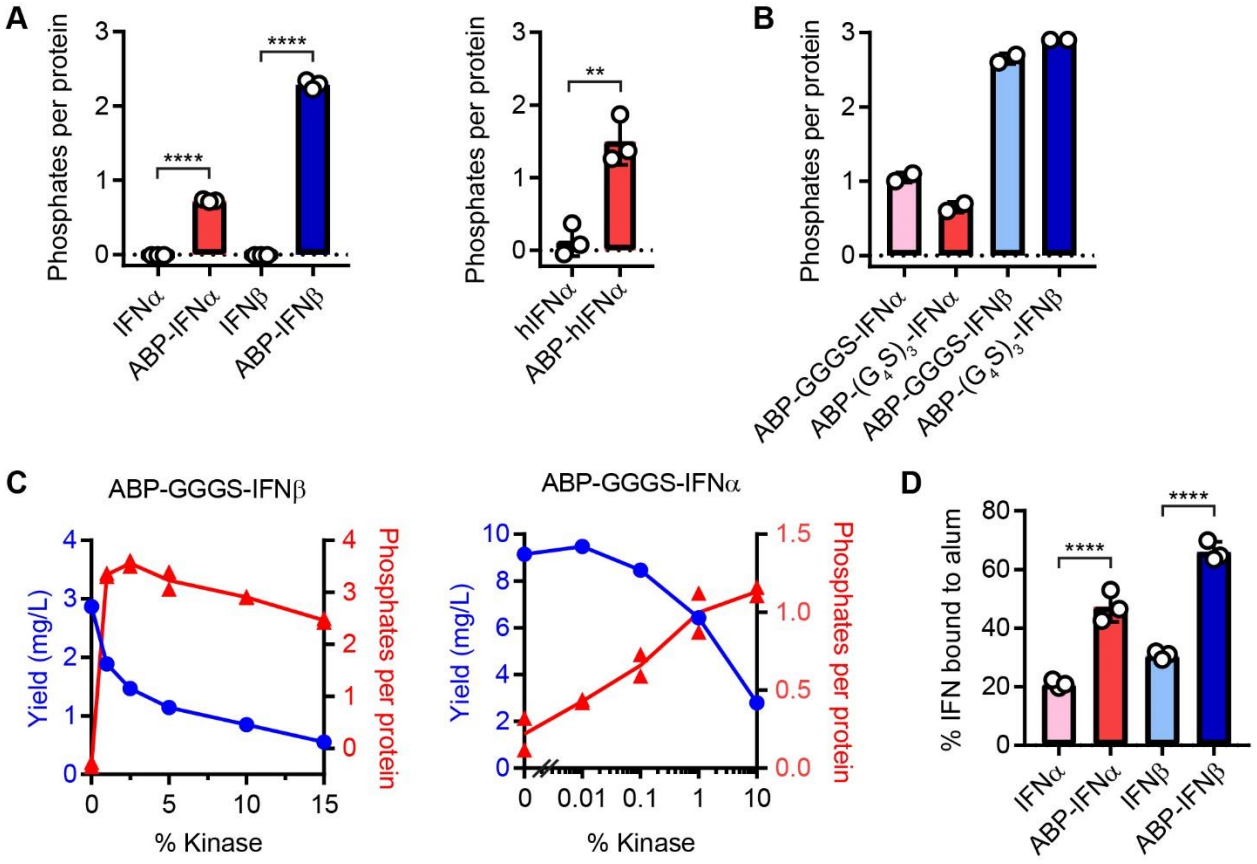

Figure 2-2: Phosphorylation and alum-binding of type I IFN fusions.
(**A**), Phosphorylation levels of murine IFNs (left) and human IFNs (right) measured by malachite green assay; mean ± SD (*n* = 3). (**B**), Phosphorylation levels of murine IFNs with different linkers measure by malachite green assay; mean (*n* = 2). (**C**) Phosphorylation levels and yields of murine IFNs with varying percentages of kinase during the transfection procedure. The conditions were expressed in parallel in small-scale HEK transfections (166 mL) (*n* = 1). (**D**), Fluorescently-labeled IFNs and alum were incubated for 20 min in TBS, then re-suspended in PBS 10% mouse serum for 1 hour. Fluorescence spectroscopy was used to measure the percentage of IFN that remained bound to alum; mean ± SD (*n* = 3). Statistics: Murine IFN phosphorylation and alum-binding compared by one-way ANOVA with Tukey's multiple comparisons test. Human IFN phosphorylation compared by one-tailed unpaired t-test. ** $P < 0.01$; **** $P < 0.0001$.

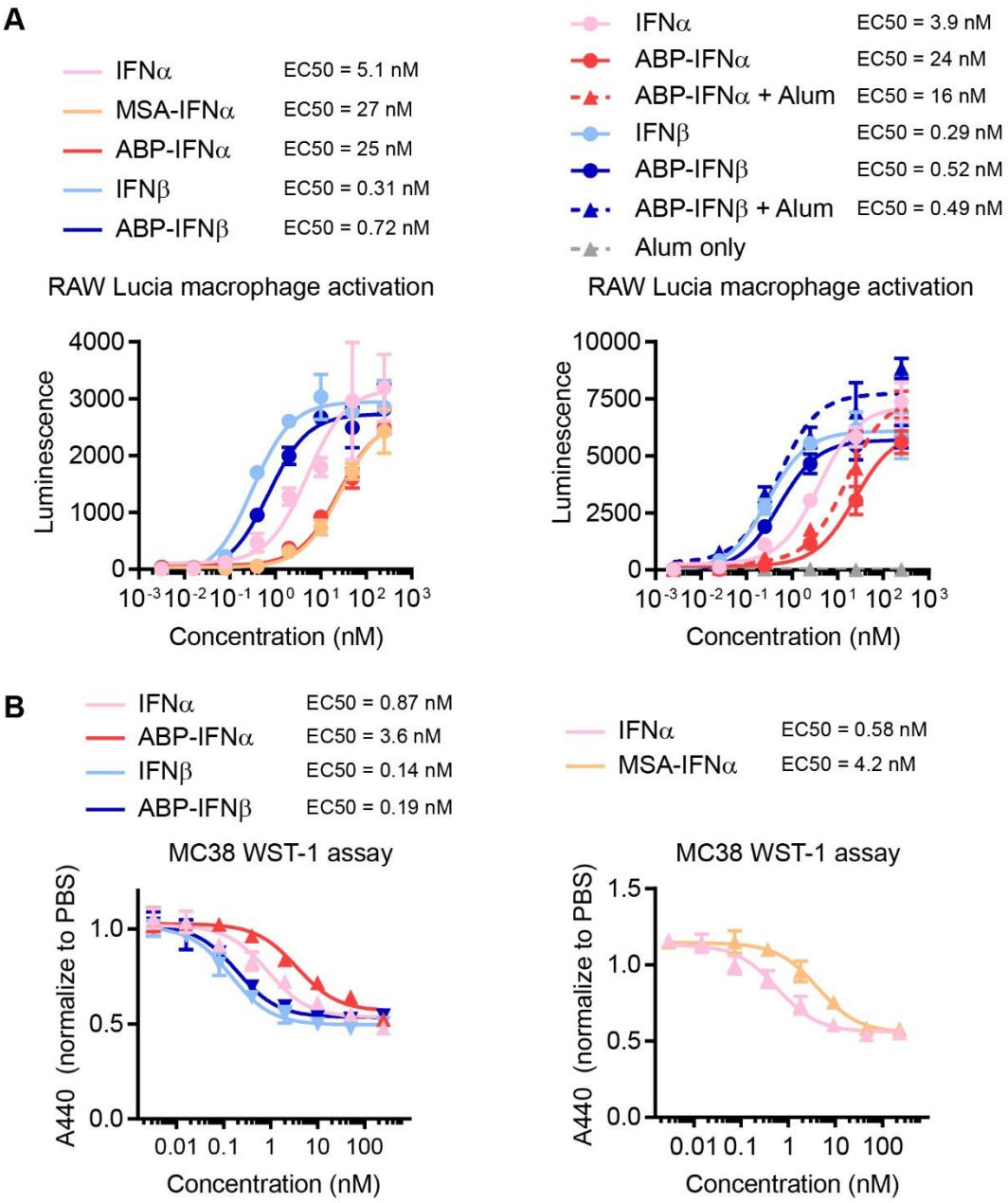

Figure 2-3: *In vitro* activity of type I IFN fusions.
Each graph shows data from one experiment. The four experiments were performed on different days. (**A**), RAW-Lucia ISG macrophage activation in response to IFNs; mean ± SD (*n* = 3). For groups with alum, alum and ABP-IFNs were mixed at a 5:1 (w/w) ratio for 20 minutes. (**B**), MC38 proliferation in response to IFNs, as measured by WST-1 assay; mean ± SD (*n* = 3).

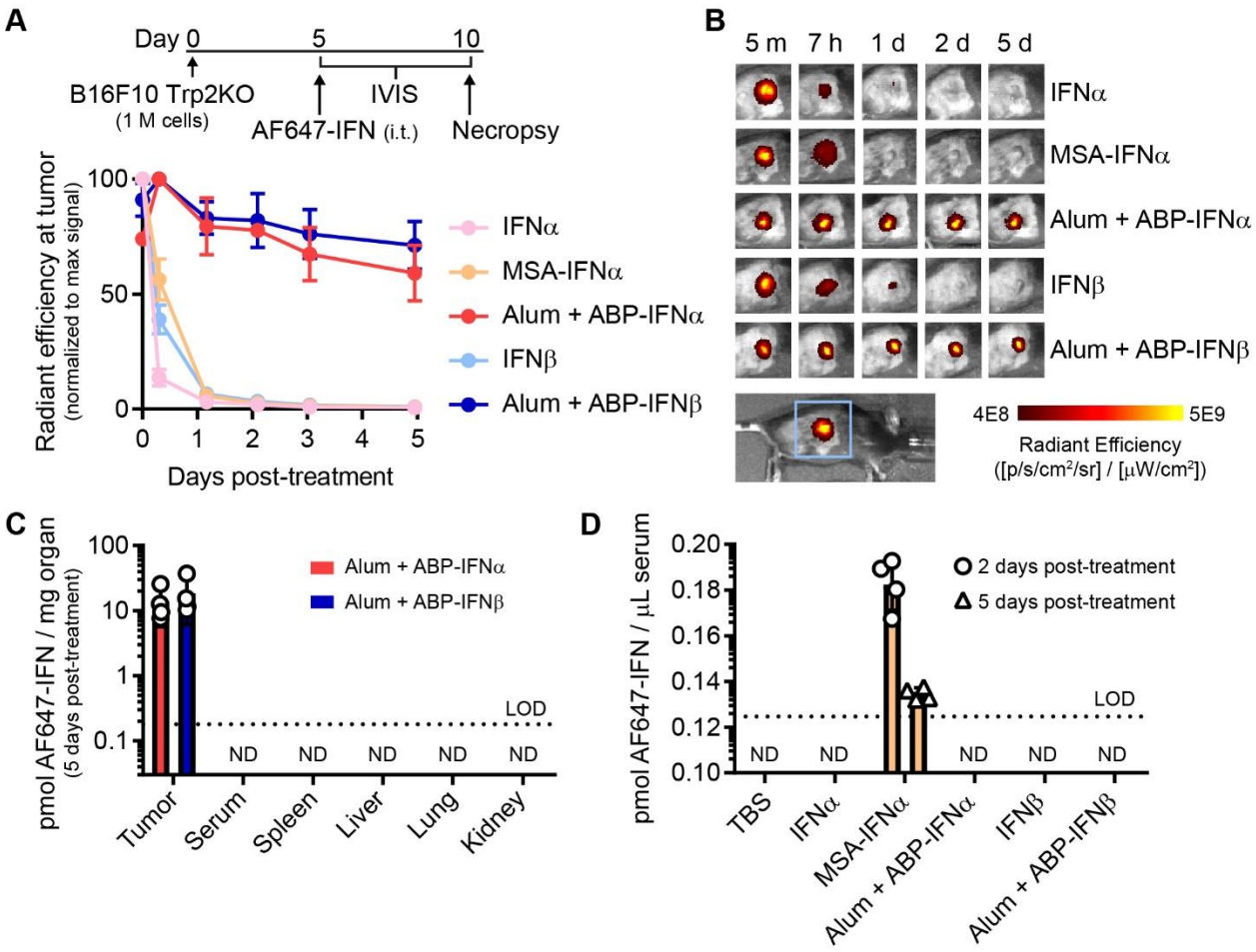

Figure 2-4: Pharmacokinetics of type I IFN fusions.
Mice bearing subcutaneous B16F10 Trp2KO tumors were injected i.t. on day 5 with 0.5 nmol AF647-labeled IFNs and tracked by *in vivo* imaging system (IVIS). (**A**), Total radiant efficiency at the tumor normalized to max signal; mean ± SD (*n* = 4). (**B**), Images of representative mice. The blue box shows the field of view around the tumor. m, minutes; h, hours; d, days. (**C** and **D**), AF647-IFN levels in (**C**), homogenized organs on day 10 and (**D**), serum on days 7 and 10, measured by fluorescence spectroscopy; mean ± SD (*n* = 4). ND, not detected; LOD, limit of detection.

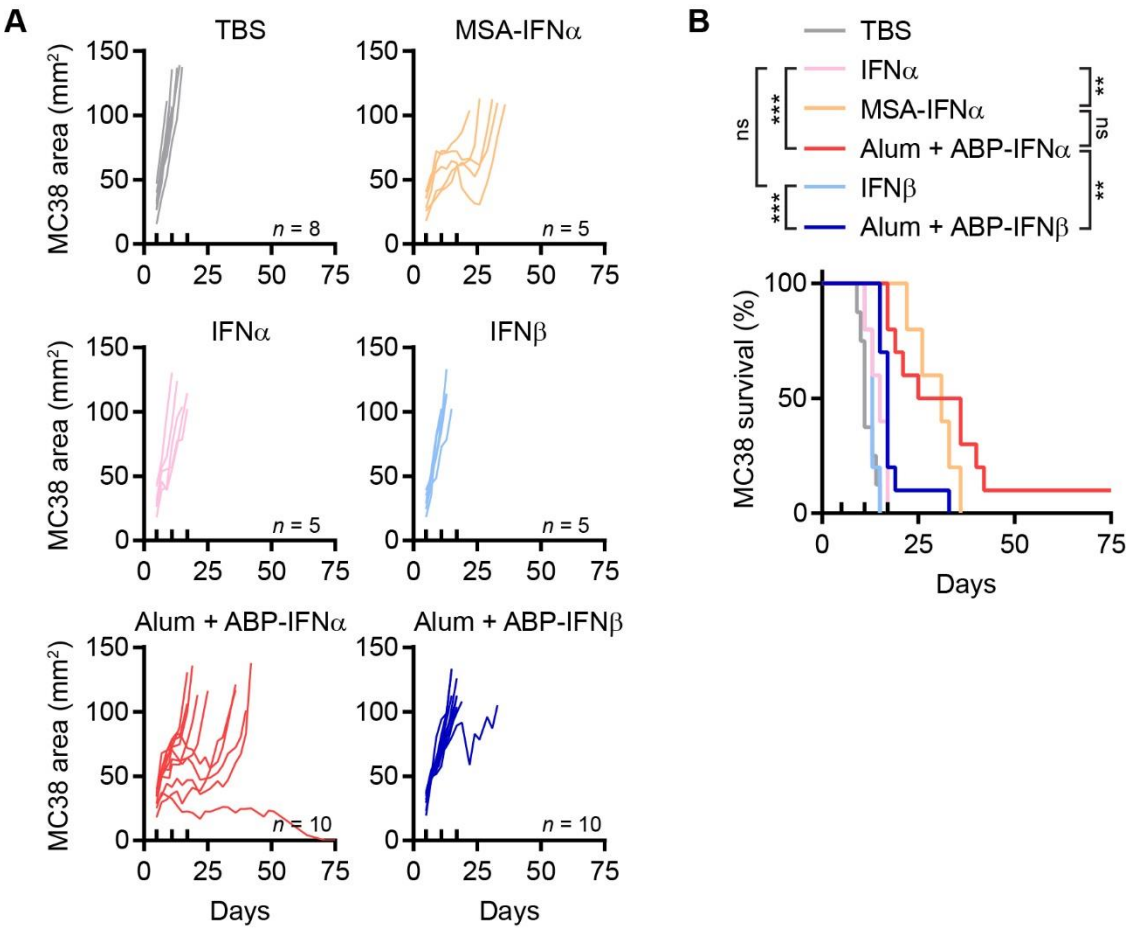

Figure 2-5: Intratumoral retention improves IFN therapy in MC38 tumors.
Mice were inoculated with 1 M MC38 cells subcutaneously on day 0. Mice were treated i.t. on days 5, 11, and 17 (ticks above x-axis) with TBS or 0.5 nmol IFN. TBS, *n* = 8; MSA-IFNα, IFNα, and IFNβ, *n* = 5; Alum + ABP-IFNα and Alum + ABP-IFNβ, *n* = 10. (**A**), Individual tumor growth curves. (**B**), Survival. Statistics: survival compared by long-rank Mantel-Cox test. ns, not significant; ** $P < 0.01$; *** $P < 0.001$.

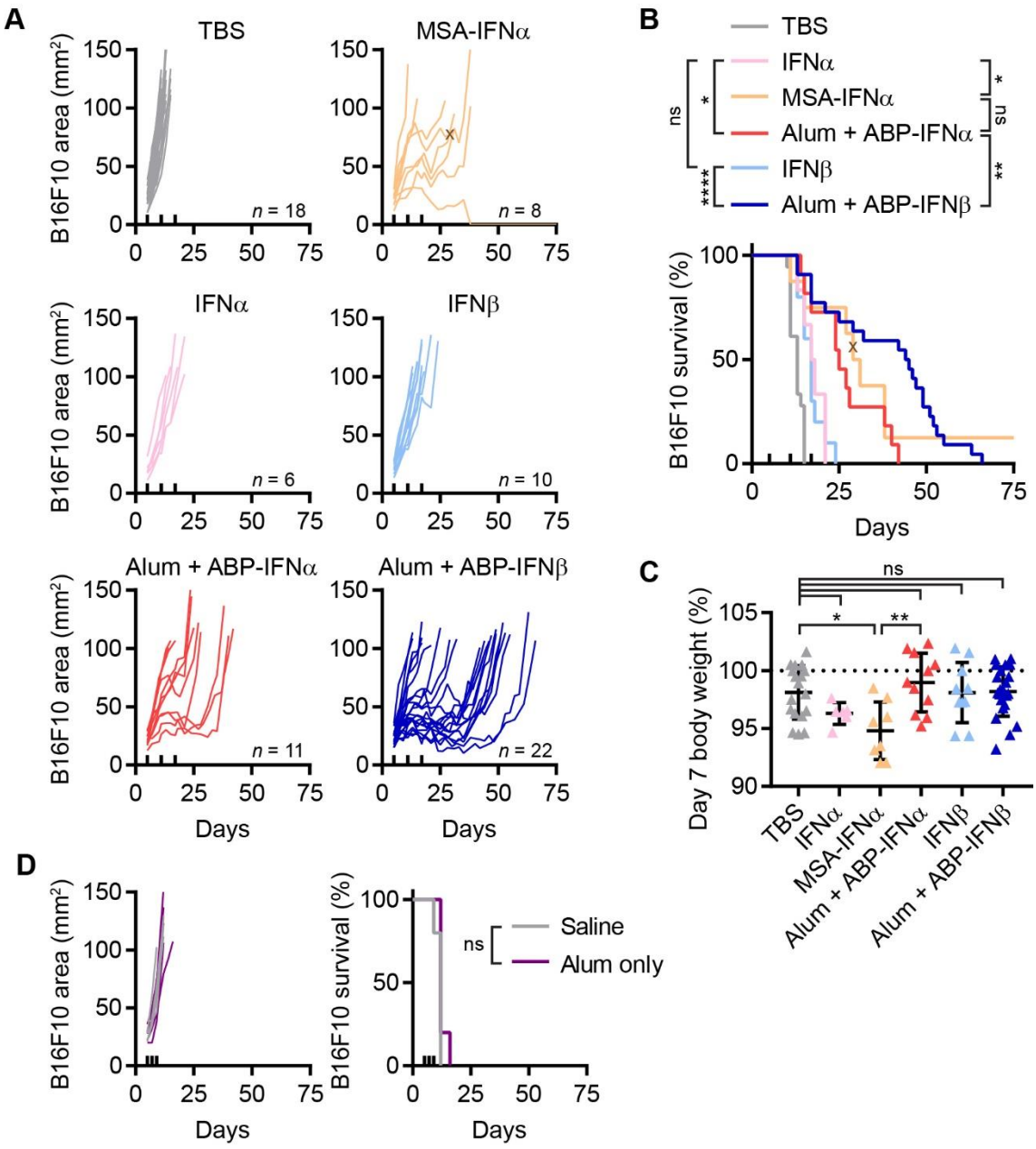

Figure 2-6: Intratumoral retention improves IFN therapy in B16F10 tumors.
(**A to C**), Mice were inoculated with 1 M B16F10 cells subcutaneously on day 0. Mice were treated i.t. on days 5, 11, and 17 (ticks above x-axis) with TBS or 0.5 nmol IFN. TBS, *n* = 18; MSA-IFNα, *n* = 8; IFNα, *n* = 6; IFNβ, *n* = 10; Alum + ABP-IFNα, *n* = 11; Alum + ABP-IFNβ, *n* = 22. "x" indicates euthanasia from poor body condition. (**A**), Individual tumor growth curves. (**B**), Survival. (**C**), Day 7 mouse body weight normalized to day 5 body weight. (**D**), Individual tumor growth and survival of mice inoculated with 1 M B16F10 cells subcutaneously on day 0 and treated i.t. with saline or a high, 120 μg dose of alum on days 5, 7, and 9 (ticks above x-axis) (*n* = 5). Statistics: survival compared by log-rank Mantel-Cox test. Weights compared by one-way ANOVA with Tukey's multiple comparisons test. ns, not significant; * $P < 0.05$; ** $P < 0.01$; **** $P < 0.0001$.

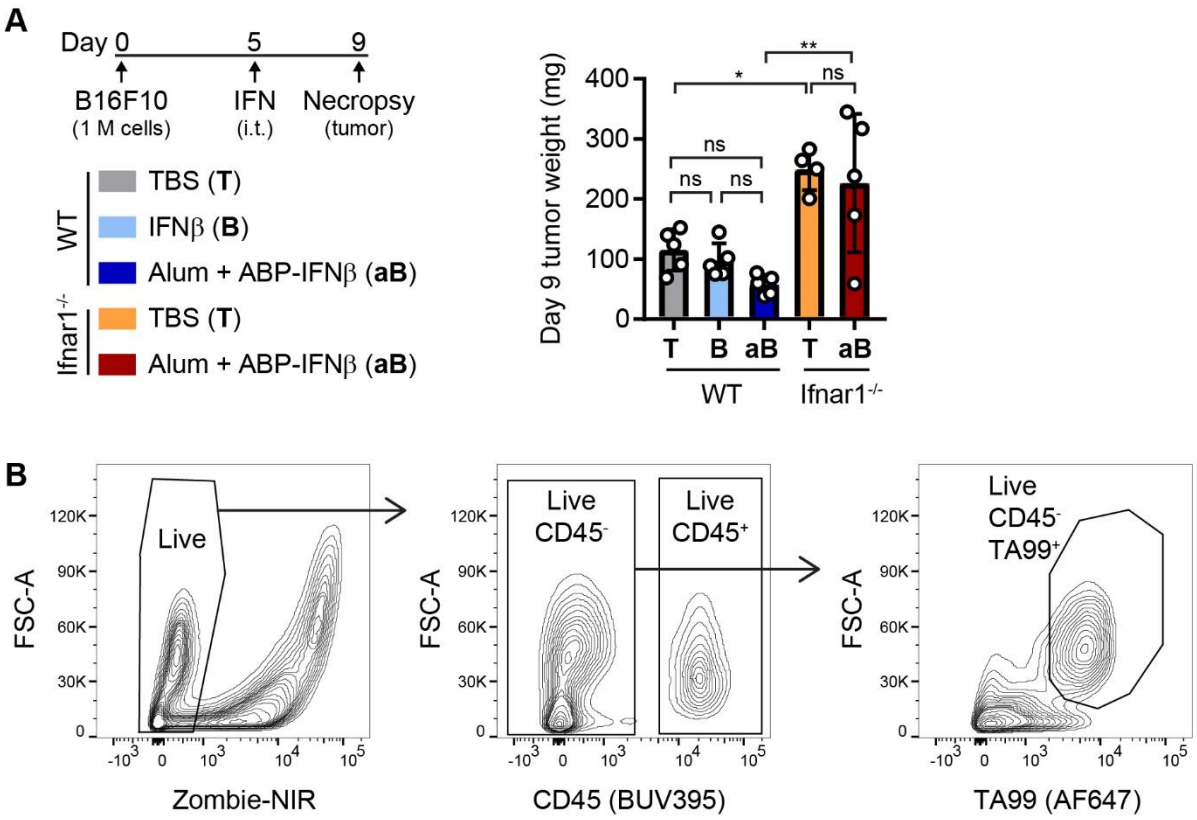

Figure 2-7: Experimental design for profiling tumor cells.
WT and Ifnar1$^{-/-}$ mice were inoculated on day 0 with 1 M B16F10 cells and treated i.t. on day 5 with TBS (T), IFNβ (B), or Alum + ABP-IFNβ (aB). On day 9, tumors were excised and analyzed by flow cytometry. TBS-treated Ifnar1$^{-/-}$ mice, n = 4; other groups, n =5. (**A**), Study timeline and weights of excised day 9 tumors. (**B**), Single cells were further gated into live immune cells (Zombie NIR^{-} CD45^{+}) and live tumor cells (Zombie NIR^{-} CD45^{-} TA99^{+}). 5% contour plots shown. Statistics: comparisons generated by one-way ANOVA with Tukey's multiple comparisons test. ns, not significant; * $P < 0.05$; ** $P < 0.01$.

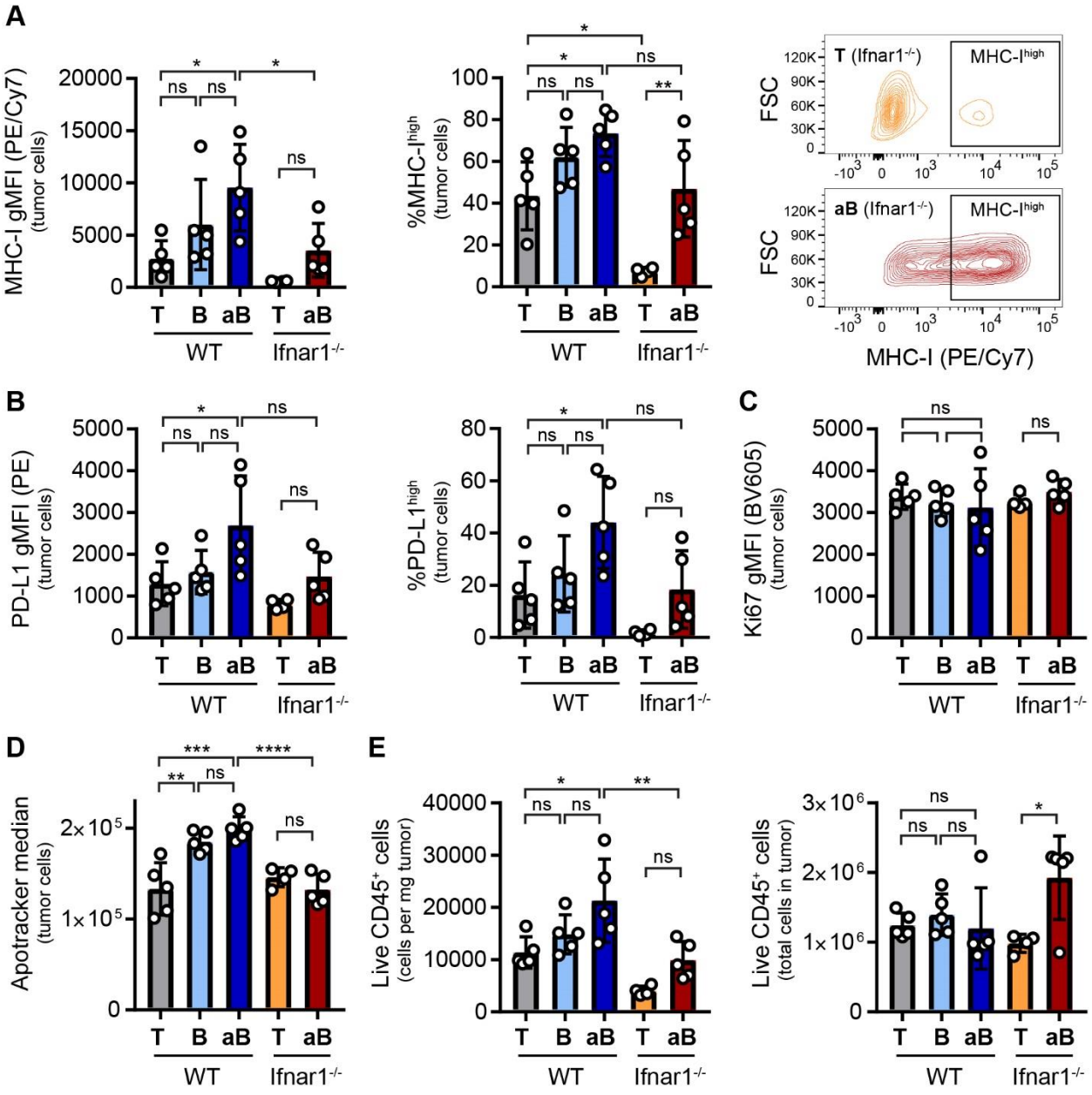

Figure 2-8: Impact of IFNβ therapies on tumor cells and immune infiltration.
B16F10 tumors were treated and analyzed by flow cytometry as described in Figure 2-7. (**A**), MHC-I levels on live tumor cells, reported as gMFI (left) and percentage of tumor cells that were MHC-I^{high} (middle). Representative MHC-I flow data (5% contour plots) for Ifnar1$^{-/-}$ mice treated with TBS or Alum + ABP-IFNβ are shown (right). (**B**), PD-L1 levels on live tumor cells, reported as gMFI (left) and percentage of tumors cells that were PD-L1^{high} (right). (**C**), Ki67 gMFI levels on live tumor cells. (**D**), Median Apotracker green levels of live tumor cells. (**E**), Immune cell counts in the tumor. Statistics: comparisons generated by one-way ANOVA with Tukey's multiple comparisons test. ns, not significant; * $P < 0.05$; ** $P < 0.01$; *** $P < 0.001$; **** $P < 0.0001$.

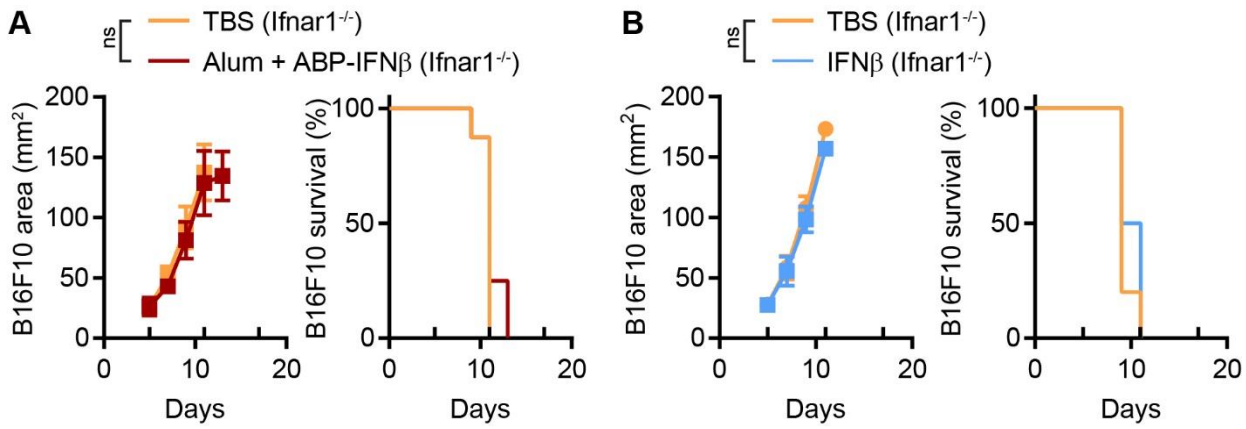

Figure 2-9: IFNβ therapies have no efficacy in Ifnar1$^{-/-}$ mice.
(**A**), Tumor growth (mean ± SD) and survival of Ifnar1$^{-/-}$ mice inoculated on day 0 with 1 M B16F10 cells and treated i.t. on days 5 and 11 (ticks above x-axis) with TBS (*n* = 8) or Alum + ABP-IFNβ (*n* = 8). All tumors exceeded 100 mm^2 before the typical third dose. (**B**), Tumor growth (mean ± SD) and survival of Ifnar1$^{-/-}$ mice inoculated on day 0 with 1 M B16F10 cells and treated i.t. on days 5 and 11 (ticks above x-axis) with TBS (*n* = 5) or ABP-IFNβ (*n* = 6). All tumors exceeded 100 mm^2 before the typical third dose.

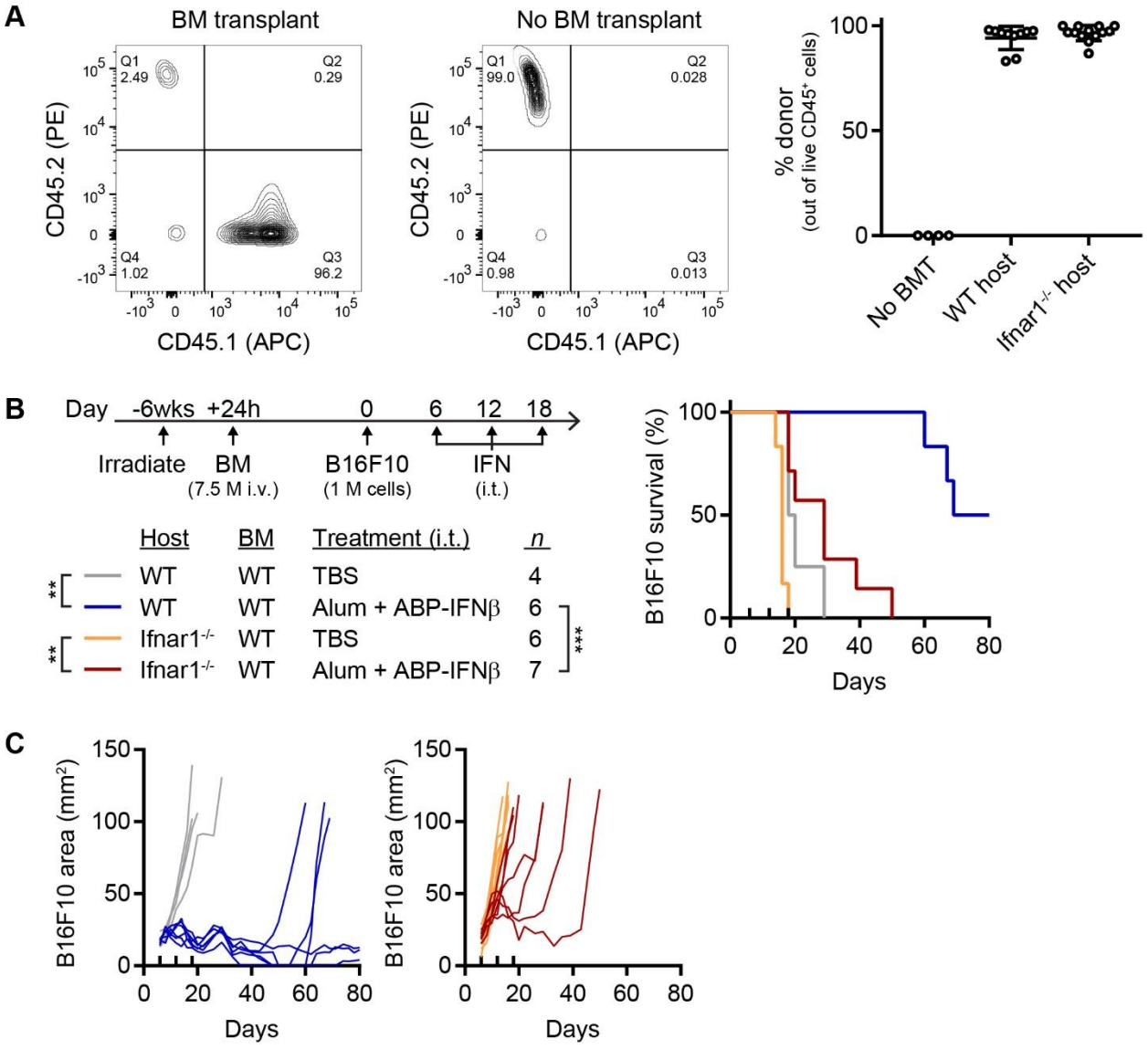

Figure 2-10: Efficacy of Alum + ABP-IFNβ relies on non-hematopoietic cells.
WT and Ifnar1$^{-/-}$ host mice (CD45.2^{+}) were lethally irradiated, followed by bone marrow transplant (BMT) (7.5 M cells i.v.) from congenically marked donor mice (CD45.1^{+}) the next day. (**A**), After 6 weeks, engraftment was confirmed by analyzing CD45.1 and CD45.2 levels from cheek bleeds via flow cytometry. Representative data of live single cells shown for a mouse that received BMT and a control mouse that had no irradiation or BMT (2% contour plots). The percentage of live CD45^{+} cells (CD45.1^{+} or CD45.2^{+}) that were donor cells (CD45.1^{+} CD45.2^{-}) are reported for all mice. No BMT controls, *n* = 4; WT host, *n* = 10; Ifnar1$^{-/-}$ host, *n* = 13. (**B**), Survival and (**C**), individual tumor growth for mice inoculated on day 0 with 1 M B16F10 cells and treated i.t. with TBS or Alum + ABP-IFNβ on days 6, 12, and 18 (ticks above x-axis); *n* indicated on plot. Statistics: survival compared by log-rank Mantel-Cox test. ** $P < 0.01$; *** $P < 0.001$.

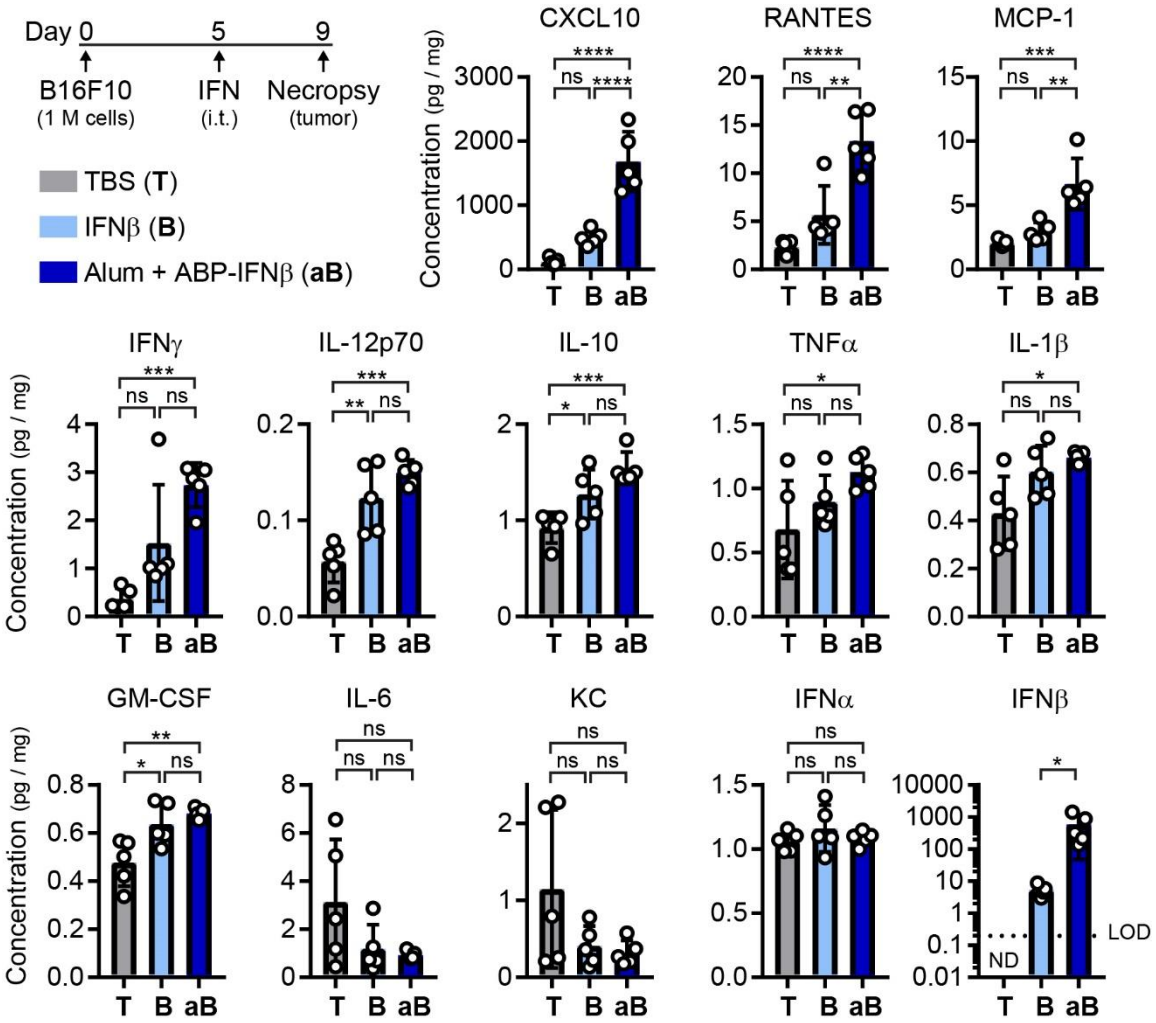

Figure 2-11: Chemokines and cytokines in tumor lysates following IFNβ therapies. Mice were inoculated on day 0 with 1 M B16F10 cells and treated i.t. on day 5 with TBS, IFNβ, or Alum + ABP-IFNβ. On day 9, tumors were excised and homogenized. Cytokine and chemokine levels in tumor lysates were measured by LEGENDplex, reported as pg analyte per mg tumor; mean ± SD (n = 5). Note that for IFNβ only, concentrations are shown on a log scale. ND, not detected; LOD, limit of detection. Statistics: IFNβ levels compared by one-tailed unpaired t-test. Other comparisons generated by one-way ANOVA with Tukey's multiple comparisons test. ns, not significant; * $P < 0.05$; ** $P < 0.01$; *** $P < 0.001$; **** $P < 0.0001$.

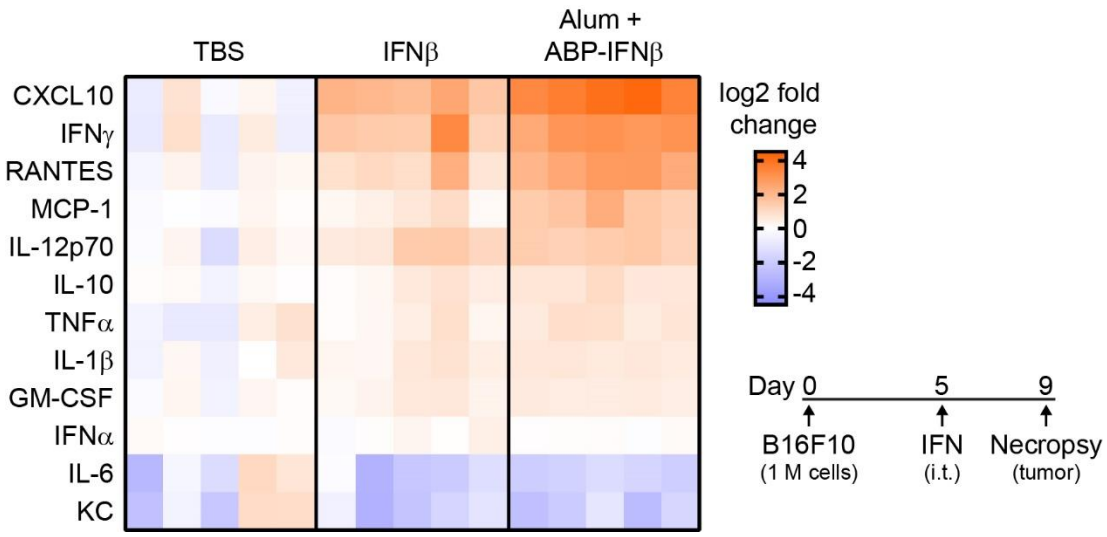

Figure 2-12: Heatmap of chemokines and cytokines in tumor lysates.
Chemokines and cytokine levels in B16F10 tumor lysates were measured as described in Figure 2-11. Heatmap columns show data from individual mice (*n* = 5), reported as log2 fold change in concentration compared to the average value of the TBS group. Data for IFNβ was not included in the heatmap because no signal was detected for any TBS mouse, and the marker was specific for the treatment administered. Raw data is shown in Figure 2-11.

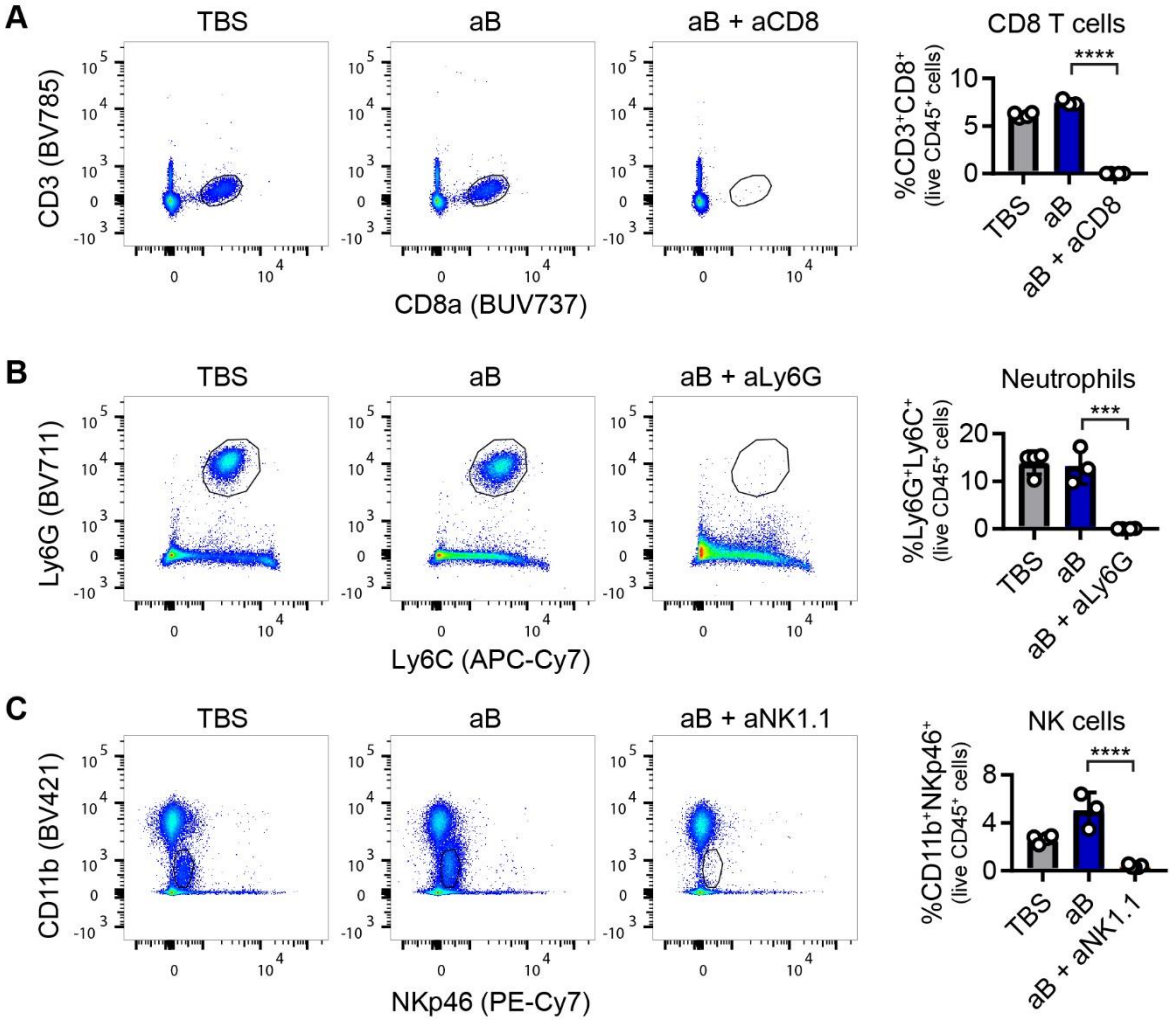

Figure 2-13: Confirmation of antibody-mediated depletions.
Mice were inoculated on day 0 with 1 M B16F10 cells and treated i.t. with TBS or Alum + ABP-IFNβ (aB) on days 5, 11, and 17. Some mice received depleting antibodies every 4 days from day 3 to day 30. To confirm antibody-mediated depletions, flow cytometry was used to analyze blood on day 9 from a subset of TBS-treated mice (n = 4), and Alum + ABP-IFNβ-treated mice with no depletions (n = 3), aCD8 (n = 4), aLy6G (n = 4), and aNK1.1 (n = 5). Shown are representative flow plots of live CD45$^+$ cells, and the percentages of live CD45$^+$ cells that were (**A**), CD3$^+$ CD8$^+$ T cells, (**B**), Ly6G$^+$ Ly6C$^+$ neutrophils, and (**C**), CD11b$^+$ Nkp46$^+$ NK cells. Statistics: comparisons generated by one-way ANOVA with Tukey's multiple comparisons test. *** $P < 0.001$; **** $P < 0.0001$.

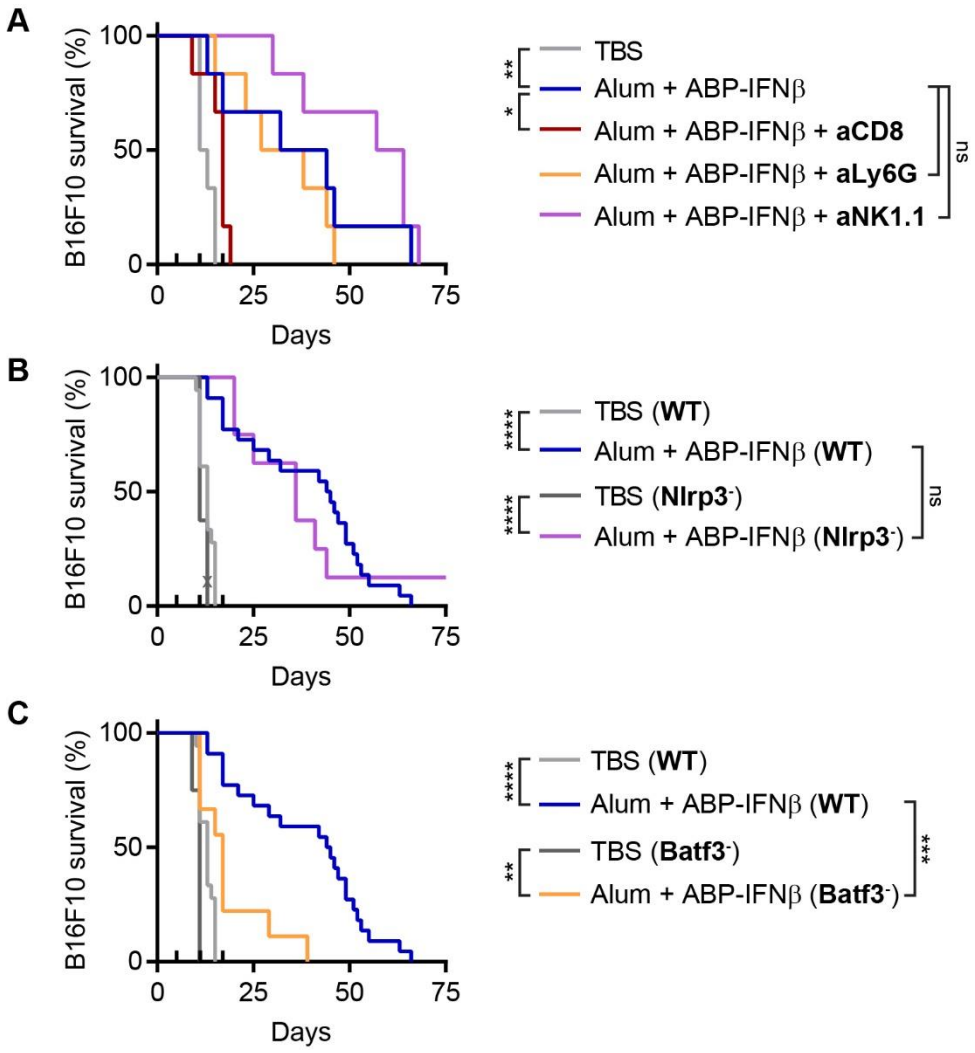

Figure 2-14: Alum + ABP-IFNβ relies on DCs and CD8+ T cells.
All mice were inoculated on day 0 with 1 M B16F10 cells. Mice were treated i.t. with TBS or Alum + ABP-IFNβ on days 5, 11, and 17 (ticks above x-axis). (**A**), Survival of mice receiving antibody-mediated depletions every 4 days from day 3 to 30 (n = 6). Antibody-mediated depletions were confirmed in Figure 2-13. (**B**), Survival of WT mice treated with TBS (n = 18) or Alum + ABP-IFNβ (n = 22), and Nlrp3$^{-/-}$ mice treated with TBS (n = 8) or Alum + ABP-IFNβ (n = 8). "x" indicates euthanasia from poor body condition. (**C**), Survival of WT mice treated with TBS (n = 18) or Alum + ABP-IFNβ (n = 22), and Batf3$^{-/-}$ mice treated with TBS (n = 8) or Alum + ABP-IFNβ (n = 9). Statistics: survival compared by log-rank Mantel-Cox test. ns, not significant; * P < 0.05; ** P < 0.01; *** P < 0.001; **** P < 0.0001.

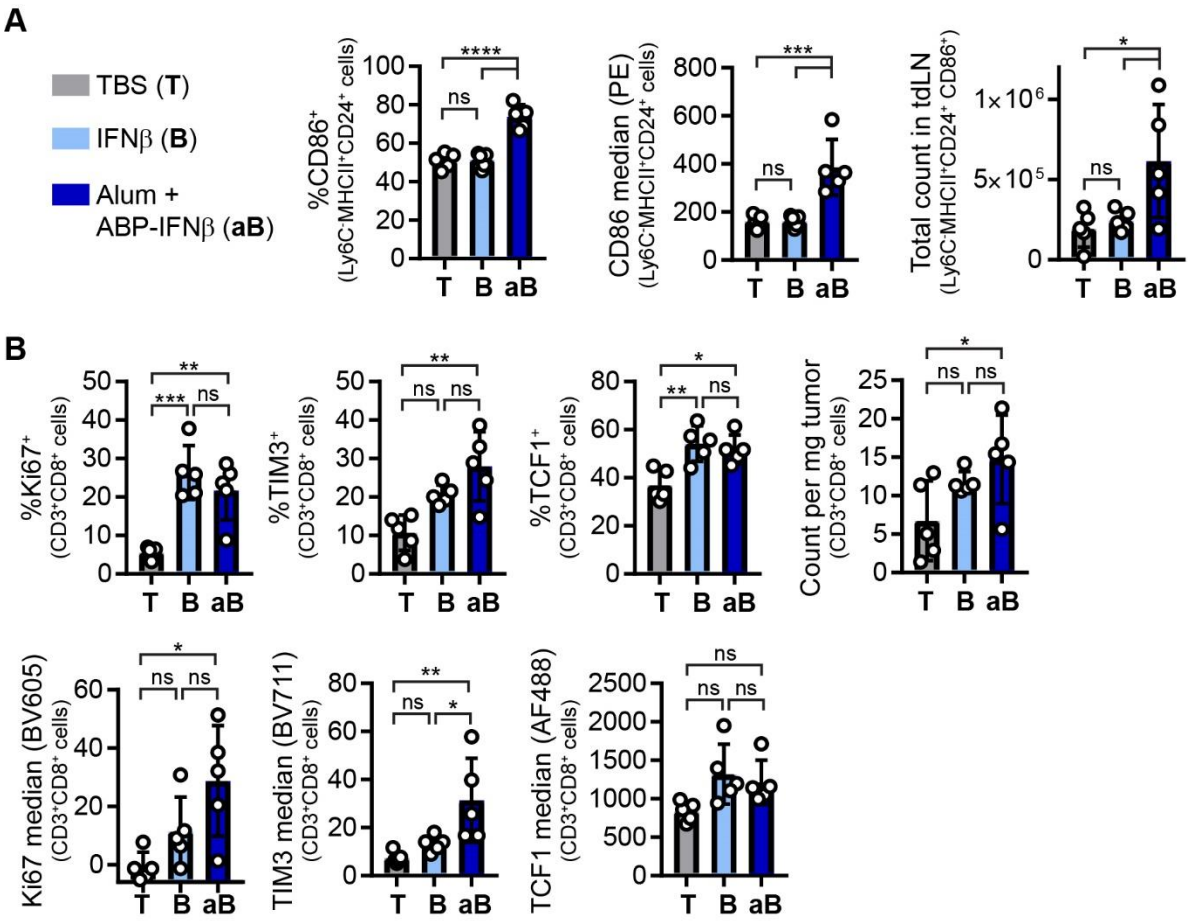

Figure 2-15: Alum + ABP-IFNβ activates DCs and CD8+ T cells.
(**A**), B16F10-bearing mice were treated i.t. on day 5 with TBS, IFNβ, or Alum + ABP-IFNβ. On day 9, tumor draining lymph nodes were excised and analyzed via flow cytometry. Reported are percentage of Ly6C$^-$ MHCII$^+$ CD24$^+$ DCs in the tdLN that were CD86$^+$ (left), median CD86 levels on Ly6C$^-$ MHCII$^+$ CD24$^+$ DCs in the tdLN (middle), and total count of Ly6C$^-$ MHCII$^+$ CD24$^+$ CD86$^+$ cells in the tdLN. Mean ± SD (*n* = 5). (**B**), B16F10-bearing mice were treated i.t. on day 5 with TBS, IFNβ, or Alum + ABP-IFNβ. On day 11, tumors were excised and analyzed via flow cytometry. Ki67, TIM3, and TCF1 levels of CD3$^+$ CD8$^+$ cells in the tumor are reported as percent positive (top) and median (bottom). CD3$^+$ CD8$^+$ cell count per mg tumor is also reported. Mean ± SD (*n* = 5). Statistics: comparisons generated by one-way ANOVA with Tukey's multiple comparisons test. ns, not significant; * $P < 0.05$; ** $P < 0.01$; *** $P < 0.001$; **** $P < 0.0001$.

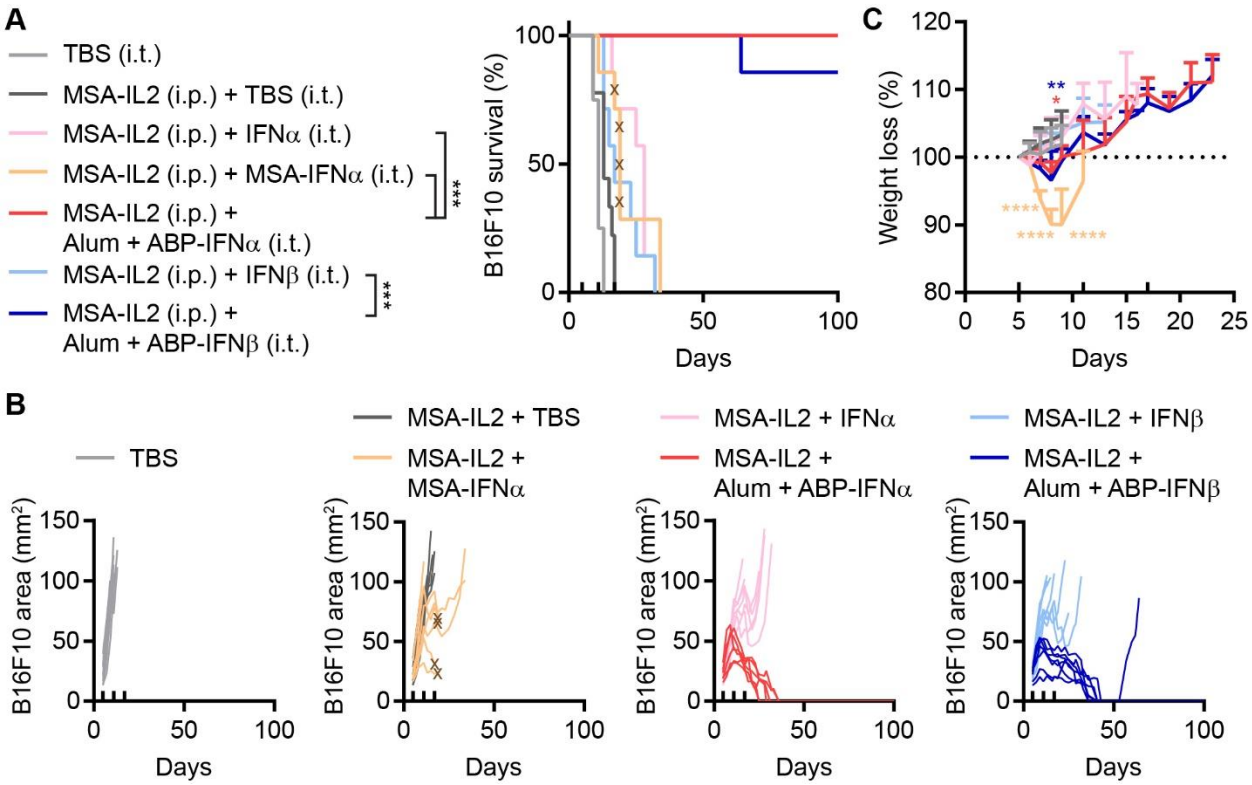

Figure 2-16: IFNs in combination with MSA-IL2.
Mice were inoculated on day 0 with 1 M B16F10 cells. Mice were treated on days 5, 11 and 17 (ticks above x-axis) with 30 μg MSA-IL2 (i.p.) and 0.5 nmol IFN (i.t.). TBS, *n* = 8; MSA-IL2 + TBS, *n* = 9; other groups, *n* = 6 or 7. (**A**), Survival. "x" marks euthanasia from poor body condition or weight loss. (**B**), Tumor growth curves of individual mice. (**C**), Body weight normalized to day 5 until a mouse in that group was euthanized; mean + SD. Statistics show comparisons to TBS. Statistics: survival compared by log-rank Mantel-Cox test. Weights compared by two-way ANOVA with Tukey's multiple comparisons test. ns, not significant; * $P < 0.05$; ** $P < 0.01$; *** $P < 0.001$; **** $P < 0.0001$.

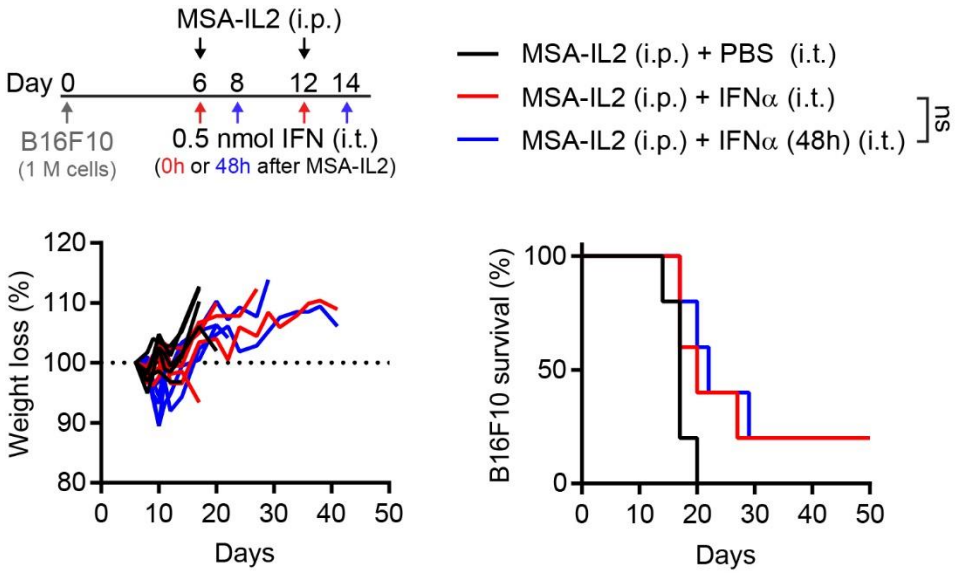

Figure 2-17: Relative timing of IFNα and MSA-IL2.
Mice bearing B16F10 tumors were treated on days 6 and 12 with 30 μg MSA-IL2 (i.p.). Mice were treated with 0.5 nmol IFNα i.t. on either days 6 and 12, or on days 8 and 14. Weight loss curves of individual mice (left), and overall survival (right); *n* = 5. Statistics: survival compared by log-rank Mantel-Cox test. ns, not significant.

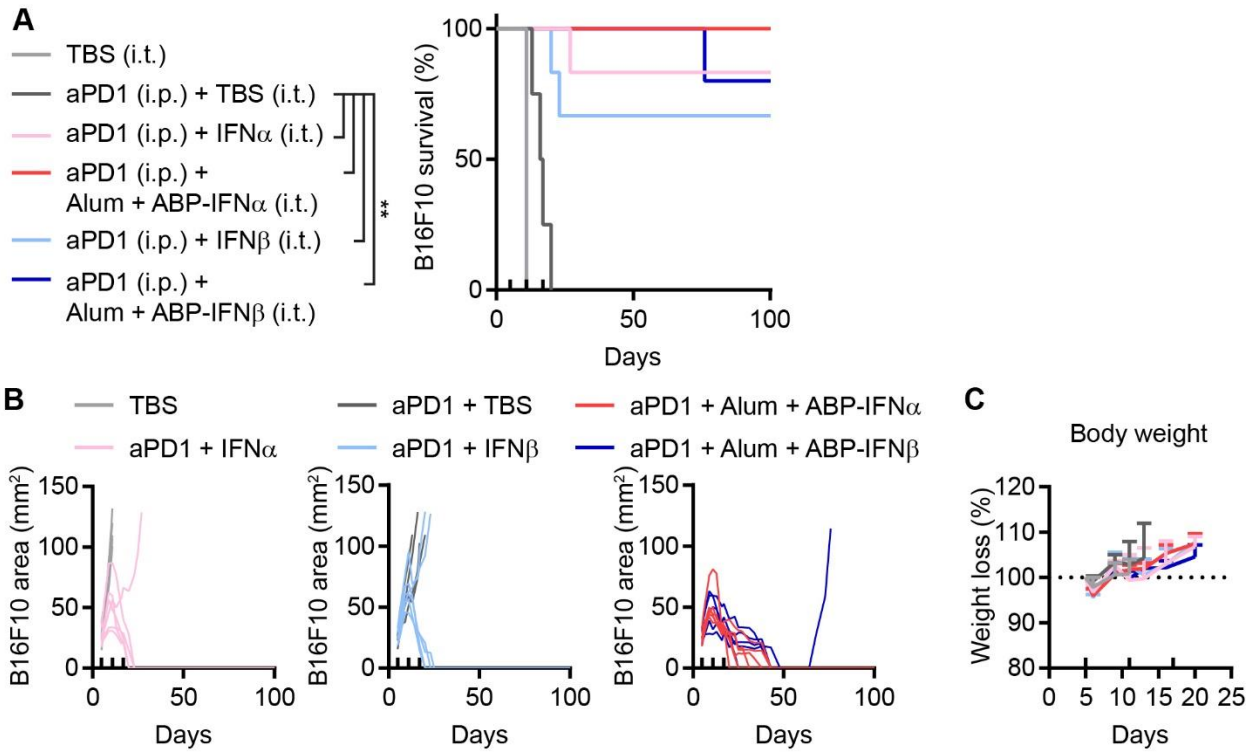

Figure 2-18: IFNs in combination with αPD1.
Mice were inoculated on day 0 with 1 M B16F10 cells. Mice were treated on days 5, 11, and 17 with αPD1 (i.p.) and IFN (i.t.). αPD1 + TBS, *n* = 4; other groups, *n* = 5 or 6. (**A**), Survival. (**B**), Tumor growth curves of individual mice. (**C**), Body weight normalized to day 5 until a mouse in that group was euthanized; mean + SD. Statistics: survival compared by log-rank Mantel-Cox test. ** $P < 0.01$.

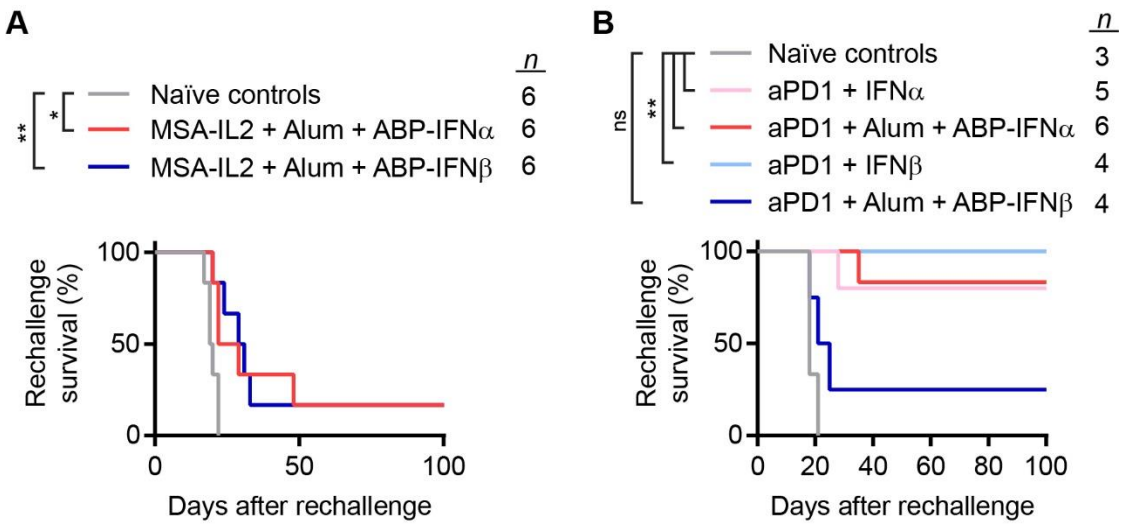

Figure 2-19: Combination immunotherapies yield contrasting memory responses. Rechallenge survival of cured mice from (**A**), the MSA-IL2 combination study from Figure 2-16, and (**B**), the αPD1 combination study from Figure 2-18, along with naïve control mice. Mice were rechallenged with 0.1 M B16F10 cells on the opposite flank and received no further treatment. *n* indicated on plot. Statistics: survival compared by log-rank Mantel-Cox test. ns, not significant; * $P < 0.05$; ** $P < 0.01$.

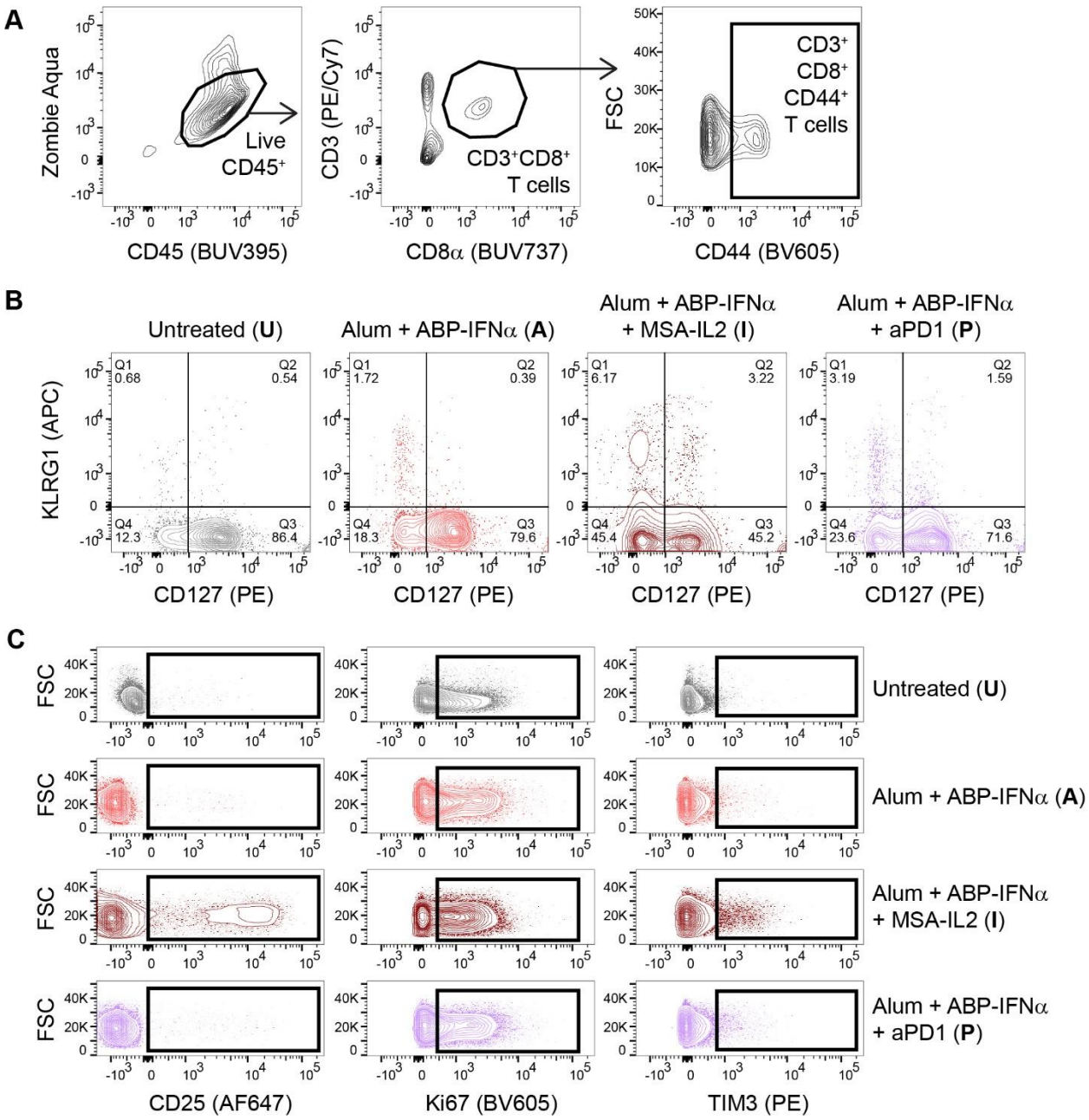

Figure 2-20: Flow cytometry gating for T cell memory response.
Mice were inoculated on day 0 with 1 M B16F10 cells and treated on days 5 and 11 with Alum + ABP-IFNα (i.t.) and 30 μg MSA-IL2 or 200 μg αPD1 (i.p.). On day 13, spleens were excised and analyzed by flow cytometry. Untreated, *n* = 4; all other groups, *n* = 5. (**A**), Single cells were further gated into live $CD3^+$ $CD8^+$ T cells and $CD3^+$ $CD8^+$ $CD44^+$ T cells. 5% contour plots shown. (**B**), One panel was used to assess MPECs and SLECs. Representative quadrants for CD127 and KLRG1 levels of $CD3^+$ $CD8^+$ $CD44^+$ T cells (5% contour plots with outliers shown). (**C**), A second panel was used to assess additional markers on T cells. Representative flow data for CD25, Ki67, and TIM3 levels on $CD3^+$ $CD8^+$ T cells (5% contour plots with outliers shown). Boxes show gating strategy used to determine percentage positive.

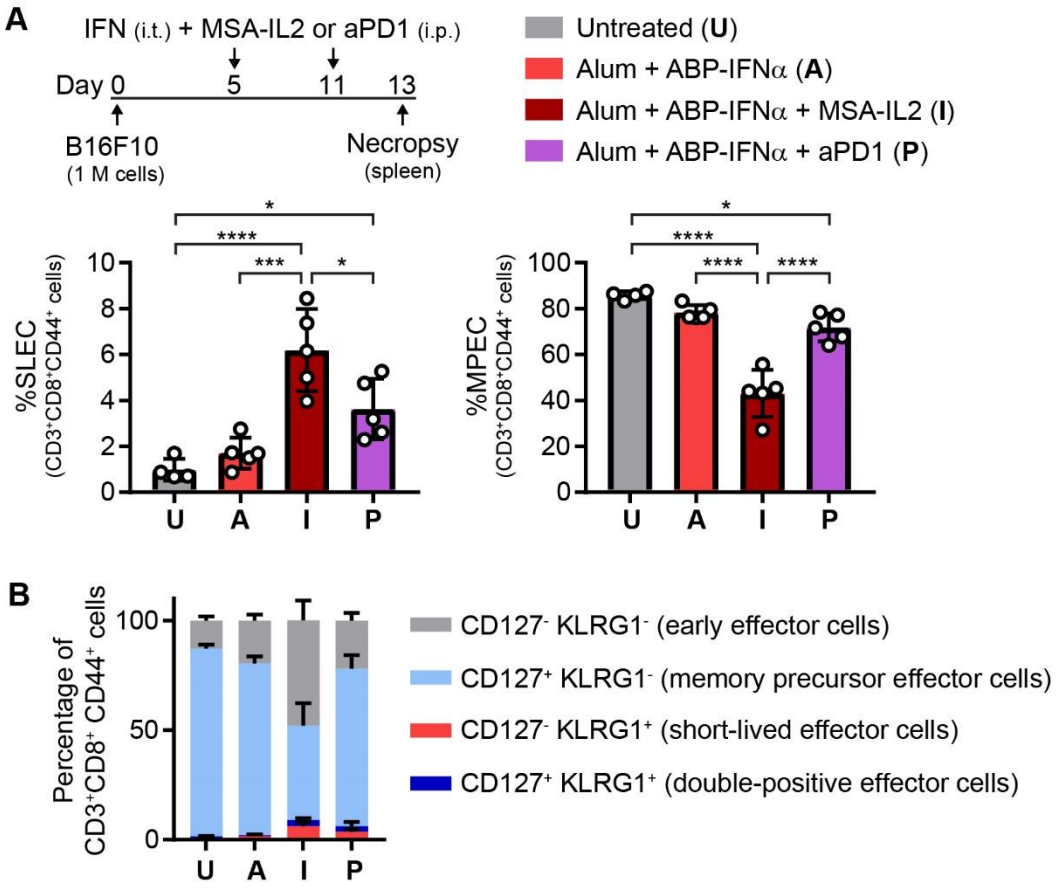

Figure 2-21: MPECs and SLECs following combination immunotherapies.
Mice were inoculated on day 0 with 1 M B16F10 cells and treated on days 5 and 11 with Alum + ABP-IFNα (i.t.) and 30 μg MSA-IL2 or 200 μg αPD1 (i.p.). On day 13, spleens were excised and analyzed by flow cytometry as described in Figure 2-20. Untreated, $n = 4$; all other groups, $n = 5$. (**A**), Proportion $CD127^-$ $KLRG1^+$ SLECs (left) and $CD127^+$ $KLRG1^-$ MPECs (right) out of $CD3^+$ $CD8^+$ $CD44^+$ cells; mean ± SD. (**B**), Proportion of all four CD127 and KLRG1 quadrants; mean + SD. Statistics: comparisons generated by one-way ANOVA with Tukey's multiple comparisons test. * $P < 0.05$; *** $P < 0.001$; **** $P < 0.0001$.

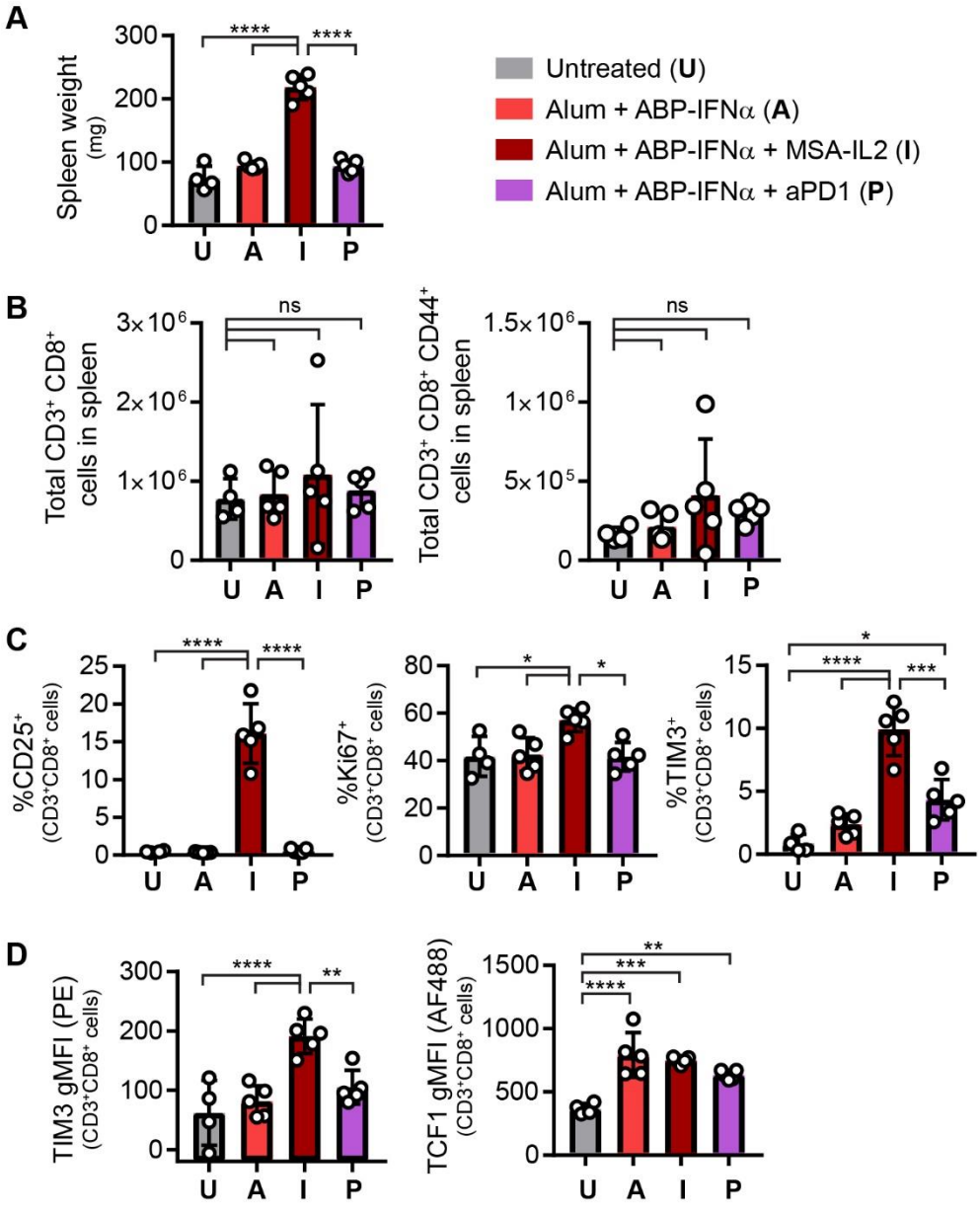

Figure 2-22: T cell phenotype following combination immunotherapies.
Mice were inoculated on day 0 with 1 M B16F10 cells and treated on days 5 and 11 with Alum + ABP-IFNα (i.t.) and 30 μg MSA-IL2 or 200 μg αPD1 (i.p.). On day 13, spleens were excised and analyzed by flow cytometry as described in Figure 2-20. Untreated, *n* = 4; all other groups, *n* = 5. (**A**), Day 13 spleen weight; mean ± SD. (**B**), Total $CD3^+$ $CD8^+$ and $CD3^+$ $CD8^+$ $CD44^+$ T cell counts in spleen; mean ± SD. (**C**), Proportion $CD25^+$, $Ki67^+$ and $TIM3^+$ out of $CD3^+$ $CD8^+$ cells; mean ± SD. (**D**), gMFI of TIM3 and TCF1 levels on $CD3^+$ $CD8^+$ T cells; mean ± SD. Statistics: comparisons generated by one-way ANOVA with Tukey's multiple comparisons test. ns, not significant; * $P < 0.05$; ** $P < 0.01$; *** $P < 0.001$; **** $P < 0.0001$.

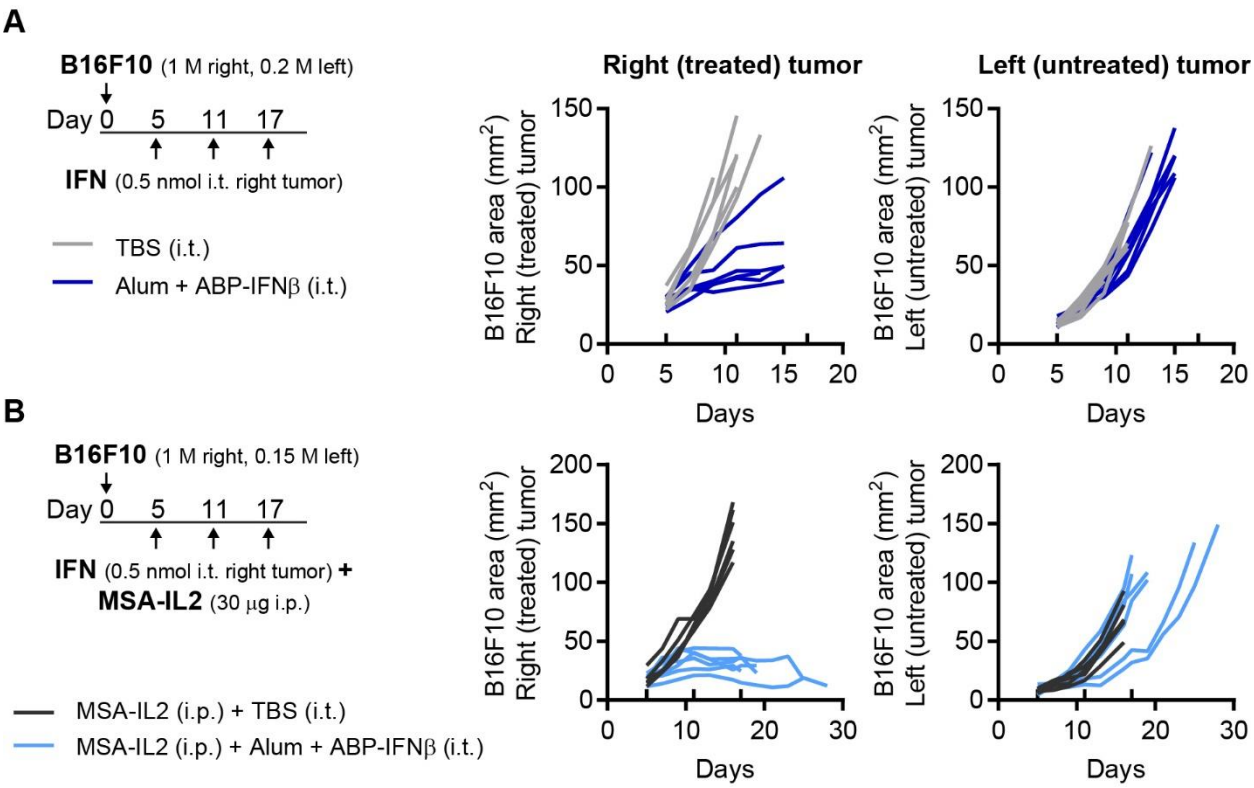

Figure 2-23: Intratumoral IFN therapies in mice bearing two B16F10 tumors.
On day 0, mice were inoculated subcutaneously with B16F10 tumors on both the right and left flanks. On days indicated (ticks above x-axis), mice were treated with TBS or 0.5 nmol IFN intratumorally in the right tumor only. (**A**), Tumor growth curves of B16F10-bearing mice until either tumor exceeded 100 mm^2. The average tumor area on day 5 was 27 mm^2 (right) and 13 mm^2 (left). *n* = 6. (**B**), Tumor growth curves of B16F10-bearing mice until either tumor exceeded 100 mm^2. Mice also received MSA-IL2 (i.p.). The average tumor area on day 5 was 18 mm^2 (right) and 8 mm^2 (left). *n* = 6.

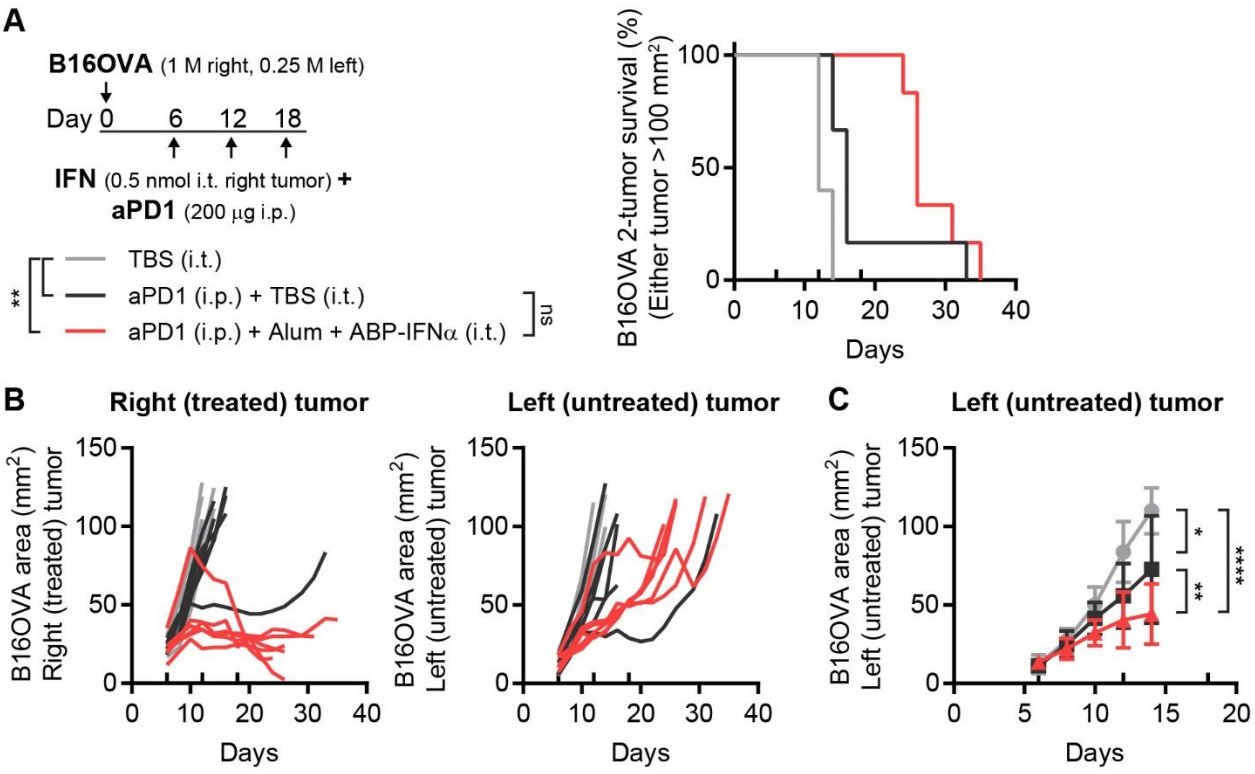

Figure 2-24: Intratumoral IFN therapies in mice bearing two B16OVA tumors.
On day 0, mice were inoculated subcutaneously with B16OVA tumors on both the right and left flanks. On days indicated (ticks above x-axis), mice were treated with TBS or 0.5 nmol IFN intratumorally in the right tumor only. Some mice also received αPD1 (i.p.). TBS only, $n = 5$; other groups, $n = 6$. (**A**), Survival until either tumor exceeded 100 mm^2. Statistics: survival compared by log-rank Mantel-Cox test. ns, not significant; ** $P < 0.01$. (**B**), Tumor growth for individual mice until either tumor exceeded 100 mm^2. The average tumor area on day 6 was 23 mm^2 (right) and 12 mm^2 (left). (**C**) Average tumor area until day 14; mean ± SD. Statistics: tumor area comparisons generated by two-way ANOVA with Tukey's multiple comparisons test; showing comparisons for day 14. * $P < 0.05$; ** $P < 0.01$; **** $P < 0.0001$.

Table 2-1 Amino acid sequences for type I IFN fusion proteins.
IFNα shown in pink. IFNβ shown in blue. MSA shown in orange. ABP shown in red. Glycine-serine linkers and polyhistidine tags shown in gray.

Protein	Sequence
IFNα (20.1 kDa)	CDLPQTHNLRNKRALTLLVQMRRLSPLSCLKDRKDFRFPQEKVDAQQIQNAQ AIPVLQELTQQVLNIFTSKDSSAAWDASLLDSFCNDLHQQLNDLKACVMQEVG VQEPPLTQEDYLLAVRTYFHRITVYLREKKHSPCAWEVVRAEVWRAMSSSAK LLARLSEEKEHHHHHH
MSA-IFNα (87.0 kDa)	EAHKSEIAHRYNDLGEQHFKGLVLIAFSQYLQKCSYDEHAKLVQEVTDFAKTC VADESAANCDKSLHTLFGDKLCAIPNLRENYGELADCCTKQEPERNECFLQH KDDNPSLPPFERPEAEAMCTSFKENPTTFMGHYLHEVARRHPYFYAPELLYY AEQYNEILTQCCAEADKESCLTPKLDGVKEKALVSSVRQRMKCSSMQKFGER AFKAWAVARLSQTFPNADFAEITKLATDLTKVNKECCHGDLLECADDRAELAK YMCENQATISSKLQTCCDKPLLKKAHCLSEVEHDTMPADLPAIAADFVEDQEV CKNYAEAKDVFLGTFLYEYSRRHPDYSVSLLLRLAKKYEATLEKCCAEANPPA CYGTVLAEFQPLVEEPKNLVKTNCDLYEKLGEYGFQNAILVRYTQKAPQVSTP TLVEAARNLGRVGTKCCTLPEDQRLPCVEDYLSAILNRVCLLHEKTPVSEHVT KCCSGSLVERRPCFSALTVDETYVPKEFKAETFTFHSDICTLPEKEKQIKKQTA LAELVKHKPKATAEQLKTVMDDFAQFLDTCCKAADKDTCFSTEGPNLVTRCK DALAGGGGSGGGGSGGGGSCDLPQTHNLRNKRALTLLVQMRRLSPLSCLKD RKDFRFPQEKVDAQQIQNAQAIPVLQELTQQVLNIFTSKDSSAAWDASLLDSF CNDLHQQLNDLKACVMQEVGVQEPPLTQEDYLLAVRTYFHRITVYLREKKHS PCAWEVVRAEVWRAMSSSAKLLARLSEEKEHHHHHH
ABP-IFNα (23.9 kDa)	FQSEEQQGGGSGGSEEGGMESEESNGGGSGGSEEGGGSGGGSCDLPQTH NLRNKRALTLLVQMRRLSPLSCLKDRKDFRFPQEKVDAQQIQNAQAIPVLQEL TQQVLNIFTSKDSSAAWDASLLDSFCNDLHQQLNDLKACVMQEVGVQEPPLT QEDYLLAVRTYFHRITVYLREKKHSPCAWEVVRAEVWRAMSSSAKLLARLSE EKEHHHHHH
IFNβ (20.6 kDa)	INYKQLQLQERTNIRKCQELLEQLNGKINLTYRADFKIPMEMTEKMQKSYTAFA IQEMLQNVFLVFRNNFSSTGWNETIVVRLLDELHQQTVFLKTVLEEKQEERLT WEMSSTALHLKSYYWRVQRYLKLMKYNSYAWMVVRAEIFRNFLIIRRLTRNFQ NHHHHHH
ABP-IFNβ (24.3 kDa)	FQSEEQQGGGSGGSEEGGMESEESNGGGSGGSEEGGGSGGGSINYKQLQ LQERTNIRKCQELLEQLNGKINLTYRADFKIPMEMTEKMQKSYTAFAIQEMLQN VFLVFRNNFSSTGWNETIVVRLLDELHQQTVFLKTVLEEKQEERLTWEMSSTA LHLKSYYWRVQRYLKLMKYNSYAWMVVRAEIFRNFLIIRRLTRNFQNHHHHHH

Methods

Mice. C57BL/6 mice (Taconic C57BL/6NTac and JAX C57BL/6J) were purchased. Ifnar1$^{-/-}$ (JAX 032045), Batf3$^{-/-}$ (JAX 013755), and Nlrp3$^{-/-}$ mice (JAX 021302) were purchased and bred in-house. 6-10-week old females were used in experiments. All animal work was conducted under the approval of the Massachusetts Institute of Technology Committee on Animal Care in accordance with federal, state, and local guidelines.

Cells. B16F10 (ATCC), MC38 (a gift from J. Schlom, National Cancer Institute), B16F10 Trp2KO (generated previously (*88*)), and RAW-Lucia ISG (InvivoGen) cells were cultured in Dulbecco's Modified Eagle's Medium (DMEM) (ATCC) supplemented with 10% FBS. RAW-Lucia ISG cells were maintained with 200 μg/mL Zeocin (InvivoGen) every other passage. Adherent cells were cultured at 37 °C and 5% CO_2. HEK293-F cells (Gibco) were cultured in FreeStyle293 Expression Medium (Gibco) shaking at 37 °C and 8% CO_2. All cell lines tested negative for mycoplasma.

Cloning and protein purification. Murine IFNα, IFNβ, MSA-IFNα, ABP-IFNα, ABP-IFNβ, and human IFNα, ABP-IFNα, were cloned with 6-His tags into the gWiz vector (Genlantis) using In-Fusion cloning (Takara Bio) (Table 2-1). Fam20C kinase with a KDEL tag (*38*) and MSA-IL2 with a 6-His tag (*62*) were previously cloned into the gWiz vector. αPD1 was cloned by Sarah Cowles into the gWiz vector starting with the sequence of 29F.1A12, which was a generous gift from the G. Freeman Lab (*89*). This clone is typically used in the rat IgG2a format, but it was cloned with a murine IgG2c isotype with a kappa light chain and the LALA-PG mutations to ablate Fc effector functions and prevent target cell clearance (*90*). Plasmids were amplified in Stellar cells and purified using NucleoBond Xtra endotoxin-free kits (Macherey-Nagel). For transfections, 1 mg plasmid DNA with 2 mL polyethylenimine (Polysciences 23966) in 40 mL OptiPRO Serum Free Medium (Thermo Fisher) was added dropwise to 1 L HEK293-F cells. For ABP-IFNs, the 1 mg plasmid DNA was a mixture of 950 μg ABP-IFN plasmid and 50 μg Fam20C plasmid. After 6 days, proteins were purified from cell supernatants using TALON Metal Affinity Resin (Takara Bio) for IFNs and MSA-IL2, and rProtein A Sepharose Fast Flow Resin (Cytiva) for αPD1. ABP-IFNs and MSA-IL2 were further purified by size exclusion chromatography on an ÄKTA FPLC (GE Healthcare). Typical yields per 1 L HEK293-F cells for murine IFNs were ~10 mg IFNα, ~5 mg IFNβ, ~20 mg MSA-IFNα, ~1 mg ABP-IFNα and ~1 mg ABP-IFNβ. Proteins were buffer exchanged into TBS (IFNs) or PBS (MSA-IL2 and αPD1) using Amicon filters (EMD Millipore). Proteins were sterile filtered and confirmed for minimal endotoxin (< 0.1 EU per dose) using the LAL Chromogenic Endotoxin Quantitation Kit (Pierce). Molecular weight was confirmed by running proteins alongside a Novex Sharp Pre-Stained Protein Standard on a NuPAGE 4-12% Bis-Tris gel (Invitrogen) with MES running buffer and SimplyBlue Safe Stain (Life Technologies). Phosphorylation of ABP-IFNs was confirmed by malachite green assay (Pierce Phosphoprotein Phosphate Estimation Assay Kit). Proteins were flash frozen in liquid nitrogen and stored at -80 °C.

In vitro alum-binding. All alum used in this paper was Alhydrogel (InvivoGen vac-alu-250). To fluorescently label proteins, IFNs were incubated with AF647 NHS ester (Invitrogen A20006) in

PBS with 0.1 M K_2HPO_4, pH 9 for 2 hours at room temperature. Free dye was removed using PD SpinTrap G-25 columns (Cytiva). Fluorescently-labeled IFNs (1 μg) and alum (10 μg) were incubated for 20 min in TBS, pelleted, then re-suspended in PBS 10% mouse serum for 1 hour. Alum was pelleted by centrifugation at 15,000 g to separate the alum-bound fraction from the released fraction, and fluorescence was measured by a Tecan Infinite M200 Pro.

***In vitro* macrophage activation.** RAW-Lucia ISG cells were seeded onto 96-well tissue culture plates at 100,000 cells per well in 200 μL media. Cells were cultured with varying concentrations of IFNs. For some wells, alum and ABP-IFNs were first mixed at a 5:1 (w/w) ratio for 20 min. After 18 hours, luciferase levels in cell supernatants were assayed using QUANTI-Luc (InvivoGen) and a Tecan Infinite M200 Pro with an injector, following vendor instructions.

***In vitro* MC38 proliferation.** MC38 cells were seeded onto 96-well tissue culture plates at 3,000 cells per well in 100 μL media. Cells were cultured with varying concentrations of IFNs for 48 hours. Proliferation was determined using a WST-1 based assay following vendor instructions (Roche). Absorbance at 440 nm was measured on a Tecan Infinite M200 Pro.

IVIS. IFNs were fluorescently labeled as described above. AF647-labeled and unlabeled IFNs were mixed such that each dose contained 0.5 nmol IFN and 0.1 nmol dye in 20 μL TBS. Low dye levels can minimize quenching artifacts. ABP-IFN groups included 60 μg alum in the dose. On day 0, C57BL/6 mice given alfalfa-free feed were inoculated with 1 M B16F10 Trp2KO cells subcutaneously (s.c.) in the right flank. On day 5, tumors were treated (i.t.). Fluorescence at the tumor was imaged by IVIS (Perkin Elmer) using a 640 nm excitation filter and 680 nm emission filter. Image analysis was done by Living Image software. Data were normalized to the maximum signal throughout the experiment for each IFN. On day 7 and 10, serum was collected. On day 10, mice were euthanized and organs were homogenized in tubes containing zirconium beads (Benchmark Scientific) using a mini-beadbeater (BioSpec Products) in PBS with 1 mg/mL collagenase/dispase (Roche) and 25 μg/mL DNase I (Roche). Fluorescence in serum and homogenized organs was measured on a Tecan Infinite M200 Pro. Standard curves were generated using serum and organs from untreated mice with AF647-IFNs added *ex vivo*.

Tumor treatments and survival. On day 0, mice were inoculated with 1 M B16F10, MC38, or B16OVA cells in 50 μL PBS s.c. in the right flank. In some studies, mice were also inoculated on day 0 with 0.15 M ~ 0.25 M B16F10 or B16OVA cells in 50 μL PBS s.c. in the left flank, as indicated in figure legends. Treatments typically began on day 5 when tumors were established (average 24 mm^2 for B16F10 and 30 mm^2 for MC38). Mice were sorted so all groups had equal average tumor area at the start of treatment. IFNs were always treated at 0.5 nmol i.t. (10 μg IFNα; 10 μg IFNβ; 43 μg MSA-IFNα; 12 μg ABP-IFNα; 12 μg ABP-IFNβ) in 20 μL TBS. ABP-IFN doses also contained 60 μg alum and were incubated at room temperature for at least 20 min before treatment. IFNs were dosed on days 5, 11, and 17, except for the BM chimera study and B16OVA study where IFNs were treated on days 6, 12, and 18 instead. For the alum only study, 120 μg alum in 20 μL was treated i.t. on days 5, 7, and 9. MSA-IL2 (30 μg in 50 μL PBS) and αPD1 (200 μg in 100 μL PBS) were treated i.p. at the same time as IFN treatment. Depleting

antibodies aCD8α (Bio X Cell 2.43), aNK1.1 (Bio X Cell PK136), and aLy6G (Bio X Cell 1A8) were dosed at 400 μg i.p. every 4 days from day 3 until day 30. Tumor area (length x width) and body weight were monitored. Most survival data are compiled from multiple experiments. Mice were euthanized when tumors exceeded 100 mm^2, weight loss exceeded 20%, or mice exhibited poor body condition. Mice who died from tumor burden (as defined by the most recent tumor measurement exceeding 70 mm^2) were included in the data. Any other unexpected deaths were omitted from the study. For rechallenge studies, mice were inoculated with 0.1 M B16F10 cells (s.c.) in the left flank at day 100 - 110. Mice were monitored for an additional 100 days and euthanized when their rechallenge tumor exceeded 100 mm^2.

Bone marrow chimeric mice. Host mice ($CD45.2^+$) were irradiated with 500 rad, allowed to recover for 3 hours, and irradiated again with 550 rad. The next day, femurs and tibias were excised from congenically marked donor mice ($CD45.1^+$), and the ends of the bones were cut. Cut bones were placed in a pierced 500 μL tube nested inside of a 1.5 mL tube. Bone marrow (BM) was harvested by centrifugation at 2500 g for 3 min. BM was resuspended in cold RPMI, 70-μm filtered, and centrifuged at 500 g for 3 min. BM was washed in cold PBS twice, then resuspended in cold PBS. 7.5 M BM cells in PBS were injected retro-orbitally into irradiated host mice within 24 hours post-irradiation. Engraftments were confirmed after 6 weeks.

Tumor lysates. Tumors were excised, weighed, and ground with a pestle in 1:20 (w/v) of tumor in Tissue Protein Extraction Reagent (Thermo Fisher) supplemented with Halt Protease Inhibitor Cocktail (Thermo Fisher) and 5 mM EDTA. Samples were incubated for 30 min at 4 °C, debris was pelleted by centrifugation at 10,000 g, and supernatants were filtered through Corning Costar Spin-X tubes. The LEGENDplex mouse anti-virus response panel (13-plex) (BioLegend) was used following vendor instructions and analyzed with BD FACS LSR Fortessa.

Flow cytometry. Blood was collected by cheek bleed into K2EDTA tubes (MiniCollect). Tumors, tdLNs, and spleens were excised, weighed, mechanically dissociated, and 70-μm filtered into single-cell suspensions. Spleens and blood were resuspended in ACK Lysing Buffer (Gibco). Cells were blocked with CD16/CD32 antibody (eBioscience Clone 93) before antibody-labeling. For intracellular markers, cells were fixed and stained in Permeabilization Buffer (Invitrogen). To assess tumors, cells were stained with Zombie NIR viability dye (BioLegend 423105), Apotracker Green (BioLegend 427402), BUV395-CD45 (BD Biosciences 30-F11), AF647-TA99 (labeled in-house), PE/Cy7-MHC-I (BioLegend 28-8-6), PE-PD-L1 (BioLegend 10F.9G2), and BV605-Ki67 (BioLegend 16A8). To assess T cells from tumors, cells were stained with Zombie UV viability dye (BioLegend 423107), BUV395-CD45 (BD Biosciences 30-F11), BV785-CD3 (BioLegend 17A2), BUV737-CD8α (BD Biosciences 53-6.7), BV605-Ki67 (BioLegend 16A8), BV711-TIM3 (BioLegend RMT3-23), and AF488-TCF1/TCF7 (Cell Signaling Technology C63D9). tdLNs were stained with Zombie NIR viability dye (BioLegend 423105), BUV395-CD45 (BD Biosciences 30-F11), PE/Cy7-Ly6C (BioLegend HK1.4), AF647-MHCII (BioLegend M5/114.15.2), BV605-CD24 (BioLegend M1/69), and PE-CD86 (BioLegend GL-1). Spleens were stained with Zombie Aqua viability dye (BioLegend 423101), BUV395-CD45 (BD Biosciences 30-F11), PE/Cy7-CD3 (BioLegend 17A2), and BUV737-CD8α (BD Biosciences 53-6.7). Spleens were also stained with BV605-CD44 (BioLegend IM7), PE-CD127 (BioLegend

A7R34), and APC-KLRG1 (BioLegend 2F1) in one panel, and AF647-CD25 (BioLegend PC61), BV605-Ki67 (BioLegend 16A8), PE-TIM3 (BioLegend RMT3-23), and AF488-TCF1/TCF7 (Cell Signaling Technology C63D9) in a separate panel. To confirm BM engraftment from blood, cells were stained with Zombie Aqua viability dye (BioLegend 423101), APC-CD45.1 (BioLegend A20), and PE-CD45.2 (BioLegend 104). To confirm antibody-mediated depletions from blood, cells were stained with Zombie Aqua viability dye (BioLegend 423101), BUV395-CD45 (BD Biosciences 30-F11), BV785-CD3 (BioLegend 17A2), BUV737-CD8α (BD Biosciences 53-6.7), BV711-Ly6G (BioLegend 1A8), APC/Cy7-Ly6C (BioLegend HK1.4), BV421-CD11b (BioLegend M1/70) and PE/Cy7-NKp46 (BioLegend 29A1.4). BD FACS LSR Fortessa or BD FACS Symphony A3 analyzers were used, and data were analyzed with FlowJo V10.

Statistical analysis. Statistics were performed with GraphPad Prism software V7. Survival was compared by log-rank Mantel-Cox text. As described in figure captions, other metrics were compared by one-way or two-way analysis of variance (ANOVA) with Tukey's multiple comparisons test, or unpaired t-test. The *n* and *P* values are indicated in captions.

Acknowledgments

Chapter 2 was performed under the guidance of Prof. K. Dane Wittrup. Thank you also to Prof. Stefani Spranger, Prof. Darrell Irvine, and Prof. Philip Kranzusch for their advice. I am thankful to the entire Wittrup lab for their support and helpful discussion around this project. In particular, thank you to Yash Agarwal, Noor Momin, Sarah Cowles, Joseph Palmeri, Ellen Duong, Vladlena Hornet, Allison Sheen, Brianna Lax, and Adrienne Rothschilds for their advice and help performing experiments. Yash Agarwal developed the ABP platform for cytokines, and his friendly support during all aspects of this project are very appreciated. Noor Momin's mentorship and her insights on intratumorally-administered cytokines was also critical. Thank you to Ellen Duong for enabling the bone marrow chimera study and helpful feedback on the manuscript. Human IFNs were produced by Vladlena Hornet and MSA-IL2 was produced by Adrienne Rothschilds.

We thank the Koch Institute's Robert A. Swanson (1969) Biotechnology Center (National Cancer Institute Grant P30-CA14051) for technical support, specifically the Flow Cytometry Core Facility and Preclinical Imaging and Testing. Thank you also to the MIT Division of Comparative Medicine.

Funding:

This work was supported by the National Cancer Institute Grant 5R01CA174795-03 (to Prof. Wittrup), the National Institute of Biomedical Imaging and Bioengineering Grant 1R01EB031082-01A1 (to Prof. Irvine and Prof. Wittrup), and the Koch Institute Frontier Research Program via the Casey and Family Foundation Cancer Research Fund (to Prof. Spranger and Prof. Wittrup).

Personnel were supported by the NSF Graduate Research Fellowship Program (EAL, NM, SCC, JRP, AS, BML, AMR), NIH/NIGMS Biotechnology Training Program (EAL, NM, AMR), Siebel Scholar Award (EAL, NM), and a fellowship from the Ludwig Center at the Koch Institute (YA). Personnel were also supported by the Hope Babette Tang Student Research Fund, the Kristin R. Pressman and Jessica J. Pourian Koch Institute Fund, and the Charles S. Krakauer Fund (EAL).

Competing Interests:

Yash Agarwal, Darrell Irvine, and Dane Wittrup are named as inventors in a patent application filed by MIT related to alum-anchored cytokines. Darrell Irvine and Dane Wittrup are co-founders of Ankyra Therapeutics, which has licensed rights to this intellectual property.

Chapter 3. Intratumoral nanobody-IL-2 fusions that bind the tumor extracellular matrix suppress solid tumor growth

This chapter was performed in equal collaboration between Emi Lutz, Noor Jailkhani, and Noor Momin, under the guidance from Prof. Richard O. Hynes and Prof. K. Dane Wittrup.

This chapter, with some modifications, was submitted for publication.

Abstract

Confining cytokine exposure to the tumor would greatly enhance cancer immunotherapy safety and efficacy. Immunocytokines, cytokines fused to tumor-targeting antibodies, have been developed with this intention, but without significant clinical success to date. A critical limitation is uptake by receptor-expressing cells in the blood, that decreases the dose at the tumor and engenders toxicity. Small-format immunocytokines, constructed with antibody fragments, are hypothesized to improve tumor specificity due to rapid systemic clearance. However, effective design criteria for small-format immunocytokines need further examination. Here we engineer small interleukin-2 (IL-2) immunocytokines fused to nanobodies with nanomolar to picomolar affinities for the tumor-specific EIIIB domain of fibronectin. Upon intravenous delivery into immunocompetent mice, such immunocytokines led to similar tumor growth delay as size-matched untargeted IL-2. Intratumoral delivery imparted improved survival dependent on affinity to EIIIB. Intratumoral administration offers a promising avenue to deliver small-format immunocytokines, provided effective affinity to the tumor microenvironment.

Introduction

Cytokines can potently activate anti-tumor immune cells, and so are promising cancer immunotherapies. In the 1990s, interleukin-2 (IL-2, marketed as Proleukin / aldesleukin) earned FDA-approval after achieving complete responses in a small subset of patients with metastatic renal cell carcinoma and metastatic melanoma (*8*, *9*). Unfortunately, the majority of treated patients also experienced severe, and in some cases fatal, adverse reactions to treatment (*91*). Toxicity from IL-2 treatment arises from on-target, off-tumor activation of systemically circulating immune cells. Strategies to improve IL-2 therapy hinge on preferentially increasing tumor exposure while decreasing systemic exposure.

Intravenous administration of cytokines fused to tumor-targeting vehicles aims to direct their immunomodulatory effects to the tumor. Immunocytokines, with cytokines fused to antibodies or antibody fragments specific to tumor-associated antigens, have been tested to this end with some promise. However, recent clinical trials show that dose-limiting side effects and low efficacy are not fully ameliorated by such an attempt at tumor targeting (*92*). Previously, the Wittrup lab demonstrated in mice that large antibody-IL-2 fusions have compromised tumor-targeting due to their prolonged circulation and uptake by abundant IL-2-receptor-expressing cells in the blood (*18*). Tzeng et al. (*18*) predicted that smaller immunocytokines may, for some

combinations of parameters, achieve higher tumor to blood ratios, because of their rapid systemic clearance.

Here we explore small-format IL-2 immunocytokines with affinity to the tumor extracellular matrix, a major component of the tumor microenvironment, rather than cell-surface antigens of tumor cells. Specifically, the alternatively spliced EIIIB (EDB) domain of fibronectin (FN), which is not expressed in healthy adult tissue, is widely expressed in a variety of cancers as a component of the tumor extracellular matrix (*93*). EIIIB is a promising translational target, with an identical amino acid sequence in humans and mice. EIIIB+FN has been pursued by others in the context of IL-2 (*94*), as well as other cytokines and anti-tumor therapies (*95*). As one example, Jailkhani et al. generated the nanobody NJB2, which binds EIIIB with 2 nM affinity and has been applied in tumor imaging (*96*) and chimeric antigen receptor (CAR) T cell therapy (*97*). Here, we use yeast surface display to affinity mature NJB2 and engineer new nanobodies that bind EIIIB with picomolar affinity, and demonstrate the necessity for such high affinity for efficacy following intratumoral administration.

In this chapter, we develop and test small (32 kDa) nanobody-IL-2 immunocytokines with a range of affinities to EIIIB in immunocompetent, tumor-bearing mice. When delivered intravenously, even picomolar affinity to EIIIB did not produce substantially improved efficacy or altered binding to immune cell types compared to size-matched, untargeted IL-2. However, after local intratumoral administration, anti-EIIIB IL-2 fusions enabled a high B16F10 melanoma cure rate that was not observed with untargeted IL-2. In the optimal implementation, nanobody-IL-2 fusions ablated established solid tumors and primed protective adaptive immunity.

Results

Engineering affinity-matured anti-EIIIB nanobodies via yeast surface display

The affinity between a drug and its target is expected to play a significant role in therapeutic outcome. We therefore aimed to generate and test nanobody-IL-2 immunocytokines with a range of affinities for EIIIB. To this end, we affinity-matured the parental NJB2 nanobody, which has 2 nM affinity for EIIIB (*96*), using yeast surface display (*98*) (**Fig. 3-1A**). We first generated a yeast library displaying NJB2 mutants (**Fig. 3-1B**). By titrating the library against EIIIB, we chose a productive concentration of EIIIB to use for equilibrium sorting (**Fig. 3-1C**). The library underwent three rounds of equilibrium sorting, with example gating strategies shown (**Fig. 3-2**). A pool of three of the most promising clones served as template for a second-round yeast library mutagenesis that we stringently screened for further enhancements in affinity, using both equilibrium and kinetic sorting strategies. From these sorts, we identified ten nanobodies of interest with frequently observed mutations in both their complementarity-determining regions (CDR) and framework regions (**Fig. 3-3A, Table 3-1**).

The ten nanobodies were recombinantly expressed, and all ten demonstrated sub-nanomolar affinity for EIIIB as measured by BioLayer Interferometry (BLI). We proceeded with clones LMJ1.2C and LMJ2.5I, which respectively contain two and five mutations compare to

NJB2, as visualized with a homology model of NJB2 generated using AbodyBuilder on the SAbPred server (**Fig. 3-3B**) (*99–101*). As measured by BLI, LMJ1.2C demonstrated a 300 pM K_D and LMJ2.5I demonstrated an approximately 25 pM K_D (**Fig. 3-3C**). Picomolar K_D values can be difficult to measure by standard methods like BLI (the off-rate is unclear) or ELISA (depleting conditions at low concentrations). Although the new nanobodies clearly have sub-nanomolar affinities, additional methods like kinetic exclusion assays would be useful to determine exact K_D values. Next, the nanobodies were tested for their specificity for EIIIB-FN by immunoblotting. The nanobodies all showed specificity of binding to fragments that contained EIIIB (EIIIB-His and FN (7-15) EIIIB), while no binding was observed for negative controls including human and mouse plasma fibronectins, ECM enriched from normal murine lung or His-GFP protein (**Fig. 3-3D**).

Developing anti-EIIIB nanobody-IL2 fusions

After generating nanobodies with a range of affinities for EIIIB, we next developed anti-EIIIB nanobody-IL-2 fusions (**Table 3-2**). We expressed murine IL-2 fused to NJB2, LMJ1.2C, and LMJ2.5I (**Fig. 3-4 A and B**). As a size-matched control, we also constructed a fusion of IL-2 with the NJT6 nanobody, which has no murine target (*96*). As an inactive control, we fused NJB2 to murine IL-2 bearing point mutations described to abrogate cytokine activity (NJB2-IL2-mt) (**Fig. 3-4C**) (*102*, *103*). All recombinant immunocytokines were ~32 kDa (ranging from 31.8 to 32.2 kDa). The IL-2 fusions had identical bioactivity on CTLL-2 cells, a murine T cell line response to IL-2, while the IL2-mt fusion did not induce CTLL-2 proliferation (**Fig. 3-5A**). When expressed as a cytokine fusion, the nanobodies maintained their expected affinities to EIIIB, as measured by BLI (**Fig. 3-5B**).

Intravenous anti-EIIIB nanobody-IL2 fusions lead to modest tumor growth delay

To investigate the therapeutic efficacy of the nanobody-IL-2 fusions, we employed the B16F10 melanoma model, previously shown to express EIIIB+FN (*96*). Since the B16F10 model is immunologically cold and unresponsive to most single-agent immunotherapies, we combined our immunocytokine treatment with TA99, a tumor-targeting antibody against tumor-associated antigen tyrosinase-related protein-1. TA99 has been shown to activate natural killer (NK) cells and prime $CD8^+$ T cells that depend on IL-2 for anti-tumor activity (*62*). Mice bearing subcutaneous B16F10 tumors were treated with the nanobody-IL-2 fusions intravenously (i.v.), and with TA99 intraperitoneally (i.p.).

We first tested the benefit of nanomolar affinity to EIIIB for 2 weeks of treatment (**Fig. 3-6A**). Compared to the inactive control NJB2-IL2-mt, both NJT6-IL2 and NJB2-IL2 improved survival of treated mice (P = 0.003). However, despite its 2 nM affinity for EIIIB, NJB2-IL2 did not improve survival compared to the untargeted size-matched control, NJT6-IL2 (P = 0.40). We next tested IL2-fusions for 3 weeks of treatment instead of 2 weeks, and incorporated immunocytokines with picomolar affinity for EIIIB (**Fig. 3-6B**). As before, we observed that the presence of untargeted NJT6-IL2 improved survival compared to mice who did not receive IL-2 (P =0.006). Compared to the size-matched untargeted NJT6-IL2 control, NJB2-IL2 with nanomolar affinity to EIIIB led to non-significant trends towards survival extension (P = 0.10),

while LMJ1.2C-IL2 and LMJ2.5I-IL2 with picomolar affinity to EIIIB led to modest extension of survival (P = 0.02 for both). However, the median survival was only extended by 2 days, and all mice succumbed to tumor burden.

IL-2 immunocytokines have similar cellular distribution after intravenous dosing

Intravenously-delivered IL-2 with picomolar affinity to EIIIB had only a modest impact on tumor growth compared to untargeted IL-2 (**Fig. 3-6**). The Wittrup lab has previously showed that the biodistribution of large format IL-2 immunocytokines is dominated by the IL-2 moiety (*18*). To test how the nanobody and cytokine moieties impact cellular biodistribution of small-format nanobody-IL-2 fusions, we assessed drug uptake in different immune cells across multiple organs. We compared active IL-2 fused to NJT6, NJB2, or LMJ2.5I, as well as NJB2 fused to inactive mutant IL-2. The nanobody-IL-2 fusions were fluorescently labeled with Alexa Fluor 647 (AF647) and administered i.v. into mice bearing 8-day-old B16F10 tumors. 24 hours later, we harvested tumors, tumor draining lymph nodes (tdLNs), spleens, and blood, and profiled the biodistribution of immunocytokines in immune cells using flow cytometry (**Fig. 3-7**).

Consistent with the small size of the immunocytokines, all constructs had rapid systemic clearance, and less than 0.3% of the injected dose remained in the blood 24 hours after retro-orbital injection (**Fig. 3-8A**). The percentage of each cell population positive for AF647 is shown as a heatmap (**Fig. 3-8B**), with all data and statistics shown for tumor (**Fig. 3-9**), tdLN (**Fig. 3-10A**), spleen (**Fig. 3-10B**), and blood (**Fig. 3-10C**). There was minimal signal in mice treated with PBS or inactive IL-2, as expected, while the three proteins with active IL-2 had generally similar levels of drug uptake in different immune cell populations across the tested organs. Unlike what has been observed for the large format immunocytokines (*18*), these small-format nanobody-IL-2 fusions had minimal signal in spleen and blood, consistent with their rapid clearance from systemic circulation. The Wittrup lab has previously seen that $CD8^+$ T cells and NK cells in the tumor are especially important in the uptake and efficacy of larger IL-2 constructs in combination with TA99 (*18*, *32*, *62*). Regardless of affinity to EIIIB, the three active IL-2 fusions had similar impacts on these populations, namely increased percent $AF647^+$ for $CD8^+$ T cells in the tumor (**Fig. 3-9A**), increased median AF647 for NK/NKT cells in the tumor (**Fig. 3-9B**), and no significant differences in cell counts (**Fig. 3-9C**). These data on similar systemic distribution of the nanobody fusions with active IL-2, regardless of affinity to EIIIB, are consistent with similar survival efficacy from these constructs after intravenous delivery.

Intratumoral dosing of anti-EIIIB IL-2 fusions enables nanobody-driven cures

The intravenous administration of EIIIB-specific nanobody-IL-2 fusions resulted in only a mild nanobody-driven impact on survival and cellular biodistribution (**Figs. 3-6 to 3-10**). We next tested if avoiding systemic circulation altogether by switching from intravenous to intratumoral (i.t.) administration could improve the impact of ECM affinity on IL-2 efficacy in the B16F10 model. Since i.t. administration inherently increases drug exposure at the tumor, we reduced the IL-2 dose from 1 nmol to 0.4 nmol, and the frequency of IL-2 dosing from thrice weekly to twice weekly (**Fig. 3-11A**).

Even with a reduced IL-2 dose and frequency, intratumoral administration of nanobody-IL-2 fusions to B16F10 tumors markedly reduced tumor growth and led to a more pronounced benefit from introducing affinity to EIIIB (**Fig. 3-11A**). Compared to untargeted NJT6-IL2 (1/11 cures), we observed improved survival with nanomolar NJB2-IL2 (6/11 cures, $P = 0.01$) and picomolar LMJ2.5I-IL2 (8/11 cures, $P = 0.004$). Although LMJ2.5I-IL2 led to the highest cure rate, there was no statistical difference in survival between NJB2-IL2 and LMJ2.5I-IL2 ($P = 0.49$), indicating that picomolar and nanomolar targeting behave similarly in this setting. When cured mice (surviving at 94 days) were rechallenged with 0.1 M B16F10 cells in the opposite flank, a majority of mice rejected rechallenge, indicating immunological memory from the combination of nanobody-IL-2 fusions and TA99 (**Fig. 3-11B**). Further reducing the i.t. dose and frequency to 0.2 nmol once weekly failed to cure any tumors, indicating a dose-dependent response, but did lead to some extension of survival for the highest affinity immunocytokine (**Fig. 3-11C**). These data show that intratumoral injection of small ECM-binding immunocytokines was more effective than systemic delivery.

Discussion

Development of optimal criteria to design and dose cytokine constructs for cancer immunotherapy is an active area of study (*19*, *25–27*, *32*, *104*). Proteins of the ECM, such as EIIIB+FN as described here, are promising targets because of their stability and their selective, abundant expression in disease sites. Although nanobody-cytokine fusions targeting cancer cell surface antigens have been studied previously in mice (*105*), here we develop and test ECM specific nanobody-cytokine fusions and characterize effective design parameters for such small-format immunocytokines. We engineered nanobody-IL-2 immunocytokines targeting the tumor ECM that are small in molecular size (~32 kDa), possess a range of binding affinities to tumor-associated, EIIIB-containing fibronectin (untargeted, nanomolar, and picomolar) and administered them via different routes (i.v. and i.t.) into immunocompetent mice.

The systemic delivery of IL-2 with picomolar affinity to EIIIB via i.v injections resulted in a modest but statistically significant extension of survival compared to untargeted IL-2 in the immunocompetent solid melanoma model B16F10 in combination with TA99. However, median survival was extended by only 2 days compared to untargeted IL-2, and all mice succumbed to tumor burden. In contrast, the intratumoral administration of IL-2 immunocytokines with nanomolar or picomolar affinity to EIIIB resulted in strong extension of survival in mice bearing established B16F10 tumors (55% and 73% cures, respectively). High cure rate was not seen with intratumoral NJT6-IL2, or with intravenous delivery of any of the nanobody-IL2 fusions, suggesting that both affinity to the tumor ECM and intratumoral administration can together maximize anti-tumor benefit from small-format IL-2 immunocytokines.

The Wittrup lab has shown previously that when using large IgG format immunocytokines based on TA99-IL-2 fusions (183 kDa), the IL-2 moiety and not the antibody specificity govern biodistribution and therapeutic efficacy (*18*). Since IL-2 engages with receptors on immune cells that are highly abundant in blood and lymphoid tissues, immunocytokine pharmacokinetics are dominated by the cytokine moiety after i.v. dosing.

Indeed, the majority of large-format IL-2 immunocytokine is bound to IL-2-receptor-expressing cells in the systemic sink. PK modeling predicted that smaller immunocytokines might exhibit comparatively improved tumor-specificity and efficacy, due to their more rapid clearance and faster diffusion into the tumor microenvironment. In this work we observed rapid clearance of the smaller (~32 kDa) anti-EIIIB immunocytokines from circulation, and did not observe elevated binding to immune cells in the blood. However, only a small percentage of immune cells in the tumor bound the small immunocytokines. Furthermore, IL-2 fusions with or without affinity to EIIIB had similar cellular biodistributions on immune cells. For small immunocytokines of the type studied here, sequestration by binding to IL-2 receptor on immune cells appears insufficient to explain their minimal efficacy, indicating that additional parameters still need to be considered in the context of systemic delivery. Previous tumor targeting theories have predicted that smaller agents with picomolar affinity could accumulate favorably within tumors (*106*). Further study of IL-2 immunocytokines of different sizes may reveal an optimum circulation time that allows sufficient tumor enrichment while maintaining minimal binding to the systemic sink. This optimum may or may not be feasibly approachable, depending on the systemic toxicity incurred by dosing such agents at high level systemically.

Although in this work we only observed minor nanobody-driven benefits for small IL-2 immunocytokines delivered intravenously, there may be other situations where tumor-targeting could lead to larger improvements for systemically-delivered cytokines. Others have reported efficacy and biodistribution improvements after i.v. dosing of anti-EIIIB IL-2 immunocytokines (*94*, *107*, *108*), or nanobody-IL-2 fusions targeting other antigens like PD-L1 (*105*). B16F10 expresses lower levels of EIIIB+FN compared to some other tumor models. Higher target expression may increase the degree of benefit conferred by tumor-targeting. The choice of cytokine may also impact these results, especially depending on cytokine affinity to its receptor and abundance of cytokine receptors in systemic circulation. Indeed, strategies aimed to minimize systemic cytokine-mediated drug uptake include weakening the potency of the fused cytokine and converting the cytokine into a prodrug (*109*, *110*). Several immunocytokines in clinical trials employ the former strategy by fusing a mutated IL-2 with reduced IL-2Rα binding to an antibody directed against tumor-associated antigens (*111–114*). Despite a weakened IL-2, systemic cytokine uptake appears still to be present, as indicated by high toxicity (*111*) and high uptake in non-pathological lymphoid tissues and spleens (*112*). Enabling effective systemic administration of immunocytokines is challenging as minimizing engagement in the periphery can often conflict with maximizing efficacy at the tumor. Further studies are needed with additional cytokines, antigens, and tumor models to clarify the degree of survival benefit conferred by attempted tumor-targeting of systemically administered immunocytokines. Testing immunocytokines in immunocompetent mice with fully size-matched untargeted controls will both be important aspects of studies intended to elucidate therapeutic index effects and systemic sink competition.

As an improved alternative to intravenous treatment, we dosed the nanobody-IL-2 fusions intratumorally. The i.t. setting enabled a high B16F10 cure rate and revealed larger differences between IL-2 with and without affinity to EIIIB. The Wittrup lab and others (*32*, *36*, *38*) find that beyond improving treatment efficacy, intratumoral administration enables

immunocytokine dose sparing and has been reported to reduce the formation of anti-drug antibodies (*115*). Clinically, intratumoral administration of wild-type IL-2 - not as an immunocytokine - yielded impressive improvement in therapeutic efficacy and toxicity of melanoma lesions (*116*). Our current results demonstrate that immunocytokines are capable of unleashing anti-tumor effects superior to untargeted IL-2 when intratumorally injected. Benefits of intratumoral administration have also been observed previously for immunocytokines that bind tumor cellular targets (*115*).

Among the most studied ECM-specific IL-2-based immunocytokines is L19-IL2, consisting of a homodimerizing single-chain variable fragment directed against EIIIB-containing fibronectin fused to wild-type IL-2. The administration of L19-IL2 and some other IL-2 immunocytokines (*35*, *117*) in clinical trials has also shifted towards the intratumoral route, likely to benefit from the improved efficacy that intratumoral administration enables. Intratumoral administration is feasible for many histological conditions and target organs in the clinic (*28*), and effective design criteria for intratumoral therapy are being increasingly understood (*31*).

One theoretical advantage of systemic over intratumoral delivery is the potential to deliver immunocytokines to distant metastases, since even small metastases also exhibit tumor-specific ECM changes such as EIIIB+FN (*96*). We have not tested that possibility in the experiments described here but prior studies have suggested that intratumoral delivery can elicit abscopal effects on distant sites (*32*, *38*) via priming of NK or T cell responses. Further research into both intratumoral and systemic routes of delivery will be necessary to explore strategies to elicit both local effects at the primary site and efficacy against distant metastases.

ECM-targeting has many applications beyond cytokine therapy. The parent nanobody NJB2 has been shown to be a powerful tool for noninvasive *in vivo* imaging in several tumor models (*96*) and NJB2-based CAR T-cells were effective against B16F10 solid tumors (*97*). With an improved picomolar K_D, the novel higher affinity nanobodies such as LMJ2.5I may enable tumor imaging over longer time-periods with high signal-to-noise resolution (*118*), or improved CAR T-cell efficacy. NJB2 and the higher affinity nanobodies such as LMJ2.5I can also be applied to the targeted delivery of small molecule drugs and radiopharmaceuticals where rapid systemic clearance enabled by small size and long on-target retention enabled by a slow off-rate are favorable (*119*). Future studies are needed to test these nanobodies in these contexts.

In this work, we generated ECM specific immunocytokines based on IL-2 and EIIIB-specific nanobodies. For these small IL-2 immunocytokines, affinity to EIIIB provided only small advantage when intravenously injected. In contrast, we show that intratumoral delivery resulted in a durable anti-tumor immune response and resistance to subsequent tumor challenge in a nanobody-dependent manner. Future studies to extrapolate this finding to small immunocytokines directed against different tumor-associated targets and fused to other cytokines are still required. Nonetheless, we identify that intratumoral administration can overcome the pharmacokinetic challenges of i.v. injected immunocytokines and drive major enhancements in survival.

Figures

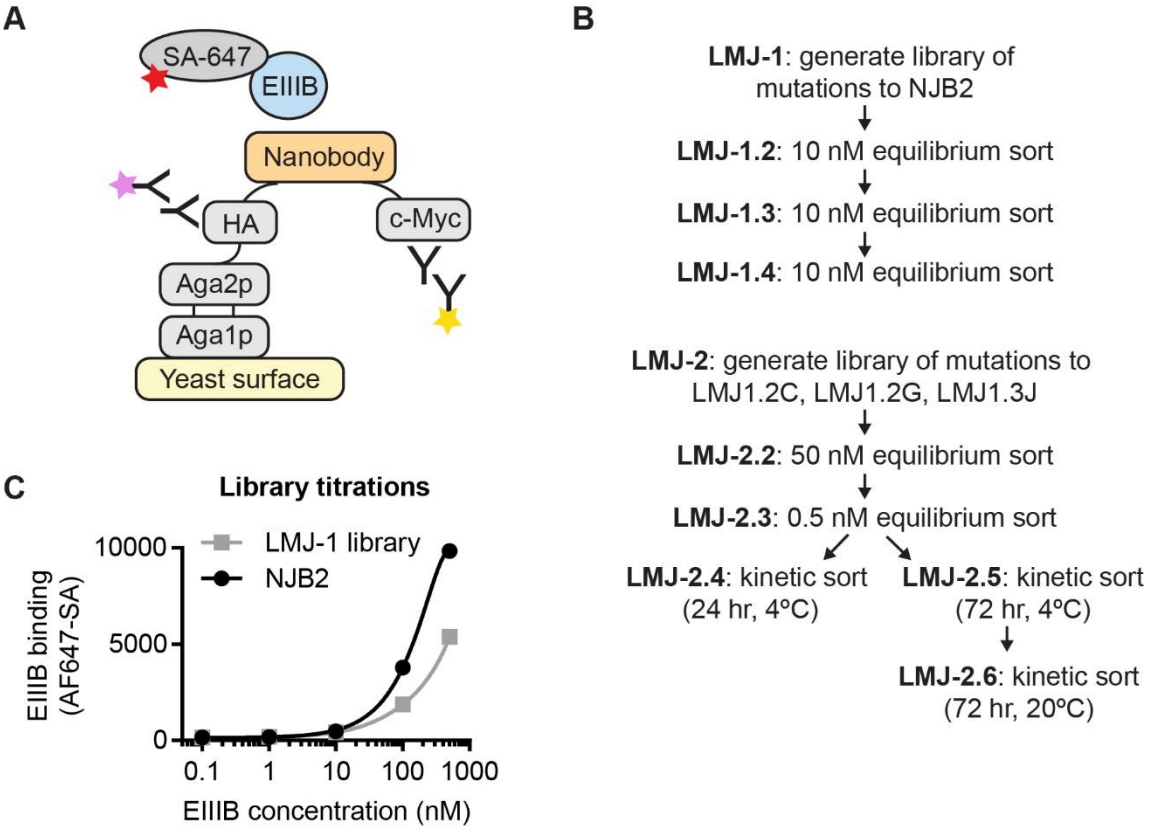

Figure 3-1: Selection strategy for yeast surface display.
(**A**), Schematic showing how nanobody libraries were expressed on the surface of yeast as an Aga2 fusion. Nanobody expression is detected by antibodies that bind to epitope tags hemagglutinin (HA) or c-Myc. Yeast were selected for binding to biotinylated EIIIB, as detected by Streptavidin Alexa Fluor 647 (SA-647). (**B**), Pipeline for yeast surface display is outlined. (**C**), Binding to EIIIB was measured for yeast displaying NJB2, or the LMJ-1 yeast library. Based on these titrations, we initially used an equilibrium sorting condition of 10 nM EIIIB.

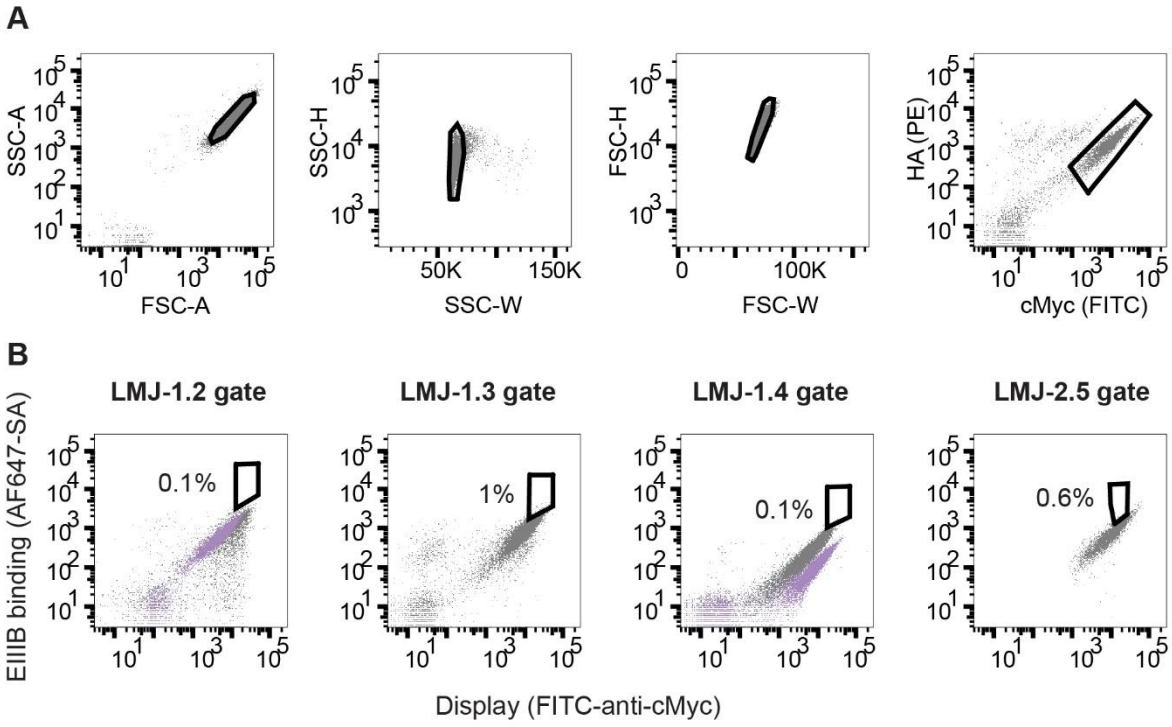

Figure 3-2: Gating strategy for yeast surface display.
(**A**), During sorts, yeast were first gated for single cells as shown. During some sorts, an additional step to gate cells with equal display of HA and cMyc was used to prevent selective pressure for mutations in cMyc. (**B**), Representative sorting gates (black) are shown for yeast display libraries (gray). The clone NJB2 (purple) was included in a separate tube during most sorts to serve as a benchmark, and is shown here for gates LMJ1.2 and LMJ1.4. The top ~0.1–1% of the library was collected during each sort.

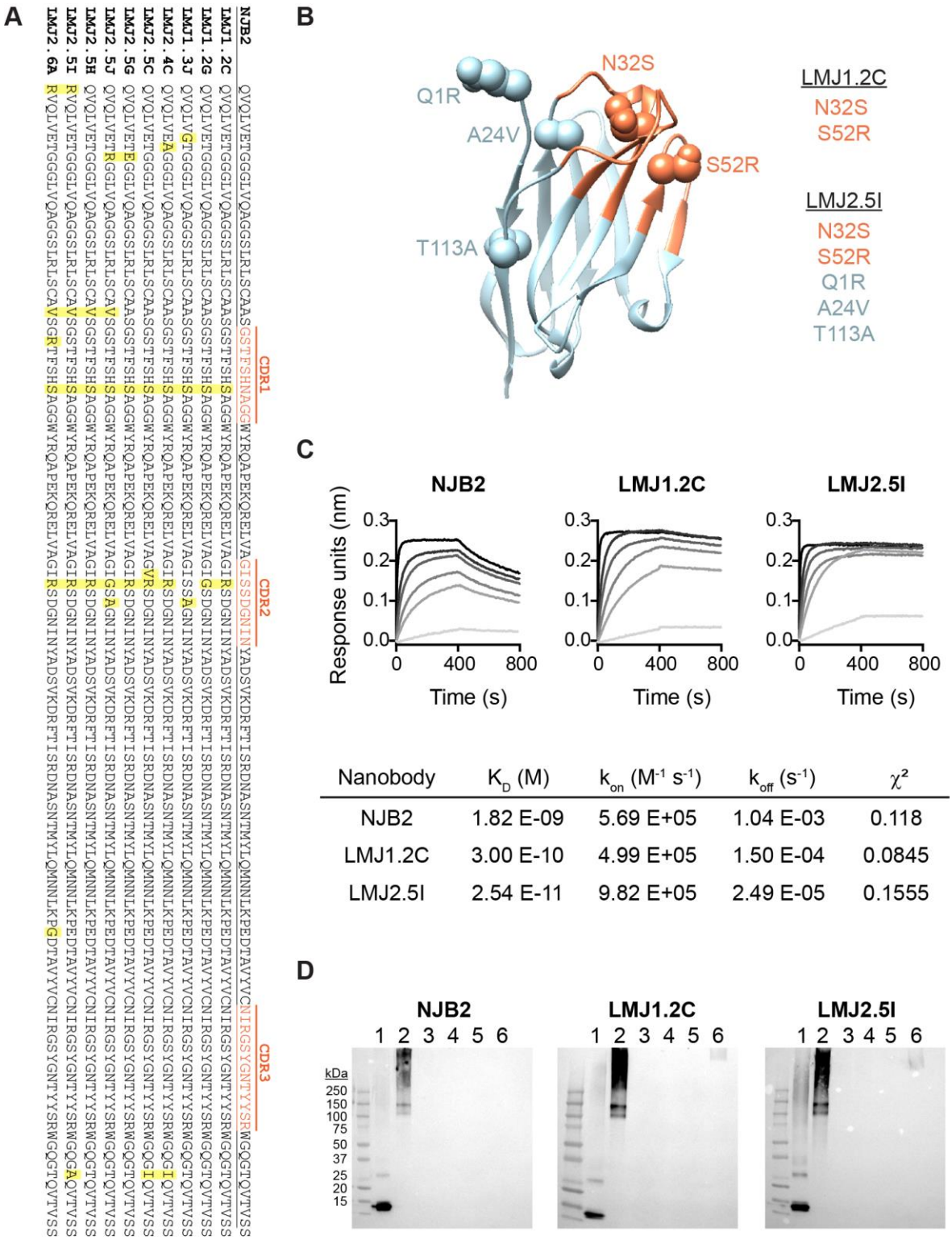
A
B
C
D
CDR1
CDR2
CDR3
N32S
Q1R
A24V
S52R
T113A
LMJ1.2C
N32S
S52R
LMJ2.5I
N32S
S52R
Q1R
A24V
T113A
NJB2
LMJ1.2C
LMJ2.5I
Response units (nm)
Time (s)
Nanobody | K_D (M) | k_on (M^-1 s^-1) | k_off (s^-1) | χ²
NJB2 | 1.82 E-09 | 5.69 E+05 | 1.04 E-03 | 0.118
LMJ1.2C | 3.00 E-10 | 4.99 E+05 | 1.50 E-04 | 0.0845
LMJ2.5I | 2.54 E-11 | 9.82 E+05 | 2.49 E-05 | 0.1555
NJB2
LMJ1.2C
LMJ2.5I
1 2 3 4 5 6
kDa
250
150
100
75
50
37
25
20
15

Figure 3-3: Nanobodies generated by yeast surface display.
(**A**), Sequences are shown for nanobody clones that were generated by yeast surface display and chosen for recombinant expression. Nanobodies were chosen if they contained mutations that were observed in many clones after yeast display sorts. Highlighted residues indicate mutations compared to the parental NJB2 nanobody. (**B**), A homology model of NJB2 was generated using ABodyBuilder on the SAbPred server. CDRs (orange) and framework (blue) are shown in ribbon format. The location of mutations in LMJ1.2C and LMJ2.5I are shown in sphere format. (**C**), Biotin-tagged nanobodies were analyzed by bio-layer interferometry (BLI). Equilibrium dissociation constant (K_D), rate of association (k_{on}), and rate of dissociation (k_{off}) using 1:1 curve fits are reported. Dark to light indicates analyte concentrations of 350, 70, 35, 14, 7, and 0.7 nM. (**D**), Biotin-tagged nanobodies were analyzed by immunoblot. Lanes 1-6, (1) EIIIB-His_6, (2) FN 7-15 EIIIB (3) human plasma FN (4) mouse plasma FN (5) normal murine lung ECM (6) His-GFP protein.

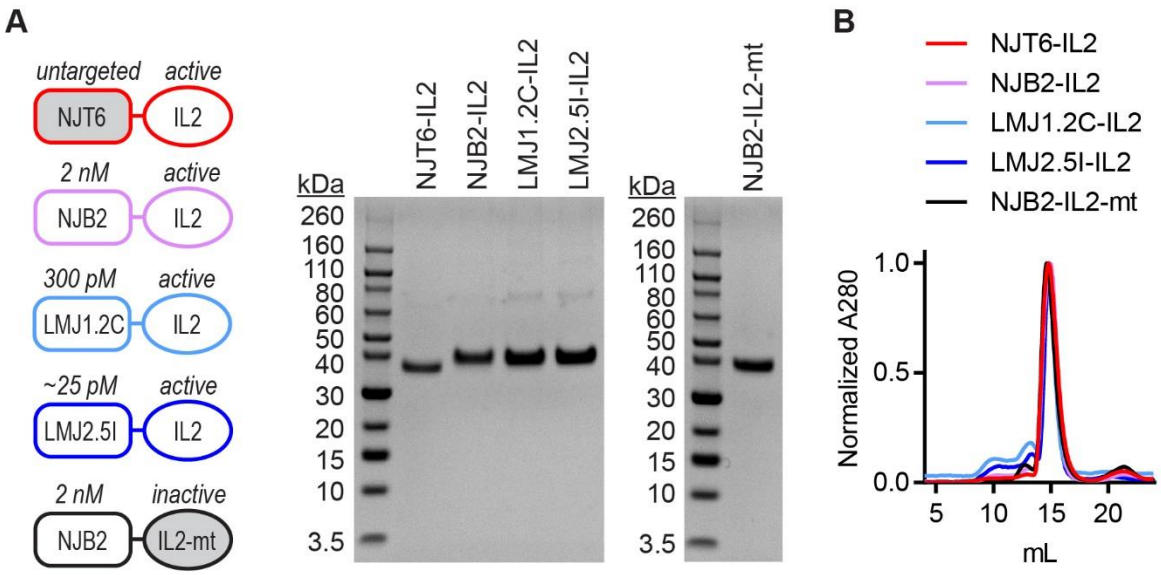

C

```
IL2-h-wt   APTSSS--------------TKKTQLQLEHLLLDLQMILNGINNYKNPKLTRMLTFKFYM  46
IL2-m-wt   APTSSSTSSSTAEAQQQQQQQQQQQQHLEQLLMDLQELLSRMENYRNLKLPRMLTFKFYL  60
IL2-m-mt   APTSSSTSSSTAEAQQQQQQQQQQQQHLEQLLMDLQELLSRMENYRNLKLPDMLTFEFYL  60

IL2-h-wt   PKKATELKHLQCLEEELKPLEEVLNLAQSKNFHLRP-RDLISNINVIVLELKGSETTFMC 105
IL2-m-wt   PKQATELKDLQCLEDELGPLRHVLDLTQSKSFQLEDAENFISNIRVTVVKLKGSDNTFEC 120
IL2-m-mt   PKQATELKDLQCLERELGPLRHVLDLTQSKSFQLEDAENFISNIRRTVVKLKGSDNTFEC 120

IL2-h-wt   EYADETATIVEFLNRWITFCQSIISTLT- 133
IL2-m-wt   QFDDESATVVDFLRRWIAFCQSIISTSPQ 149
IL2-m-mt   QFDDESATVVDFLRRWIAFCTSIISTSPQ 149
```

Figure 3-4: Development of nanobody-IL-2 fusions.
(**A**), NJT6-IL2 (32.2 kDa), NJB2-IL2 (31.8 kDa), LMJ1.2C-IL2 (31.9 kDa), LMJ2.5I-IL2 (31.9 kDa), and NJB2-IL2-mt (31.8 kDa) on a non-reducing SDS-PAGE gel with Coomassie blue stain. (**B**), Size exclusion chromatography of indicated proteins using a Superdex200 Increase 10/300 GL column in PBS. (**C**), An alignment of wild-type human IL-2, wild-type murine IL-2, and inactive murine IL2-mt. The five mutations used to generate IL2-mt are highlighted. The three mutations highlighted in blue are described by Vazquez-Lombardi et al (*102*) to disrupt binding to the alpha subunit of human IL-2. The two mutations in red are described by Liu et al (*103*) to disrupt binding to the beta and gamma subunits of human IL-2.

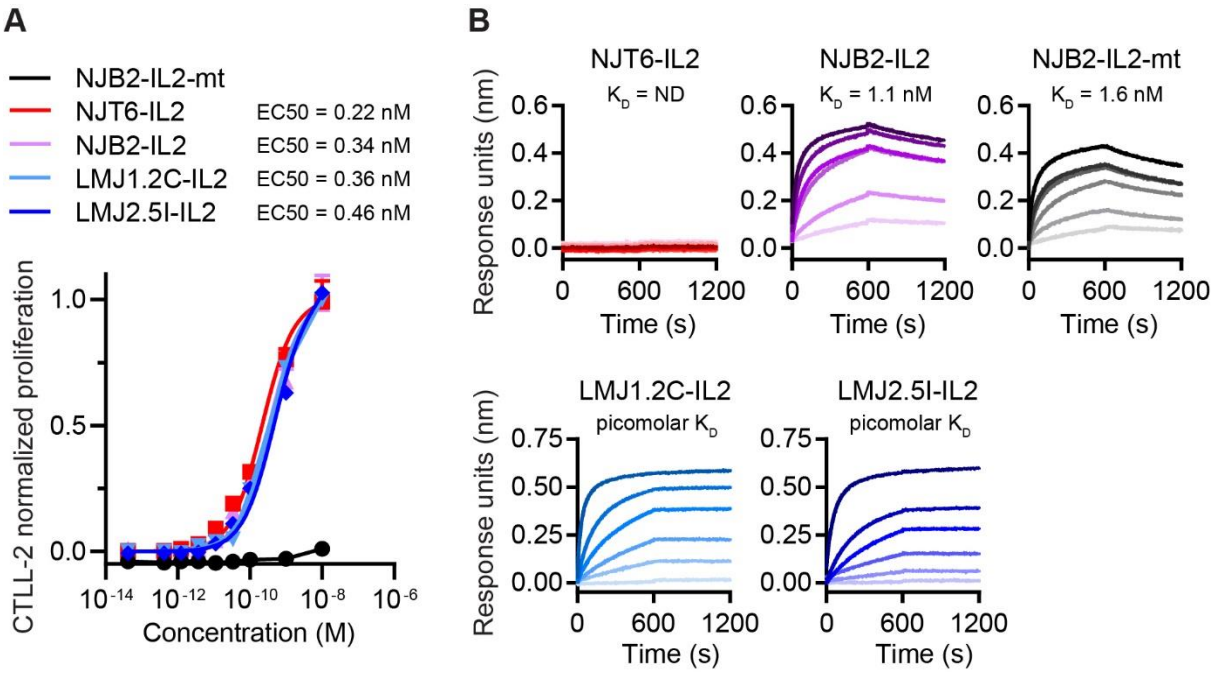

Figure 3-5: *In vitro* validation of nanobody-IL-2 fusions.
(**A**), Dose-dependent, normalized CTLL-2 cell proliferation in response to IL-2 fusion proteins (mean + SD; *n* = 3). (**B**), Association and dissociation curves (600 seconds each) are shown for indicated IL-2 fusions as measured by BLI using streptavidin tips coated with biotinylated EIIIB. Dark to light indicates analyte concentration of 100, 50, 30, 5, 3, and 1 nM for NJT6 and NJB2 fusions. Dark to light indicates analyte concentration of 100, 20, 5, 2.5, 1, and 0.1 nM for LMJ1.2C and LMJ2.5I fusions. ND, not determined.

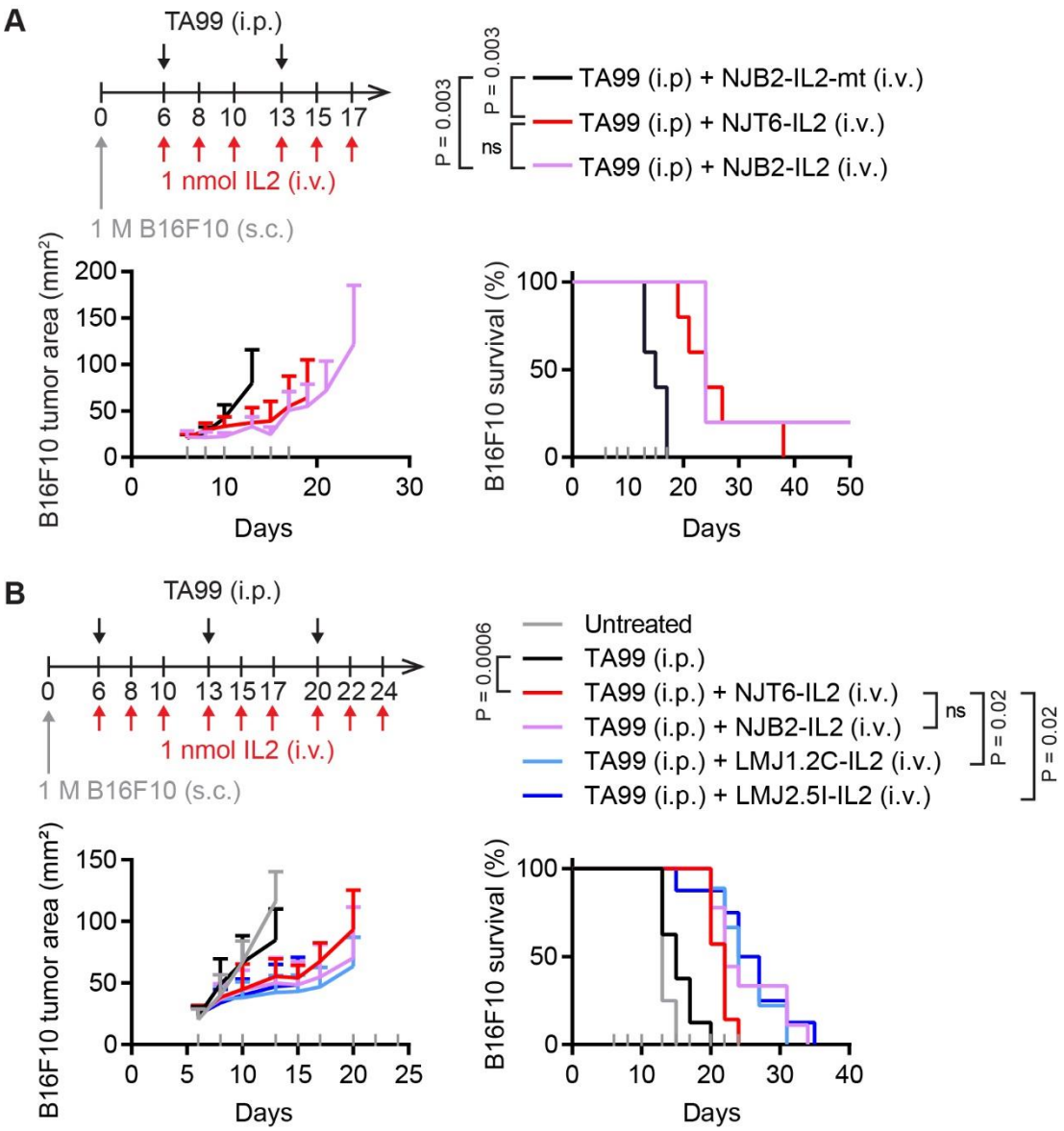

Figure 3-6: EIIIB-specific nanobody-IL-2 fusions lead to modest survival extension after intravenous dosing.

All mice were inoculated with 1 M B16F10 cells subcutaneously (s.c.) in the right flank on day 0. Mice were treated on days indicated with 100 μg TA99 (i.p.) and 1 nmol (32 μg) IL-2 fusions (i.v.). Tumor growth (left) and survival (right). Gray ticks above the x-axis mark treatment days. Tumor area (mean + SD) is shown until a mouse in that group is euthanized. Statistical significance for survival was generated by a log-rank Mantel-Cox test. (**A**), Results for mice given two weeks of treatment; *n* = 5 for all groups. (**B**), Results for mice given three weeks of treatment; *n* = 7~9.

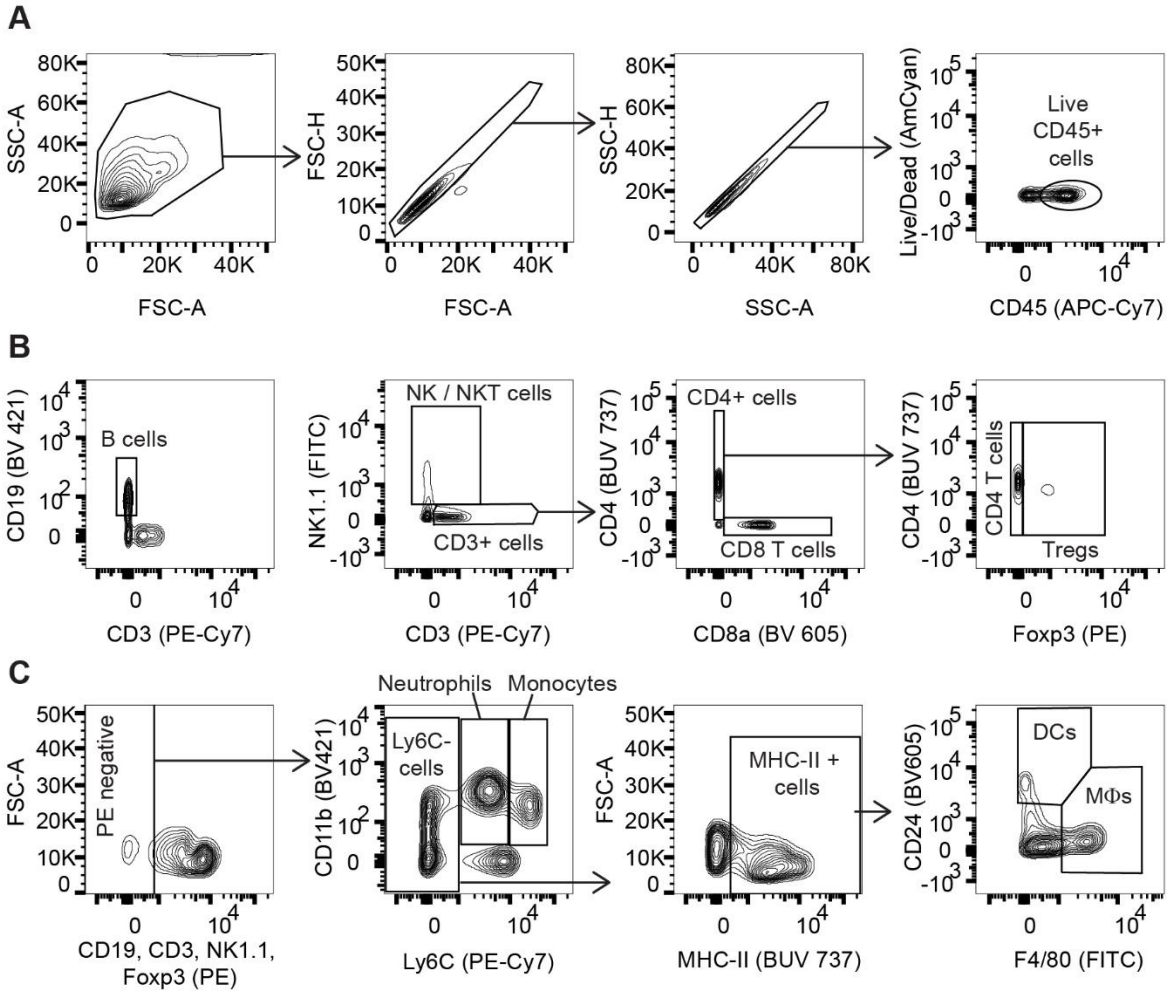

Figure 3-7: Flow cytometry gating for cellular biodistribution.
(**A**), To process flow cytometry data, cells were first gated for single cells, then gated for live CD45+ cells. (**B**), In one flow panel, live CD45+ cells were further gated into NK/NKT cells and T cell subsets. (**C**), In a separate flow panel, live CD45+ cells were gated for neutrophils, monocytes, dendritic cells (DCs), and macrophages (MΦs). The first gate excluded cells that expressed markers already used in the first panel.

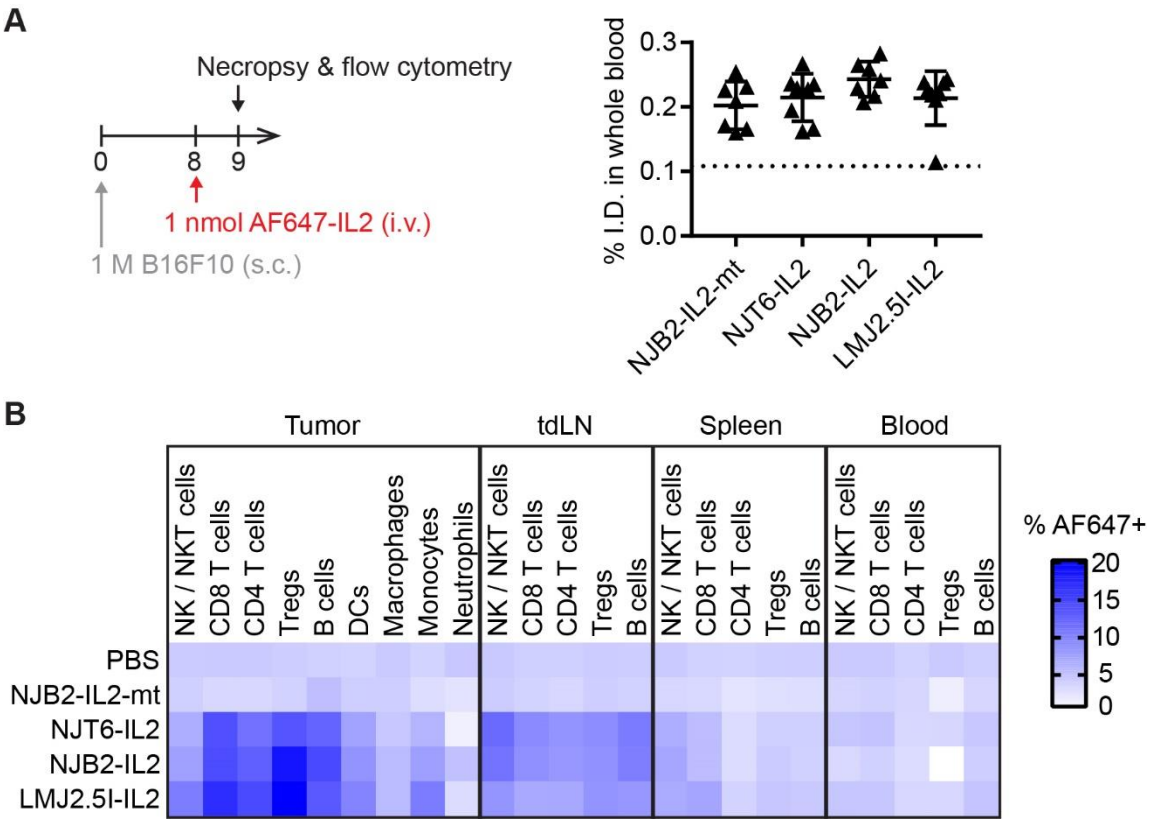

Figure 3-8: Nanobody-IL-2 fusions have similar cellular biodistribution after intravenous administration.

Mice were inoculated with 1 M B16F10 cells subcutaneously in the right flank on day 0. Mice were treated i.v. on day 8 with 1 nmol (32 μg) AF647-labeled IL-2 fusions. 24 hours later, mice were sacrificed for necropsy and flow cytometry. (**A**), 24 hours after treatment, blood was collected via cheek bleed and fluorescence of whole blood was measured. % injected dose (I.D.) was determined based on a standard curve of AF647-labeled immunocytokines added to blood from untreated mice *ex vivo*, and the assumption that the blood compartment in a mouse is 2 mL. Dotted line shows limit of detection. Mean ± SD; n = 7~8. (**B**), Heat map displaying % $AF647^+$ in indicated cell types and organs (mean of n = 5). Individual data points and statistics are reported in Fig. 3-9 and 3-10.

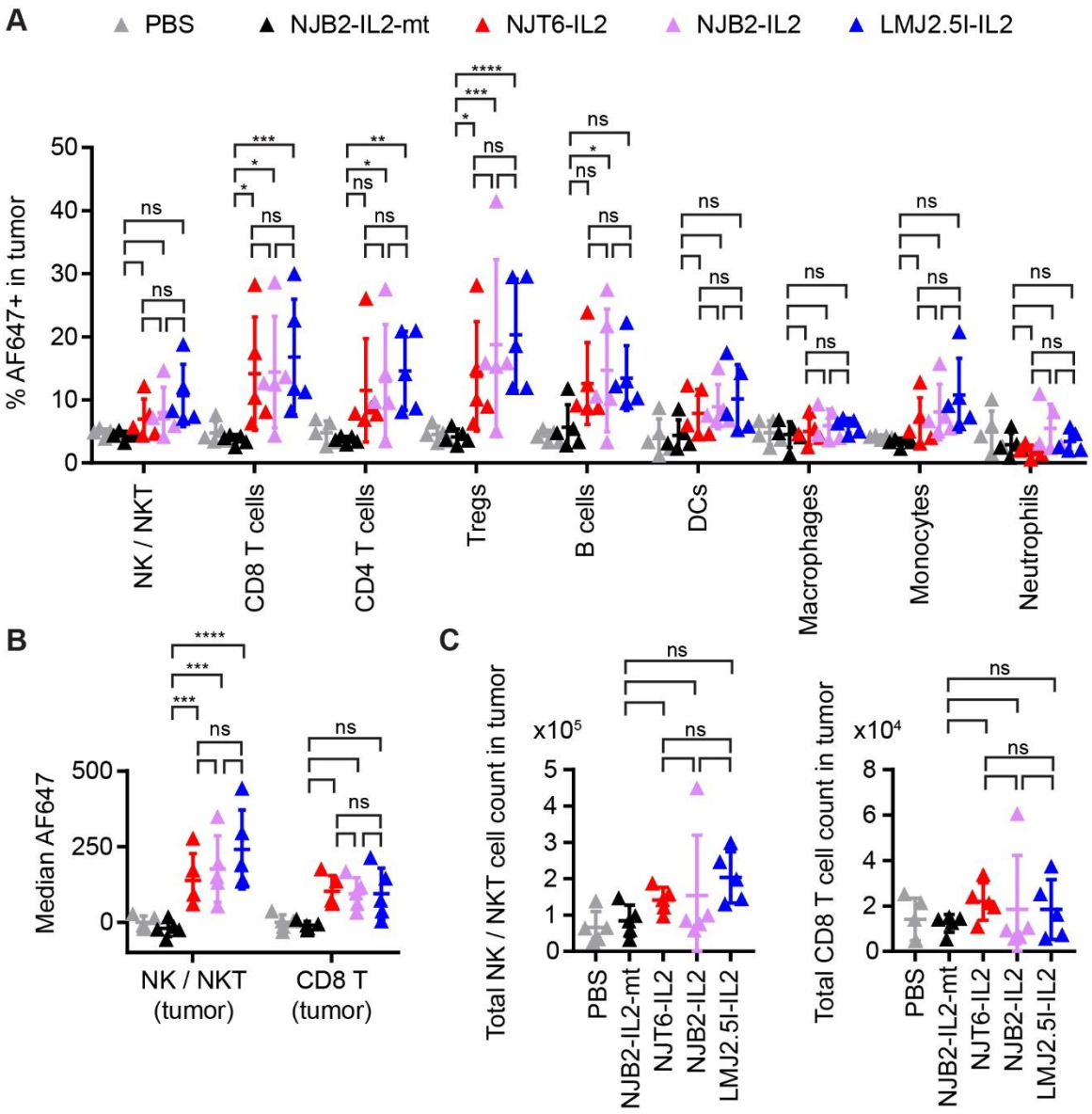

Figure 3-9: Nanobody-IL-2 uptake by immune cells in the tumor.
Mice were inoculated with 1 M B16F10 cells subcutaneously in the right flank on day 0. Mice were treated on day 8 with 1 nmol (32 µg) AF647-labeled IL-2 fusions (i.v.). 24 hours later, mice were sacrificed for necropsy and flow cytometry. (**A**), % AF647$^+$ in different cell populations at the tumor. (**B**), Median AF647 for NK/NKT cells and CD8$^+$ T cells in the tumor. When reporting median AF647, background levels from PBS mice was subtracted. (**C**), Total cell count in the tumor for NK/NKT cells and CD8$^+$ T cells. All data are shown as mean ± SD; *n* = 5. Data were analyzed with two-way analysis of variance (ANOVA) with Tukey's multiple comparisons test.

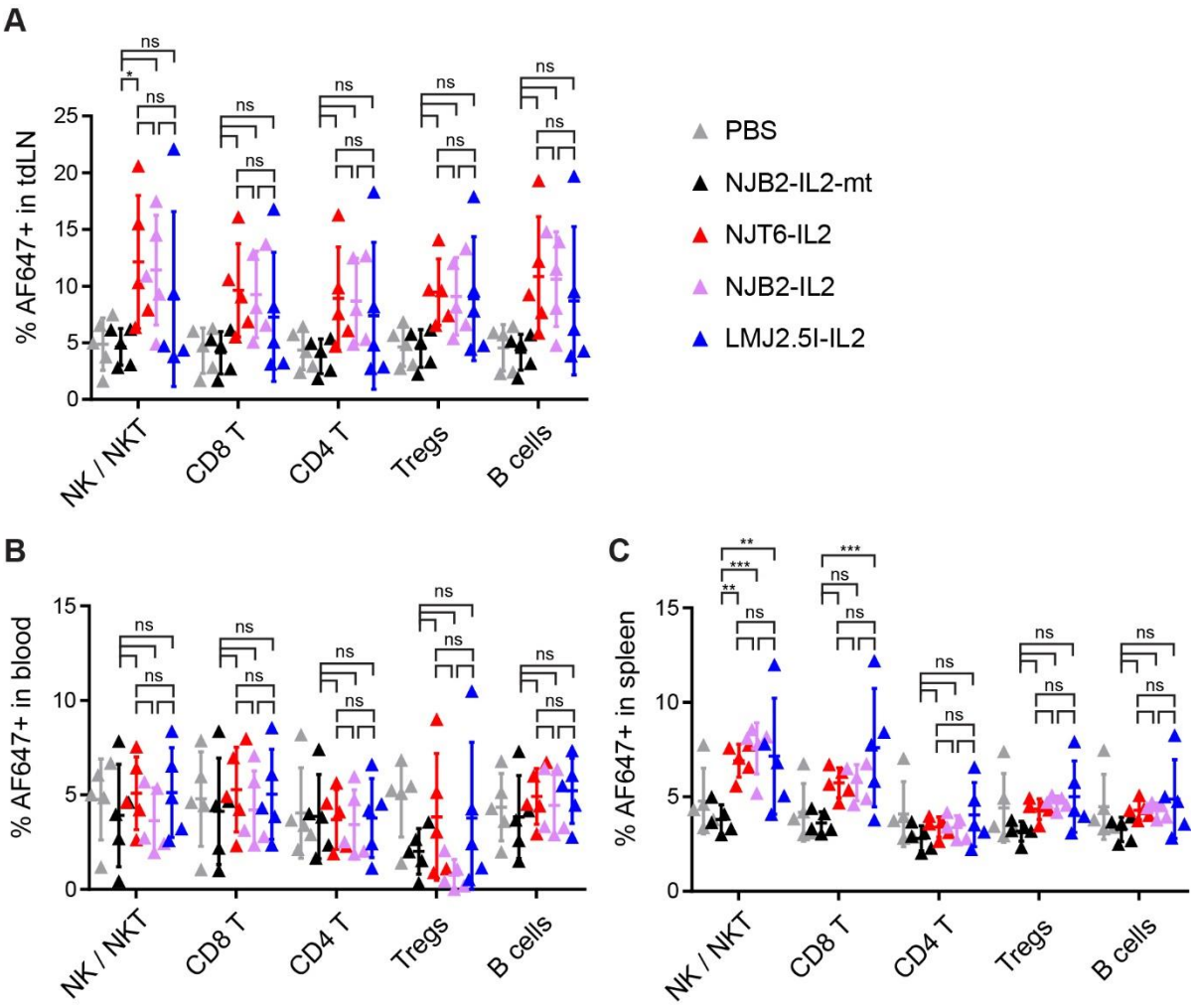

Figure 3-10: Nanobody-IL-2 uptake by immune cells in the tdLN, spleen, and blood.

Mice were inoculated with 1 M B16F10 cells subcutaneously in the right flank on day 0. Mice were treated on day 8 with 1 nmol (32 µg) AF647-labeled IL-2 fusions (i.v.). 24 hours later, mice were sacrificed for necropsy and flow cytometry. % AF647^{+} in different cell populations at the (**A**) tumor draining lymph node, (**B**), spleen, and (**C**), blood. All data are shown as mean ± SD; *n* = 5. Data were analyzed with two-way analysis of variance (ANOVA) with Tukey's multiple comparisons test.

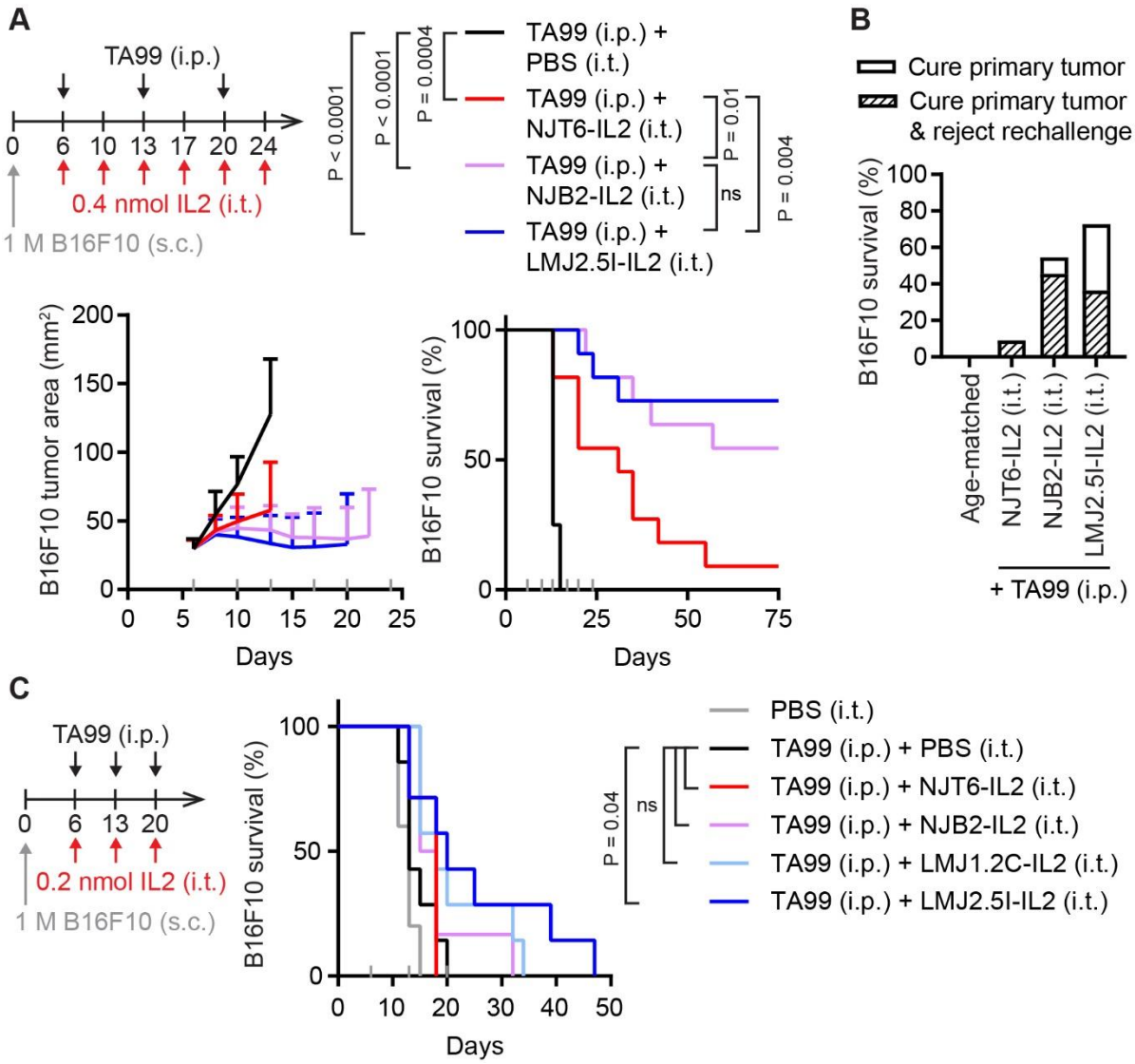

Figure 3-11: Intratumoral administration of EIIIB-specific nanobody-IL-2 fusions enables high B16F10 cure rate.

(**A**), Mice were inoculated with 1 M B16F10 cells subcutaneously (s.c.) in the right flank on day 0. Mice were treated on indicated days with 100 μg TA99 (i.p.) and 0.4 nmol (12.8 μg) IL-2 fusions (i.t.). Tumor growth (left) and survival (right). Gray ticks above the x-axis mark treatment days. Tumor area (mean + SD) is shown until a mouse in that group is euthanized. *n* = 8 for TA99 + PBS, *n* = 11 for all other groups. (**B**), Surviving mice were rechallenged with 0.1 M B16F10 cells subcutaneously in the left flank on day 94 and tumor growth was monitored with no additional treatment. (**C**), Mice were inoculated with 1 M B16F10 cells subcutaneously (s.c.) in the right flank on day 0. Mice were treated on indicated days with 100 μg TA99 (i.p.) and 0.2 nmol (6.4 μg) IL-2 fusions (i.t.). Gray ticks above the x-axis mark treatment days. *n* = 5 for PBS, *n* = 6~7 for all other groups. Statistics: survival comparisons were generated by a log-rank Mantel-Cox test. ns, not significant.

Table 3-1: Amino acid sequences of nanobodies.
Amino acid sequences are shown for recombinant nanobodies. The sequence for the nanobody is shown in blue. Glycine-serine linkers, sortase motifs (LPETG) and polyhistidine tags (HHHHHH) are shown in black.

Nanobody	Sequence
NJT6	QVQLVETGGDLVQPGGSLRLSCAASGLTLDYYAIGWVRQAPGKEREGVS CITPQDGNTYYDDSVMGRFTILRDNAKNMVYLQMNNLKPEDTAVYFCAAA GALTLDPSEYEYWGQGTQVTVSSGGGSLPETGGHHHHHH
NJB2	QVQLVETGGGLVQAGGSLRLSCAASGSTFSHNAGGWYRQAPEKQRELV AGISSDGNINYADSVKDRFTISRDNASNTMYLQMNNLKPEDTAVYVCNIRG SYGNTYYSRWGQGTQVTVSSGGGSLPETGGHHHHHH
LMJ1.2C	QVQLVETGGGLVQAGGSLRLSCAASGSTFSHSAGGWYRQAPEKQRELV AGIRSDGNINYADSVKDRFTISRDNASNTMYLQMNNLKPEDTAVYVCNIRG SYGNTYYSRWGQGTQVTVSSGGGSLPETGGHHHHHH
LMJ2.5I	RVQLVETGGGLVQAGGSLRLSCAVSGSTFSHSAGGWYRQAPEKQRELV AGIRSDGNINYADSVKDRFTISRDNASNTMYLQMNNLKPEDTAVYVCNIRG SYGNTYYSRWGQGAQVTVSSGGGSLPETGGHHHHHH
LMJ1.2G	QVQLVETGGGLVQAGGSLRLSCAASGSTFSHSAGGWYRQAPEKQRELV AGIGSDGNINYADSVKDRFTISRDNASNTMYLQMNNLKPEDTAVYVCNIRG SYGNTYYSRWGQGTQVTVSSGGGSLPETGGHHHHHH
LMJ1.3J	QVQLVGTGGGLVQAGGSLRLSCAASGSTFSHSAGGWYRQAPEKQRELV AGISSAGNINYADSVKDRFTISRDNASNTMYLQMNNLKPEDTAVYVCNIRG SYGNTYYSRWGQGTQVTVSSGGGSLPETGGHHHHHH
LMJ2.5C	QVQLVETGGGLVQAGGSLRLSCAASGSTFSHSAGGWYRQAPEKQRELV AGVRSDGNINYADSVKDRFTISRDNASNTMYLQMNNLKPEDTAVYVCNIR GSYGNTYYSRWGQGIQVTVSSGGGSLPETGGHHHHHH
LMJ2.5G	QVQLVETEGGLVQAGGSLRLSCAASGSTFSHSAGGWYRQAPEKQRELV AGIRSDGNINYADSVKDRFTISRDNASNTMYLQMNNLKPEDTAVYVCNIRG SYGNTYYSRWGQGTQVTVSSGGGSLPETGGHHHHHH
LMJ2.5H	QVQLVETGGGLVQAGGSLRLSCAVSGSTFSHSAGGWYRQAPEKQRELV AGIRSDGNINYADSVKDRFTISRDNASNTMYLQMNNLKPEDTAVYVCNIRG SYGNTYYSRWGQGTQVTVSSGGGSLPETGGHHHHHH
LMJ2.5J	QVQLVETRGGLVQAGGSLRLSCAVSGSTFSHSAGGWYRQAPEKQRELV AGIGSAGNINYADSVKDRFTISRDNASNTMYLQMNNLKPEDTAVYVCNIRG SYGNTYYSRWGQGTQVTVSSGGGSLPETGGHHHHHH
LMJ2.4C	QVQLVEAGGGLVQAGGSLRLSCAASGSTFSHSAGGWYRQAPEKQRELV AGIRSDGNINYADSVKDRFTISRDNASNTMYLQMNNLKPEDTAVYVCNIRG SYGNTYYSRWGQGIQVTVSSGGGSLPETGGHHHHHH
LMJ2.6A	RVQLVETGGGLVQAGGSLRLSCAVSGRTFSHSAGGWYRQAPEKQRELV AGIRSDGNINYADSVKDRFTISRDNASNTMYLQMNNLKPGDTAVYVCNIR GSYGNTYYSRWGQGTQVTVSSGGGSLPETGGHHHHHH

Table 3-2: Amino acid sequences of nanobody-IL-2 fusions.
Amino acid sequences are shown for nanobody-IL-2 fusions. The sequence for the nanobody is shown in blue and the sequence for murine IL-2 is shown in red. Glycine-serine linkers, sortase motifs (LPETG), and polyhistidine tags (HHHHHH) are shown in black.

IL-2 fusion	Sequence
NJT6-IL2	QVQLVETGGDLVQPGGSLRLSCAASGLTLDYYAIGWVRQAPGKEREGVS CITPQDGNTYYDDSVMGRFTILRDNAKNMVYLQMNNLKPEDTAVYFCAAA GALTLDPSEYEYWGQGTQVTVSSGGGGGSAPTSSSTSSSTAEAQQQQQ QQQQQQQHLEQLLMDLQELLSRMENYRNLKLPRMLTFKFYLPKQATELK DLQCLEDELGPLRHVLDLTQSKSFQLEDAENFISNIRVTVVKLKGSDNTFE CQFDDESATVVDFLRRWIAFCQSIISTSPQLPETGGHHHHHH
NJB2-IL2	QVQLVETGGGLVQAGGSLRLSCAASGSTFSHNAGGWYRQAPEKQRELV AGISSDGNINYADSVKDRFTISRDNASNTMYLQMNNLKPEDTAVYVCNIRG SYGNTYYSRWGQGTQVTVSSGGGGGSAPTSSSTSSSTAEAQQQQQQQ QQQQQHLEQLLMDLQELLSRMENYRNLKLPRMLTFKFYLPKQATELKDLQ CLEDELGPLRHVLDLTQSKSFQLEDAENFISNIRVTVVKLKGSDNTFECQF DDESATVVDFLRRWIAFCQSIISTSPQLPETGGHHHHHH
LMJ1.2C-IL2	QVQLVETGGGLVQAGGSLRLSCAASGSTFSHSAGGWYRQAPEKQRELV AGIRSDGNINYADSVKDRFTISRDNASNTMYLQMNNLKPEDTAVYVCNIRG SYGNTYYSRWGQGTQVTVSSGGGGGSAPTSSSTSSSTAEAQQQQQQQ QQQQQHLEQLLMDLQELLSRMENYRNLKLPRMLTFKFYLPKQATELKDLQ CLEDELGPLRHVLDLTQSKSFQLEDAENFISNIRVTVVKLKGSDNTFECQF DDESATVVDFLRRWIAFCQSIISTSPQLPETGGHHHHHH
LMJ2.5I-IL2	RVQLVETGGGLVQAGGSLRLSCAVSGSTFSHSAGGWYRQAPEKQRELV AGIRSDGNINYADSVKDRFTISRDNASNTMYLQMNNLKPEDTAVYVCNIRG SYGNTYYSRWGQGAQVTVSSGGGGGSAPTSSSTSSSTAEAQQQQQQQ QQQQQHLEQLLMDLQELLSRMENYRNLKLPRMLTFKFYLPKQATELKDLQ CLEDELGPLRHVLDLTQSKSFQLEDAENFISNIRVTVVKLKGSDNTFECQF DDESATVVDFLRRWIAFCQSIISTSPQLPETGGHHHHHH
NJB2-IL2-mt	QVQLVETGGGLVQAGGSLRLSCAASGSTFSHNAGGWYRQAPEKQRELV AGISSDGNINYADSVKDRFTISRDNASNTMYLQMNNLKPEDTAVYVCNIRG SYGNTYYSRWGQGTQVTVSSGGGGGSAPTSSSTSSSTAEAQQQQQQQ QQQQQHLEQLLMDLQELLSRMENYRNLKLPDMLTFEFYLPKQATELKDLQ CLERELGPLRHVLDLTQSKSFQLEDAENFISNIRRTVVKLKGSDNTFECQF DDESATVVDFLRRWIAFCTSIISTSPQLPETGGHHHHHH

Methods

Mice. B6 mice were purchased from Taconic (C57BL/6NTac) and The Jackson Laboratory (C57BL/6J). All animal work was conducted under the approval of the Massachusetts Institute of Technology Committee on Animal Care in accordance with federal, state, and local guidelines.

Cells. B16F10 cells were purchased from ATCC and cultured according to vendor instructions. HEK293-F cells were purchased from Life Technologies and cultured in FreeStyle293 Expression Medium (Life Technologies). CTLL-2 cells were purchased from ATCC and cultured in RPMI-1640 (ATCC) supplemented with 10% fetal bovine serum (Thermo Fisher Scientific), 10% T cell culture supplement with concanavalin A (T-STIM with ConA, Corning), 20 mM HEPES, 1 mM sodium pyruvate, 0.05 mM β-mercaptoethanol (Life Technologies), 100 units/mL penicillin (Life Technologies), 100 µg/mL streptomycin (Life Technologies), 2 mM L-alanyl,-L-glutamine (Life Technologies), and 1x minimal essential medium non-essential amino acids (Corning). All adherent cells were maintained at 37 °C and 5% CO_2. All cell lines tested negative for mycoplasma.

Yeast surface display. The antigen for yeast display was the protein fragment of fibronectin (FN) splice variant EIIIB, previously made in the Hynes laboratory (*120*, *121*). EIIIB was biotinylated using ChromaLink NHS-biotin reagent (Solulink) following manufacturer's protocol. Yeast selections were performed following previous protocols (*98*, *122*, *123*). An initial yeast library of diversity 4E7 was generated via 20~40 cycles of error-prone PCR (using 2 µM each of 8-oxo-dGTP and dPTP) on plasmid DNA containing NJB2. The nanobody library was displayed on the surface of *Saccharomyces cerevisiae* (yeast) strain EBY100 using the pCTcon2 plasmid, resulting in expression of Aga2p - HA tag - $(G_4S)_3$ linker – nanobody – G_3S linker - cMyc tag. The yeast library went through 3 initial rounds of equilibrium sorting (sorts 1.2, 1.3, 1.4) where yeast were incubated in PBS 0.1% BSA with 10 nM biotinylated EIIIB, chicken-anti-cMyc (Exalpha) and mouse-anti-HA (BioLegend 16B12) for at least 1 hour. Yeast were washed, and secondarily stained with Streptavidin Alexa Fluor 647 (Invitrogen S21374), goat-anti-chicken Alexa Fluor488 (Invitrogen A11039), and goat-anti-mouse PE (Invitrogen P-852) for 30 minutes. Yeast were washed and sorted on a BD FACSAria III Cell Sorter. The top 0.1~1% of yeast were sorted for binding to EIIIB, as determined by Streptavidin-AF647 (Fig. 3-2). Sorted yeast were grown up for the next round of sorts. After three initial equilibrium sorts, a second yeast library of diversity 6E7 was generated as before, but now with 60 cycles of error-prone PCR on an equimolar mixture of plasmid DNA containing clones LMJ1.2C, LMJ1.2G and LMJ1.3J. The second library went through equilibrium sorts as before, but at 50 nM and 0.5 nM biotinylated EIIIB (sorts 2.2 and 2.3, respectively). We next performed kinetic sorts, where yeast were incubated in PBS 0.1% BSA with 50~100 nM biotinylated EIIIB for at least 1 hour, washed, then resuspended in 100 nM unlabeled EIIIB at 4 °C for 24 hours (sort 2.4), 4 °C for 72 hours (sort 2.5), or room temperature for 72 hours (sort 2.6). In sorts 2.5 and 2.6, we also gated for equal expression of HA and cMyc to prevent selective pressure for mutations in cMyc. After each sort, plasmid DNA of sorted yeast was isolated using Zymoprep Yeast Plasmid Miniprep II Kit (Zymo research). Isolated plasmid DNA was transformed into Stellar Competent cells to isolate individual colonies for Sanger sequencing. To visualize mutations, the structure of the NJB2

nanobody was predicted using ABodyBuilder on the SAbPred server (*99*, *100*) based on PDB 7KKJ (*124*). Graphics were generated using UCSF Chimera (*101*).

Nanobody sub-cloning, expression and purification in WK6 cells. The engineered nanobody sequences were sub-cloned from the yeast display vector pCTcon2 into the pHEN6 periplasmic expression vector with a C-terminal LPETG sortase motif followed by a 6-His tag (Table 3-1). Proteins were expressed in WK6 *E. coli* cells. 1 mM IPTG was used to induce protein expression at OD600 = 0.6 (16 hours at 30 °C). The His-tagged nanobody present in the periplasmic fraction was extracted by osmotic shock and purified using Ni-NTA beads (Qiagen). To confirm the molecular weights, proteins were run alongside the Precision Plus Kaleidoscope Prestained Protein standards (Biorad) on a Novex 4-20% Tris-Glycine gel and stained in Coomassie blue stain. The purified protein was buffer exchanged into PBS and concentrated using 10K Amicon filters (EMD Millipore), flash frozen in liquid nitrogen and stored at -80 °C. Nanobodies expressed in WK6 cells were only used *in vitro* to test EIIIB affinity and specificity.

C-terminal sortase tagging. C-terminal sortase tagging with biotin was done using the *Staphylococcus aureus* sortase A (pentamutant variant 5M-SrtA). The sortase was expressed and purified as previously described (*125*). For biotin tagging, sortase (5 μM) was incubated with purified His-tagged nanobodies (150 μM) and nucleophile (GGGK-Biotin, 500 μM) in sortase buffer containing 50 mM Tris·HCl, pH 7.5, 150 mM NaCl, 10 mM $CaCl_2$ for 3-12 hours at 4 °C. The unreacted sortase and His-tagged nanobody were removed by incubation with Ni-NTA beads with agitation for 5 min at 25 °C followed by centrifugation. The biotin-tagged nanobodies were buffer-exchanged into PBS and concentrated using 3K 0.5 mL Amicon filters (EMD Millipore) and stored at -20 °C with 5% glycerol.

Affinity determination by Bio-Layer Interferometry. To determine the affinities of the recombinant nanobodies, bio-layer interferometry (BLI) was done using a ForteBio Octet RED96 bio-layer interferometer (Pall ForteBio). Streptavidin-coated BLI biosensor tips (ForteBio) were soaked in the assay running buffer (PBS, 0.05% Tween-20, 1% recombinant human albumin (Sigma)) for 10 minutes. Biotinylated EIIIB was then immobilized on streptavidin-coated BLI biosensor tips by immersion in a 2 μg/mL solution. The association and dissociation were analyzed for different concentrations of analyte ranging from 0.1-350 nM. Association and dissociation rate constants were determined using the ForteBio data analysis software (V8.2) using the 1:1 binding model and a global fit analysis with double referencing.

Immunoblotting. Samples including recombinant proteins, murine plasma fibronectin (Abcam) and human plasma fibronectins (BD Biosciences), and in-house ECM-enriched samples from murine lung were prepared in Laemmli buffer containing 100mM dithiothreitol. All proteins were separated by SDS-PAGE on 4-20% Tris-Glycine gradient Gels (Novex) and transferred onto nitrocellulose membranes (Millipore, Billerica). Immunoblotting was performed using biotin-tagged nanobodies. Following primary antibody incubation, the membranes were washed and incubated in the presence of HRP-Streptavidin (BD Biosciences). Membranes were washed and incubated with Western Lightning Chemiluminescence Reagent (PerkinElmer LAS).

Cloning and Protein Production of therapeutic proteins. The nanobody cDNA was amplified by PCR and fused with murine IL-2 cDNA containing the C-terminal LPETG sortase motif followed by a 6-His tag. The fusions were cloned by In-Fusion snap assembly kits (Takara Bio) into the gWIZ vector (Genlantis). Sequences are shown in Table 3-2. Plasmids were transformed and amplified in Stellar competent cells and purified using NucleoBond Xtra endotoxin-free Midi prep kit (Macherey-Nagel). Sterile plasmid DNA encoding each protein was transfected into suspension HEK293 cells with Polyethylenimine (Polysciences 23966) in OptiPRO Serum Free Medium (Thermo Fisher). Nanobody-IL-2 fusions were purified using TALON Metal Affinity Resin (Takara Bio). TA99 was purified using rProtein A Sepharose Fast Flow Resin (Cytiva). Some IL-2 fusions were further purified by size exclusion chromatography using a Superdex 200 Increase 10/300 GL column on an ÄKTA FPLC (GE Healthcare). All proteins were buffer-exchanged into sterile PBS (Corning), 0.22-μm sterile filtered (Corning), and confirmed for minimal endotoxin (<0.1 EU per dose) as measured by a LAL Chromogenic Endotoxin Quantitation Kit (Pierce). To confirm molecular weight, proteins were run alongside a Novex Sharp Pre-Stained Protein Standard on an NuPAGE 4-12% Bis-Tris gel (Invitrogen) in MES running buffer and stained in SimplyBlue SafeStain (Life Technologies). Proteins were flash frozen in liquid nitrogen and stored at -80 °C.

CTLL-2 proliferation assay. CTLL-2 cells were seeded onto 96-well tissue culture plates at 5000 cells/well in 100 μL of media without T-STIM and without ConA. Cells were cultured for 48 hours with varying concentrations of nanobody-IL-2 fusions. Cell proliferation was determined by WST-1-based colorimetric assay (Roche) according to manufacturer's instructions. Absorbance at 450 nm with reference absorbance at 650 nm was measured using an Infinite M1000 microplate reader (Tecan).

In vivo tumor survival. 7~8-week-old female mice were inoculated on day 0 with B16F10 tumors (1 M cells in 50 μL PBS injected subcutaneously in the right flank). Treatments initiated on day 6 when tumors were established (average 25 mm^2). TA99 was dosed intraperitoneally at 100 μg in 100 μL PBS once per week. For intravenous IL-2 treatments, 1 nmol (32 μg) of nanobody-IL-2 fusion in 70 μL PBS was injected retro-orbitally thrice per week. For intratumoral IL-2 treatments, nanobody-IL-2 fusion in 20 μL PBS was injected intratumorally at either 0.4 nmol twice per week, or 0.2 nmol once per week. Mice underwent two to three weeks of treatment, as outlined in each experimental figure. Tumor area (length x width) and body weight were recorded three times per week. Mice were euthanized when their tumor area exceeded 100 mm^2. Cured mice (surviving at 94 days) along with age-matched control mice were rechallenged on day 94 with 0.1 M B16F10 cells in 50 μL PBS injected subcutaneously in the left flank. Tumor growth was monitored and mice were euthanized when their tumor area exceeded 100 mm^2.

Fluorescently labeling nanobody-IL-2 fusions. Fluorescently-labeled proteins were prepared by incubating proteins (1 mg/mL in PBS with 0.1 M K_2HPO_4, pH 9) with 6-fold molar excess of AF647 NHS ester (Invitrogen A20006) for 1.5 hours at room temperature in the dark. Free dye was removed using 10K Amicon filters (EMD Millipore) and two successive PD SpinTrap G-25 columns (Cytiva). Dye to protein ratios ranged from 1.5 to 2. Fluorescently-labeled and

unlabeled nanobody-IL-2 fusions were prepared such that each dose contained 1 nmol nanobody-IL-2 and 1.5 nmol dye.

Cellular biodistribution. Cellular biodistribution was profiled similar to Tzeng et al (*18*). 7-week-old female mice were inoculated on day 0 with 1 M B16F10 cells in 50 µL PBS injected subcutaneously in the right flank. On day 8, mice were treated retro-orbitally with 1 nmol AF647-labeled nanobody-IL-2 in 70 µL PBS. 24 hours later, blood was collected via cheek bleed into K2 EDTA tubes (Greiner Bio-one 450480). Mice were euthanized and tumors, tumor draining lymph nodes (tdLNs), and spleens were harvested and weighed. Tumors and tdLNs were mechanically dissociated, then incubated in RPMI 1 mg/mL Collagenase/Dispase (Sigma 11097113001), 20 µg/mL DNase I (Sigma 10104159001). Organs were rendered into single-cell suspension by filtration through 70-µm mesh screens. Spleens and blood were resuspended in ACK Lysing Buffer (Gibco A1049201). Cells were stained with Zombie Aqua viability dye (BioLegend 423101), then blocked with CD16/CD32 antibody (eBioscience Clone 93). In one panel, cells were stained with the antibodies APC/Cy7-CD45 (BioLegend 30-F11), PE/Cy7-CD3 (BioLegend 17A2), BV421-CD19 (BioLegend 6D5), FITC-NK1.1 (BioLegend PK136), BV605-CD8a (BioLegend 53-6.7), BUV737-CD4 (BD Biosciences GK1.5), and PE-FOXP3 (BioLegend 150D). In a separate panel, we gated for immune cells as previously described (*126*) using the antibodies APC/Cy7-CD45 (BioLegend 30-F11), PE/Cy7-Ly6C (BioLegend HK1.4), BV421-CD11b (BioLegend M1/70), BUV737-I-A/I-E (BD Biosciences M5/114), FITC-F4/80 (BioLegend BM8), BV605-CD24 (BioLegend M1/69), and a PE-dump channel with PE-CD3, PE-NK1.1, PE-CD19, PE-FOXP3 (BioLegend, same clones as above). Cells were fixed and intracellular staining was performed in Permeabilization Buffer (Invitrogen) according to manufacturer's instructions. Samples were run on a BD LSRFortessa HTS-1 analyzer and data were analyzed with FlowJo software (V10.4). Gating strategy is shown in Fig. 3-7. When reporting median AF647, background levels from PBS mice was subtracted.

Statistical analysis. Statistical analysis was performed with GraphPad Prism software (V7). Survival curves were compared by log-rank Mantel-Cox test. As described in figure legends, comparisons between groups were assessed by two-way analysis of variance (ANOVA) with Tukey's multiple comparisons test. The *n* values are indicated in figure legends and *P* values are shown in the figures.

Acknowledgments

Chapter 3 was performed with equal contributions from Emi Lutz, Noor Jailkhani, and Noor Momin. I am very grateful to Noor Jailkhani and Noor Momin for being wonderful collaborators and mentors. We thank Prof. Richard O. Hynes and Prof. K. Dane Wittrup for their guidance in designing experiments, interpreting results, and writing a manuscript. We also thank Ying Huang, Allison Sheen, and Byong Kang for their help in performing experiments.

We thank the Koch Institute's Robert A. Swanson (1969) Biotechnology Center (National Cancer Institute Grant P30-CA14051) for technical support, especially the Flow Cytometry Core Facility. We thank the MIT Biology Biophysical Instrumentation Facility for the Study of Complex Macromolecular Systems (National Science Foundation Grant 0070319) for enabling use of the Octet Bio-Layer Interferometry System (National Institutes of Health Grant S10 OD016326). Nanobody graphic was performed with UCSF Chimera, developed by the Resource for Biocomputing, Visualization, and Informatics at the University of California, San Francisco.

Funding:

This work was supported by the National Cancer Institute Grant NCI CA174795 (to Prof. Wittrup), the National Institute of Biomedical Imaging and Bioengineering R01EB031082 (to Prof. Wittrup and Prof. Irvine), the Department of Defense Breast Cancer Research Program Investigator Award W81XWH-14–1-0240 (to Prof. Hynes), and the Massachusetts Institute of Technology Ludwig Center for Molecular Oncology (to Prof. Hynes).

Personnel were supported by the NSF Graduate Research Fellowships Program (EAL, NM, AS), NIH / NIGMS Biotechnology Training Program (EAL, NM), Siebel Scholar Award (EAL, NM), the Mazumdar-Shaw International Oncology Fellowship (NJ), and the Hope Babette Tang Student Research Fund, the Kristin R. Pressman and Jessica J. Pourian Koch Institute Fund, and the Charles S. Krakauer Fund (EAL).

Competing Interests:

Richard O. Hynes, K. Dane Wittrup, Noor Jailkhani, Noor Momin, and Emi Lutz are named as inventors in a patent application filed by the Massachusetts Institute of Technology related to the data presented in this chapter (Application number 63/304,954). Richard O. Hynes and Noor Jailkhani are named as inventors in a patent application filed by the Massachusetts Institute of Technology related to the data presented in this chapter (US20190225693A1).

Chapter 4. DNA-based cGAS agonists

Abstract

The cGAS-STING pathway is a promising therapeutic target that leads to type I interferon production. This pathway has been studied most commonly in the context of cyclic dinucleotides that activate STING. Here we explore the benefits and challenges of DNA-based therapies that activate the upstream receptor cGAS. A modified, 45 base-pair DNA delayed tumor growth in mice in a STING-dependent manner. We begin testing delivery agents and oligonucleotide sequences aimed to improve the potency of cGAS agonists. The current iterations of DNA-based cGAS agonists had inferior efficacy compared to cyclic dinucleotides in tumor-bearing mice, but continued research may yield more potent DNA therapies.

Introduction

Type I interferons (IFNs) are essential for effective anti-tumor immunity in mice (*42–44*). As discussed in Chapter 2, type I IFNs themselves can be potent anti-cancer drugs. However, several innate immune signaling pathways lead to type I IFN production, and these upstream pathways can also be activated therapeutically. In particular, the cGAS-STING pathway has gained attention in recent years (*127*, *128*). Upon detecting the danger signal of cytosolic DNA, cyclic GMP-AMP (cGAMP) synthase (cGAS) (*129*, *130*) produces cGAMP, a type of cyclic dinucleotide (CDN), from ATP and GTP. Small molecule CDNs are sensed by the Stimulator of Interferon Genes (STING), and drive type I interferon production. This innate immune pathway is particularly important because spontaneous T cell priming against tumor associated antigens is driven by cGAS-STING pathway recognition of tumor-derived DNA (*128*, *131*).

CDN-based STING agonists have been studied extensively, and intratumoral treatments of synthetic CDNs enable control of primary, distal, and rechallenge tumors in mice (*132*, *133*). This motivated several on-going clinical trials with CDNs, but effective activation of the cGAS-STING pathway is still challenging (*70*, *134*). We hypothesized that developing DNA-based cGAS agonists may have advantages over CDN-based STING agonists. Since one piece of DNA can activate cGAS to produce many CDN molecules, DNA-based drugs have the potential to be more potent. DNA is also easily modulated, and technologies that enhance the cytosolic delivery or stability of DNA have been studied for decades. In this chapter, we designed DNA-based cGAS agonists, tested them in mice, and observed some anti-tumor efficacy.

Results

DNA-based cGAS agonists delay tumor growth.

To design cGAS agonists, we started with a 45 bp double-stranded DNA (dsDNA) sequence called Baseline DNA (**Fig. 4-1A**). dsDNA of ~45 bp is necessary for efficient activation of human cGAS (*135*), while mouse cGAS is capable of responding to shorter dsDNA lengths (*136*, *137*). This Baseline DNA sequence contains no CpG motifs (which activate a

different sensor TLR9), and was derived from a sequence commonly used in the field called Immunostimulatory DNA (ISD) (*136*, *138*). Next, we applied known modifications that could boost therapeutic potential to activate cGAS. Herzner and colleagues found that unpaired guanosines flanking short DNA enhances cGAS activation (*139*), so we changed the ends of Baseline DNA to three, unpaired guanosines (GGG-DNA). Phosphorothioate (PS) linkages are a common chemical modification that enhances oligonucleotide stability (*140*, *141*). We incorporated PS linkages at the ends of the DNA to protect from exonucleases (PS-DNA), and also examined DNA with both unpaired guanosines and PS linkages at the ends (GGGPS-DNA).

DNA were complexed with Lipofectamine 2000 and tested on RAW-Lucia ISG cells, a murine macrophage reporter cell line for the induction of interferon-stimulated genes. Baseline DNA led to mild activation of the macrophages. Both GGG-DNA and PS-DNA improved activation over Baseline DNA. GGGPS-DNA, which included both modifications, had the most potent effect. None of the DNA had activity in a cGAS KO version of the cell line, demonstrating the assay's specificity for cGAS. As a second method to measure DNA immunostimulatory activity *in vitro*, we recombinantly expressed the catalytic domain of murine cGAS (**Fig. 4-1B**). cGAS was incubated with DNA, ATP, GTP, and $MgCl_2$ for 2 hours, and cGAMP production was measured by anion exchange. GGGPS-DNA again activated cGAS to a greater extent than Baseline DNA (**Fig. 4-1C**).

To test cGAS agonists *in vivo*, mice bearing subcutaneous B16F10 tumors were treated intratumorally (i.t.) with PBS or 225 μg GGGPS-DNA. In WT mice, DNA significantly extended survival ($P = 0.0006$) (**Fig. 4-2A**) and delayed tumor growth (**Fig. 4-2B**). The efficacy was lost in STING-deficient mice, indicating that the therapy was activating the intended pathway. Treated mice did not lose body weight, which is one metric for toxicity (**Fig. 4-2C**).

Delivery challenges for cGAS agonists.

Although GGGPS-DNA as a single agent slowed B16F10 tumor growth, all mice succumbed to disease before day 25 (**Fig. 4-2**). This may be attributed to several key challenges that DNA-based cGAS agonists face. First, nucleic acids can be quickly degraded *in vivo* (*142*). Second, delivery to cytosolic cGAS is difficult because oligonucleotides have poor intracellular delivery (*142*). Third, DNA drugs of this size are poorly retained in the tumor upon intratumoral injection. To characterize the challenge of intratumoral retention, we injected AF647-labeled DNA into B16F10 tumors. Most of the fluorescent signal was lost within hours, indicating rapid degradation or leakage from the tumor (**Fig. 4-3A**).

We investigated several strategies to address these delivery issues. As one example, we hypothesized that a transfection reagent would improve intracellular delivery. Lipofectamine 2000 is a commonly used transfection reagent, and enables intracellular delivery of cGAS agonists into cells *in vitro* (**Fig. 4-1A**). However, addition of Lipofectamine 2000 *in vivo* did not improve therapeutic efficacy (**Fig. 4-3B**).

We also tested cGAS agonists co-delivered with aluminum hydroxide (alum) particles. Alum, discussed in detail in Chapter 2, is a commonly-used material that is FDA-approved as a vaccine adjuvant. Drugs that contain phosphate groups, including DNA, bind tightly to alum through a ligand exchange reaction with surface hydroxyls (*38*, *58*, *59*, *143*). When phosphate-containing drugs are mixed and co-injected with alum into the tumor, alum can serve as an intratumoral depot that enables long-term intratumoral retention (*38*). However, adding alum to the cGAS agonist GGGPS-DNA did not improve survival, and the STING agonist cGAMP yielded superior efficacy (**Fig. 4-3B**).

Aptamer selections against cGAS

We next investigated if the DNA payload itself could be optimized to activate cGAS. Although cGAS is generally considered sequence agnostic, there are oligonucleotide structures (*139*, *144*) and lengths (*135–137*) that improve cGAS activation, as well as sequences that can inhibit cGAS (*145*). Since oligonucleotide affinity to cGAS has correlated with cGAS activity (*146*, *147*), we hypothesized that selecting a DNA aptamer library for affinity to cGAS could yield potent cGAS agonists. Although cGAS is typically activated by dsDNA, we worked with ssDNA because secondary structure within ssDNA oligos is known to weakly activate cGAS to some degree (*136*, *139*, *147*), and ssDNA aptamers make more unique, complex structures. We panned a ssDNA aptamer library against recombinant biotinylated cGAS and collected bound aptamers with streptavidin magnetic beads. ssDNA aptamers were amplified using asymmetric PCR between rounds of selections.

After several rounds of selections, a consensus motif GGGCCGCCC emerged. After multiple rounds of selections, aptamer lengths (~10 nt) were shorter than the original aptamer library size (40 nt), indicating that truncations occurred during PCR, and PCR amplification bias likely played a role during selections. Optimizing the asymmetric PCR protocol is necessary to solve this issue. Nevertheless, the motif dominated the library, and affinity to cGAS may have also played some role during selections. Adding this motif to ssDNA indeed improved the activation of RAW Lucia macrophages (**Fig. 4-4**). A standard 51 nt ssDNA (**Fig. 4-4B**) could not activate the macrophages, but upon addition of the GGGCCGCCC motif, the 51 nt ssDNA (**Fig. 4-4C**) had similar activity to 51 bp dsDNA (**Fig. 4-4A**). The benefit was lost when the motif's cytosines were exchanged for thymines (**Fig. 4-4D**), indicating sequence specificity. The motif added activity to ssDNA strands whether it was located in the center (**Fig. 4-4 B vs. C**) or the end of the ssDNA (**Fig. 4-4 E vs. F**). However, ssDNA with the GGGCCGCCC motif was far less potent than 51 bp dsDNA that contained the previously known, simpler unpaired GGG motif (**Fig. 4-4G**) (*139*). dsDNA with the GGGCCGCCC motif incorporated was also not particularly potent (data not shown). Although the GGGCCGCCC motif may not be a promising therapeutic candidate, these selections served as a proof of principle that aptamer selections may reveal oligonucleotide sequences that preferentially activate cGAS.

Discussion

In this chapter, we designed DNA-based cGAS agonists and administered them intratumorally to slow B16F10 tumor growth in mice. Other groups have also recently developed

DNA-based cGAS agonists. Laursen and colleagues conjugated 60 bp DNA to an anti-CD11c antibody and activated cGAS in dendritic cells *in vitro* (*148*). Garland and colleagues designed NanoISD, a phosphorhioate-capped 95 bp dsDNA complexed to a polymer (*149*). NanoISD slowed B16F10 and MC38 tumor growth in mice after intratumoral administration at 2 μg DNA in a 100 μL injection volume (*149*). Together, these studies demonstrate that cGAS activation by DNA-based therapies is possible for cancer.

These DNA-based cGAS agonists may be improved by further stabilizing modifications. The phosphorothioate modification is the most common backbone modification that has enabled other oligonucleotide therapies like siRNA and antisense oligonucleotides (*140*, *141*). However, we and others have observed that DNA with a full PS backbone no longer activates cGAS (*136*, *149*). Finding other stabilizing modifications that protect DNA while maintaining cGAS activity will be key. Alternatively, co-injecting inhibitors of nucleases like TREX1 may be useful to increase the recognition of both endogenous and therapeutically delivered DNA (*150*, *151*).

Efficient delivery agents will also be critical for cGAS agonists. Here, Lipofectamine 2000 and alum did not improve the efficacy of GGGPS-DNA. We incorporated as much delivery agent as possible while maintaining a total 20 μL intratumoral dose. Intratumoral treatments are limited by a maximum volume that the tumor can hold, which is related to the tumor's size and interstitial void volume fraction (*31*). Momin et al found that for protein therapies, B16F10 tumors only held about 30% of an injected 20 μL dose, and the excess leaked immediately into circulation (*31*). Due to these restrictions on dosing volume, the large 225 μg dose of DNA likely exceeded the capacity of the relatively small amount of Lipofectamine 2000 and alum. Delivery agents with higher efficiency and capacity will be useful for intratumoral oligonucleotide therapies. Delivery agents designed for long-term intratumoral retention may also help maximize on-target, anti-tumor effects and minimize potential systemic toxicity (*31*, *38*).

DNA's stability, intracellular delivery, and retention at the tumor are large hurdles. Once these challenges are met and DNA is efficiently delivered to cGAS in the tumor microenvironment, the DNA payload itself can also be optimized. These designs can be found by studying pathogens, such as when Herzner and colleagues found the potent unpaired guanosine motif from HIV-1 reverse transcripts (*139*). As an alternative approach, here we present a proof of principle that aptamer libraries can be panned against recombinant cGAS. Repeating and improving the aptamer selections may yield additional oligonucleotide motifs with stronger activation of cGAS. A more potent DNA payload itself with help amplify the effects of cGAS therapies.

Although there is promise and future work for cGAS agonists, this project ultimately focused on engaging the cGAS-STING pathway further downstream by engineering type I IFN therapies directly (see Chapter 2). However, continuing to develop agonists that intersect at various points in the innate immune system will no doubt help advance our treatment of cancer.

Figures

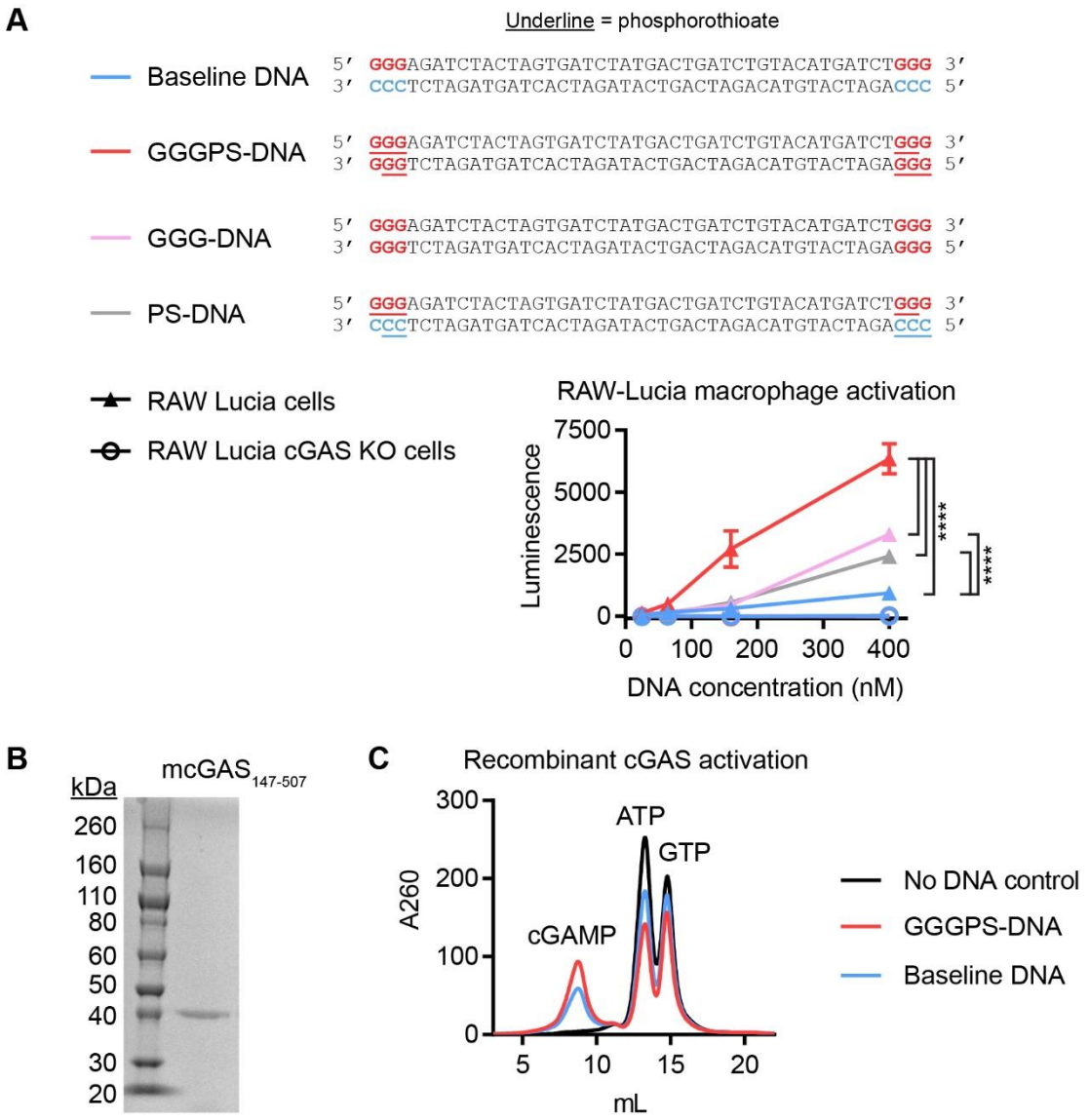

Figure 4-1: cGAS agonist characterization *in vitro*.
(**A**), RAW-Lucia ISG cells were activated with DNA complexed to Lipofectamine 2000. Triangles show the activity of the 4 DNAs tested in RAW-Lucia cells. Circles show minimal activity in cGAS KO RAW-Lucia cells for all 4 DNAs tested. Mean ± SD, $n = 3$. Some error bars are smaller than the symbol. Comparisons were made via two-way ANOVA using Tukey's multiple comparisons test, and statistics for the 400 nM condition are shown. ****, $P < 0.0001$. (**B**), Purified murine cGAS (amino acids 147-507) on a non-reducing SDS-PAGE gel with Coomassie blue stain. (**C**), Recombinant cGAS was incubated with DNA, ATP, GTP, and $MgCl_2$. The small molecules remaining after the reaction were assayed on a HiTrap Q HP column using a NaCl gradient.

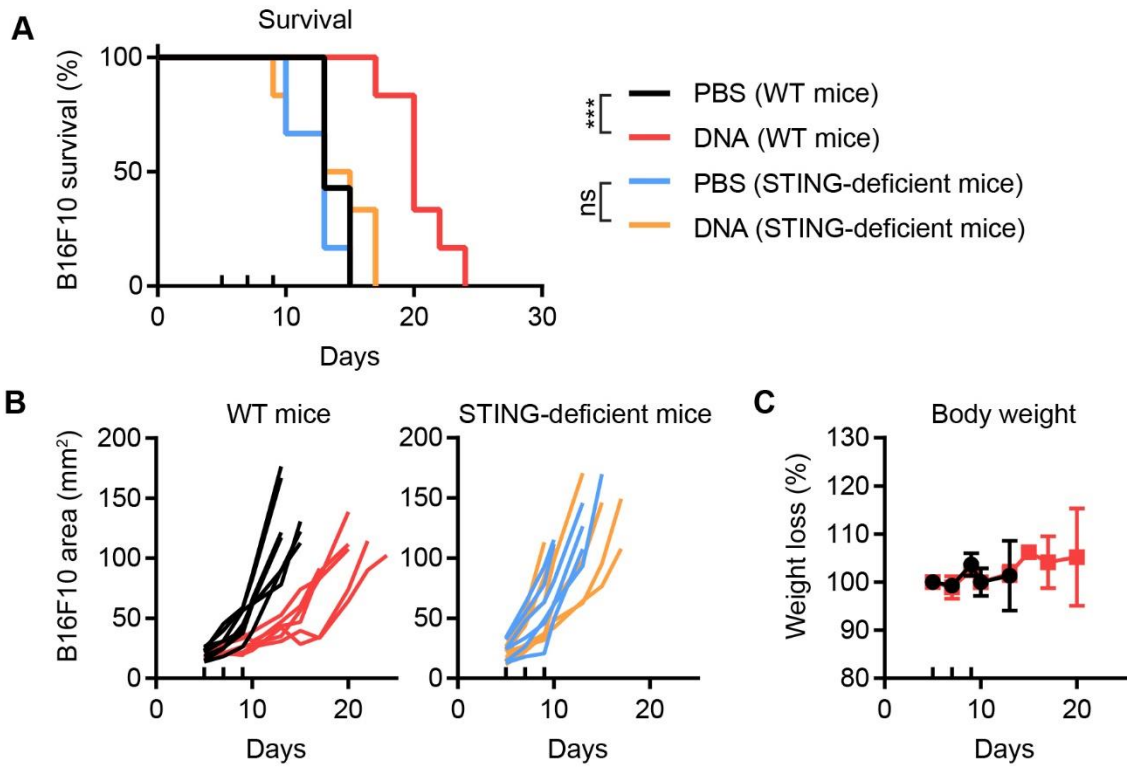

Figure 4-2: DNA-based cGAS agonists delay B16F10 tumor growth.
WT and STING-deficient mice were inoculated with 1 M B16F10 cells on day 0 and treated i.t. on days 5, 7, and 9 (ticks above x-axis) with PBS or 225 µg GGGPS-DNA. PBS-treated WT mice, *n* = 7. Other groups, *n* = 6. (**A**), Survival. Comparisons made by log-rank Mantel-Cox test. *** $P < 0.001$. (**B**), Tumor growth of individual mice. (**C**), Body weight loss normalized to day 5 weight; mean ± SD.

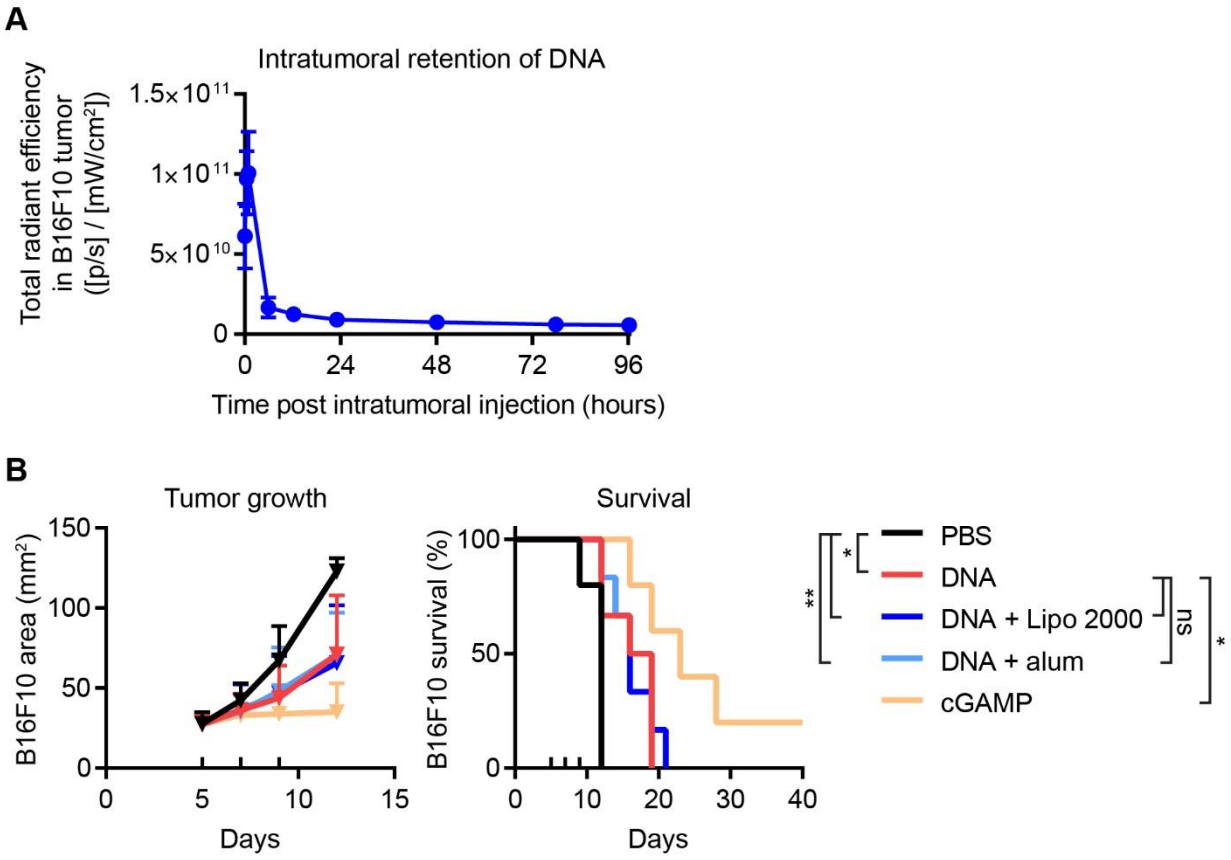

Figure 4-3: Challenges for DNA-based cGAS agonists.
(**A**), Mice bearing day 6 B16F10 Trp2KO tumors were injected i.t. with 24 μg AF647-labeled GGGPS-DNA. Total radiant efficiency at the tumor was tracked using *in vivo* imaging system (IVIS). Mean ± SD, $n = 3$. Representative experiment shown from 3 independent experiments. (**B**), Tumor area until day 12 (mean + SD) and survival of B16F10-bearing mice treated i.t. on days 5, 7, and 9 (ticks above x-axis) with PBS, 25 μg 2′3′-cGAMP, or 225 μg GGGPS-DNA. Some doses contained 12 μL Lipofectamine (Lipo) 2000 or 120 μg alum. PBS and cGAMP, $n = 5$. Other groups, $n = 6$. Survival compared by log-rank Mantel-Cox test. ns, not significant; * $P < 0.05$; ** $P < 0.01$.

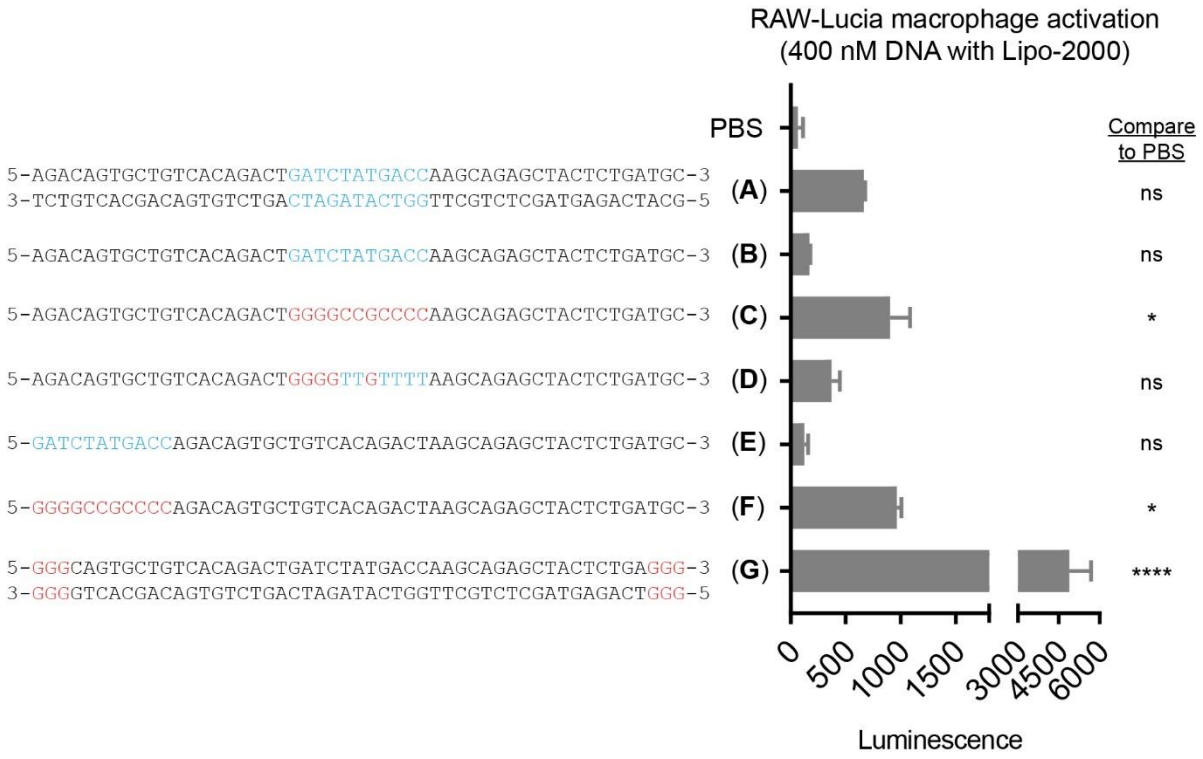

Figure 4-4: *In vitro* activity of GC-rich motif.
RAW-Lucia ISG cells were activated with PBS or 400 nM DNA complexed to Lipofectamine 2000. Mean ± SD, *n* = 3. (**A**) and (**G**) were double-stranded DNA, while (**B**), (**C**), (**D**), (**E**), and (**F**) were single-stranded DNA with the indicated sequences. The differences between oligonucleotide sequences are emphasized in blue and red text. Statistics: comparisons generated by one-way ANOVA with Tukey's multiple comparisons test. Showing statistics compared to PBS. ns, not significant; * $P < 0.05$; **** $P < 0.0001$.

Methods

Mice. C57BL/6 mice (Taconic C57BL/6NTac) were purchased. STING-deficient, Goldenticket mice (JAX 017537) were bred in-house. 6~8-week old female mice were used for experiments. All animal work was conducted under the approval of the Massachusetts Institute of Technology Committee on Animal Care in accordance with federal, state, and local guidelines.

Cells. B16F10 cells (ATCC), B16F10 Trp2KO cells (generated previously (*88*)), RAW-Lucia ISG cells (InvivoGen), and RAW-Lucia ISG-KO-cGAS cells (InvivoGen) were cultured in DMEM (ATCC) supplemented with 10% FBS. RAW-Lucia cell lines were maintained with 200 ug/mL Zeocin (InvivoGen) every other passage. Cells were cultured at 37 °C and 5% CO_2. All cell lines tested negative for mycoplasma.

DNA. DNA strands and aptamer libraries were purchased from Integrated DNA Technologies (IDT). To form dsDNA, complementary strands were annealed at 94 °C for 2 min, then cooled at 0.1 °C per second. DNA was stored at 4 °C.

Macrophage activation *in vitro*. 25 µL of 40 µM DNA was incubated with 25 µL Lipofectamine (Lipo) 2000 for 5 min at room temperature, followed by dilutions with PBS. RAW-Lucia ISG cells were seeded onto 96-well tissue culture plates at 100,000 cells per well and cultured in media with the DNA-Lipo mixtures. After 18 hours, luciferase levels in cell supernatants were assayed using QUANTI-Luc (InvivoGen) and a Tecan Infinite M200 Pro with an injector, following vendor instructions.

cGAS production. The catalytic domain of murine cGAS (amino acids 147-507) was cloned into the pE-SUMO vector (Life Sensors) and transformed into Rosetta 2 (DE3) *E. coli*. Rosetta cells were grown at 37 °C in LB broth with kanamycin and chloramphenicol until OD_{600} reached 0.7, induced by adding 1 mM IPTG, and incubated overnight at 20 °C. Cells were sonicated and H6-SUMO-cGAS was purified using TALON Metal Affinity Resin (Takara Bio). SUMO protease was added and incubated overnight at 4 °C. Protein was further purified on an ÄKTA FPLC using the Heparin HP ion-exchange column and a NaCl gradient. Protein was passed through fresh TALON resin to remove any cGAS that was not cleaved from H6-SUMO. cGAS was buffer exchanged into 20 mM HEPES-KOH pH 7.5, 250 mM KCl, 1 mM TCEP then flash frozen in liquid nitrogen. Molecular weight was confirmed by running cGAS alongside a pre-stained protein standard (Invitrogen) on a NuPage 4-12% Bis-Tris gel with Simply Blue Safe Stain (Life Technologies). For use in aptamer selections, cGAS was biotinylated using EZ-Link Sulfo-NHS-LC-Biotin reagent following vendor instructions.

cGAS activity assay. 0.2 µM cGAS, 200 µM ATP (Sigma), 200 µM GTP (Sigma), 4 µM DNA (IDT), and 10 mM $MgCl_2$ were incubated in 40 mM Tris-HCl, 100 mM NaCl, pH 7.5 for 2 hours at 37 °C. Reactions were terminated by heating at 95 °C for 3 min. cGAS and DNA were removed with a 10 kDa filter. Remaining small molecules were assayed on an ÄKTA FPLC using the HiTrap Q HP column in 50 mM Tris HCl, pH 8.5 and a gradient from 0 to 375 mM NaCl.

Tumor treatments and survival. On day 0, mice were inoculated subcutaneously (s.c.) with 1 M B16F10 cells in 50 µL PBS in the right flank. Mice were treated on days 5, 7, and 9, with all treatments administered intratumorally in a 20 µL volume. Mice were treated with PBS, 25 µg 2′3′-cGAMP (InvivoGen), or 225 µg GGGPS-DNA (IDT). To test delivery agents, 225 µg GGGPS-DNA was mixed with 12 µL Lipofectamine 2000 (Thermo Fisher) or 120 µg alum (Alhydrogel; InvivoGen vac-alu-250), and incubated at room temperature for at least 20 min prior to treatment. Mice were monitored for tumor area (length x width) and body weight. Mice were euthanized when tumors exceeded 100 mm^2 or mice exhibited poor body condition.

IVIS. On day 0, mice were inoculated with 1 M B16F10 Trp2KO cells (s.c.). Mice were fed alfalfa-free feed to minimize background fluorescence. GGGPS-DNA labeled with AF647 on the 5′ end was purchased from IDT. On day 6, AF647-DNA was injected i.t. (24 µg in 20 µL). Fluorescence at the tumor was imaged by IVIS (Perkin Elmer) using a 640 nm excitation filter and 680 nm emission filter. Image analysis was done by Living Image software.

Aptamer selections. A random aptamer library flanked by primers was purchased from IDT in the following format:
AGACAGTGCTGTCACAGACTG (N_{40}) CAAGCAGAGCTACTCTGATGC
Ten rounds of aptamer selections were performed. For each round, the aptamer library was prepared at 95 °C for 5 min, ice for 10 min, then RT for 15 min. Selections were performed in PBS, 0.8 mM $MgCl_2$, 0.05% Tween-20, 0.01% BSA, 1 mM TCEP, 1 mM DTT. Selections were performed using streptavidin magnetic beads, alternating each round with carboxylate modified beads (New England Biolabs S1420) and hydrophilic beads (New England Biolabs S1421). During negative selections, aptamers were incubated with magnetic beads alone for 10 min at RT. During positive selections, aptamers were incubated with biotinylated cGAS. With each round, selections became more stringent by lowering the concentration of cGAS and aptamers, increasing BSA from 0.01% to 0.03%, or adding an additional non-biotinylated, irrelevant protein competitor. After positive selections for 1 hour at RT, streptavidin magnetic beads were added, incubated for 5 min at RT, then applied to a magnet. Supernatant was discarded and beads were washed 3 times. Remaining aptamers were amplified using asymmetric PCR and gel purification for the next round of selections. Aptamers were cloned into the gWiz plasmid (Genlantis) and sequenced via Sanger sequencing.

Statistics. Statistics were performed with GraphPad Prism software V7. Survival was compared by log-rank Mantel-Cox text. Other comparisons were made via one-way or two-way analysis of variance (ANOVA) with Tukey's multiple comparisons test. The *n* and *P* values are indicated in captions.

Acknowledgments

Chapter 4 was performed under the guidance of Prof. K. Dane Wittrup. Thank you to Prof. Philip Kranzusch, Prof. Stefani Spranger, and Prof. Darrell Irvine for additional advice. I am grateful for support from many members of the Wittrup lab. Thank you especially to undergraduate researcher Vladlena Hornet and research assistant Janice Ong for their help with experiments on cGAS agonists.

We thank the Koch Institute's Robert A. Swanson (1969) Biotechnology Center (National Cancer Institute Grant P30-CA14051) for technical support, specifically the Preclinical Imaging and Testing facility. Thank you also to the MIT Division of Comparative Medicine. This work was supported in part by a MIT Skoltech Seed Grant. Personnel were supported by the NSF Graduate Research Fellowship Program, NIH/NIGMS Biotechnology Training Program, Siebel Scholar Award, and the Hope Babette Tang Student Research Fund, the Kristin R. Pressman and Jessica J. Pourian Koch Institute Fund, and the Charles S. Krakauer Fund (EAL).

Chapter 5. Conclusions and Outlook

This thesis is comprised of three projects, each addressing different considerations for intratumoral cytokine therapies. In chapter 2, we explore the benefits and nuances of intratumorally retaining type I interferon therapies. Alum-anchoring enabled high efficacy from type I IFNs, while maintaining safe tolerability in mice. Intratumoral administration and retention of type I IFNs are promising and warrant further study. Although our spatial constraint of IFN signaling was clearly advantageous, additional strategies to restrain the IFN pleiotropy observed within the tumor would likely further enhance this treatment. This project also highlighted how cytokine therapies can be too potent. In some contexts, the more potent tumor-retained IFNβ had inferior performance to its IFNα counterpart. In addition, tumor-retained type I IFNs combined with extended half-life IL-2 over-activated T-cells to an extent where memory response against the tumor was clearly dampened. Many methods have now emerged to increase cytokine potency, extend cytokine half-life, or prolong cytokine retention at the tumor. With these strategies readily available, it will be important to remember that for cytokines, “more” is not always “better”. A delicate balance is needed to fall between insufficient activation and over-stimulation of anti-tumor immunity.

In chapter 3, we tested the intratumoral administration of nanobody-IL-2 fusions, which are a relatively less-studied, small-format option for targeted cytokines. We find that small nanobody-IL-2 fusions had strong anti-tumor efficacy given both intratumoral administration and sufficient affinity to the tumor target. As one consideration for future research, the Wittrup lab previously found that intratumoral retention of proteins is extended not only by affinity to a target in the tumor microenvironment, but by high molecular weight (*31*). Thus, the small nanobody-IL-2 construct likely has weaker intratumoral retention than what is possible given the same targeting moiety used on a larger construct. However, the small nanobody-cytokine format has the potential benefit that once it eventually leaks out from the tumor, it will clear rapidly and may induce less systemic toxicity. For intratumorally administered and retained cytokines, it will be helpful to directly compare the toxicity and efficacy enabled by large molecular weight constructs (extra intratumoral retention) and small molecular weight constructs (rapid clearance from systemic circulation).

In chapter 4, we tested the possibility of using intratumorally-delivered DNA-based cGAS agonists to elicit productive type I IFN signaling. In our current iteration, DNA agonists were less efficacious than activating the pathway further downstream with CDN-based STING agonists, or with recombinant type I IFNs themselves. DNA-based cGAS agonists are still in the early stages of research (*148*, *149*), and further advances to the oligonucleotide stability, delivery, and activity will be necessary to continue making this approach more viable. It will also be important to take the tumor landscape into consideration, because cGAS-STING signaling can be defective in cancers (*152*, *153*), which would dampen the response to DNA or CDN therapies. Nevertheless, the immune system has evolved to transmit the danger signals of DNA or CDNs into productive, complex, downstream cytokine profiles. These cytokine profiles may have benefits compared to cytokine therapies where typically a single cytokine is administered at artificially high concentrations. Continuing to research innate immune pathways at multiple

intersection points will likely be useful to uncover optimal ways to elicit productive cytokine signaling.

As a whole, intratumoral cancer immunotherapies are advancing quickly. The number of clinical trials using intratumoral administration has rapidly increased, including both biologics and small molecule therapies (*30*). Many intratumoral administrations in the clinic have focused on easily accessible melanomas, but the technique is also being used for tumors in the colon, ovaries, breast, and bladder, among other anatomical locations (*28*). As this field continues to expand and gain accessibility, it is critical to first engineer strategies that enable different spatial and temporal signaling following intratumoral administration. It is next important to understand what spatial and temporal dynamics are most useful for a given drug, and rationally design therapies with those parameters. This thesis begins to address these questions for type I IFNs and IL-2 in murine tumor models. Applying and expanding on the lessons discussed here will help enable intratumoral cytokine therapies that can safely and effectively promote anti-tumor immunity for oncology patients.

References

1. D. S. Chen, I. Mellman, Oncology meets immunology: the cancer-immunity cycle. *Immunity*. **39**, 1–10 (2013).
2. A. D. Waldman, J. M. Fritz, M. J. Lenardo, A guide to cancer immunotherapy: from T cell basic science to clinical practice. *Nat. Rev. Immunol.* **20**, 651–668 (2020).
3. M. Saxena, S. H. van der Burg, C. J. M. Melief, N. Bhardwaj, Therapeutic cancer vaccines. *Nat. Rev. Cancer*. **21**, 360–378 (2021).
4. A. Ribas, J. D. Wolchok, Cancer immunotherapy using checkpoint blockade. *Science*. **359**, 1350–1355 (2018).
5. S. J. Schuster, M. R. Bishop, C. S. Tam, E. K. Waller, P. Borchmann, J. P. McGuirk, U. Jäger, S. Jaglowski, C. Andreadis, J. R. Westin, I. Fleury, V. Bachanova, S. R. Foley, P. J. Ho, S. Mielke, J. M. Magenau, H. Holte, S. Pantano, L. B. Pacaud, R. Awasthi, J. Chu, Ö. Anak, G. Salles, R. T. Maziarz, JULIET Investigators, Tisagenlecleucel in adult relapsed or refractory diffuse large B-cell lymphoma. *N. Engl. J. Med.* **380**, 45–56 (2019).
6. P. Berraondo, M. F. Sanmamed, M. C. Ochoa, I. Etxeberria, M. A. Aznar, J. L. Pérez-Gracia, M. E. Rodríguez-Ruiz, M. Ponz-Sarvise, E. Castañón, I. Melero, Cytokines in clinical cancer immunotherapy. *Br. J. Cancer*. **120**, 6–15 (2019).
7. J. R. Quesada, J. Reuben, J. T. Manning, E. M. Hersh, J. U. Gutterman, Alpha interferon for induction of remission in hairy-cell leukemia. *N. Engl. J. Med.* **310**, 15–18 (1984).
8. G. Fyfe, R. I. Fisher, S. A. Rosenberg, M. Sznol, D. R. Parkinson, A. C. Louie, Results of treatment of 255 patients with metastatic renal cell carcinoma who received high-dose recombinant interleukin-2 therapy. *J. Clin. Oncol.* **13**, 688–696 (1995).
9. M. B. Atkins, M. T. Lotze, J. P. Dutcher, R. I. Fisher, G. Weiss, K. Margolin, J. Abrams, M. Sznol, D. Parkinson, M. Hawkins, C. Paradise, L. Kunkel, S. A. Rosenberg, High-dose recombinant interleukin 2 therapy for patients with metastatic melanoma: analysis of 270 patients treated between 1985 and 1993. *J. Clin. Oncol.* **17**, 2105–2116 (1999).
10. P. G. Holder, S. A. Lim, C. S. Huang, P. Sharma, Y. S. Dagdas, B. Bulutoglu, J. T. Sockolosky, Engineering interferons and interleukins for cancer immunotherapy. *Adv. Drug Deliv. Rev.* **182**, 114112 (2022).
11. A. M. Eggermont, S. Suciu, M. Santinami, A. Testori, W. H. Kruit, J. Marsden, C. J. Punt, F. Salès, M. Gore, R. MacKie, Z. Kusic, R. Dummer, A. Hauschild, E. Musat, A. Spatz, U. Keilholz, EORTC Melanoma Group, Adjuvant therapy with pegylated interferon alfa-2b versus observation alone in resected stage III melanoma: final results of EORTC 18991, a randomised phase III trial. *Lancet*. **372**, 117–126 (2008).
12. T. M. Herndon, S. G. Demko, X. Jiang, K. He, J. E. Gootenberg, M. H. Cohen, P. Keegan, R. Pazdur, U.S. Food and Drug Administration Approval: peginterferon-alfa-2b for the adjuvant treatment of patients with melanoma. *Oncologist*. **17**, 1323–1328 (2012).
13. H.-Y. Tao, R.-Q. Wang, W.-J. Sheng, Y.-S. Zhen, The development of human serum albumin-based drugs and relevant fusion proteins for cancer therapy. *Int. J. Biol. Macromol.* **187**, 24–34 (2021).
14. G. M. Subramanian, M. Fiscella, A. Lamousé-Smith, S. Zeuzem, J. G. McHutchison, Albinterferon alpha-2b: a genetic fusion protein for the treatment of chronic hepatitis C. *Nat. Biotechnol.* **25**, 1411–1419 (2007).

15. C. Xuan, K. K. Steward, J. M. Timmerman, S. L. Morrison, Targeted delivery of interferon-alpha via fusion to anti-CD20 results in potent antitumor activity against B-cell lymphoma. *Blood*. **115**, 2864–2871 (2010).
16. Y. Liang, H. Tang, J. Guo, X. Qiu, Z. Yang, Z. Ren, Z. Sun, Y. Bian, L. Xu, H. Xu, J. Shen, Y. Han, H. Dong, H. Peng, Y.-X. Fu, Targeting IFNα to tumor by anti-PD-L1 creates feedforward antitumor responses to overcome checkpoint blockade resistance. *Nat. Commun.* **9**, 4586 (2018).
17. X. Yang, X. Zhang, M. L. Fu, R. R. Weichselbaum, T. F. Gajewski, Y. Guo, Y.-X. Fu, Targeting the tumor microenvironment with interferon-β bridges innate and adaptive immune responses. *Cancer Cell*. **25**, 37–48 (2014).
18. A. Tzeng, B. H. Kwan, C. F. Opel, T. Navaratna, K. D. Wittrup, Antigen specificity can be irrelevant to immunocytokine efficacy and biodistribution. *Proc. Natl. Acad. Sci. U. S. A.* **112**, 3320–3325 (2015).
19. P. Murer, D. Neri, Antibody-cytokine fusion proteins: A novel class of biopharmaceuticals for the therapy of cancer and of chronic inflammation. *N. Biotechnol.* **52**, 42–53 (2019).
20. G. Garcin, F. Paul, M. Staufenbiel, Y. Bordat, J. Van der Heyden, S. Wilmes, G. Cartron, F. Apparailly, S. De Koker, J. Piehler, J. Tavernier, G. Uzé, High efficiency cell-specific targeting of cytokine activity. *Nat. Commun.* **5**, 3016 (2014).
21. A. Cauwels, S. Van Lint, F. Paul, G. Garcin, S. De Koker, A. Van Parys, T. Wueest, S. Gerlo, J. Van der Heyden, Y. Bordat, D. Catteeuw, E. Rogge, A. Verhee, B. Vandekerckhove, N. Kley, G. Uzé, J. Tavernier, Delivering type I interferon to dendritic cells empowers tumor eradication and immune combination treatments. *Cancer Res.* **78**, 463–474 (2018).
22. X. Cao, Y. Liang, Z. Hu, H. Li, J. Yang, E. J. Hsu, J. Zhu, J. Zhou, Y.-X. Fu, Next generation of tumor-activating type I IFN enhances anti-tumor immune responses to overcome therapy resistance. *Nat. Commun.* **12**, 5866 (2021).
23. H. Wang, Y. Hou, Y. Hu, J. Dou, Y. Shen, Y. Wang, H. Lu, Enzyme-activatable interferon-poly(α-amino acid) conjugates for tumor microenvironment potentiation. *Biomacromolecules*. **20**, 3000–3008 (2019).
24. Z. Wang, J. Guo, J. Sun, P. Liang, Y. Wei, X. Deng, W. Gao, Thermoresponsive and protease-cleavable interferon-polypeptide conjugates with spatiotemporally programmed two-step release kinetics for tumor therapy. *Adv. Sci. (Weinh.)*. **6**, 1900586 (2019).
25. W. Winston, D. Hicklin, V. Bhaskar, L. Evnin, P. Baeuerle, J. A. Salmeron Garcia, H. Brodkin, Activatable Interleukin-2 Polypeptides And Methods Of Use Thereof. *US Patent* (2020).
26. A. Mansurov, A. Lauterbach, E. Budina, A. T. Alpar, J. A. Hubbell, J. Ishihara, Immunoengineering approaches for cytokine therapy. *Am. J. Physiol. Cell Physiol.* **321**, C369–C383 (2021).
27. A. W. Li, W. A. Lim, Engineering cytokines and cytokine circuits. *Science*. **370**, 1034–1035 (2020).
28. R. A. Sheth, R. Murthy, D. S. Hong, S. Patel, M. J. Overman, A. Diab, P. Hwu, A. Tam, Assessment of Image-Guided Intratumoral Delivery of Immunotherapeutics in Patients With Cancer. *JAMA Netw Open*. **3**, e207911–e207911 (2020).

29. R. H. I. Andtbacka, H. L. Kaufman, F. Collichio, T. Amatruda, N. Senzer, J. Chesney, K. A. Delman, L. E. Spitler, I. Puzanov, S. S. Agarwala, M. Milhem, L. Cranmer, B. Curti, K. Lewis, M. Ross, T. Guthrie, G. P. Linette, G. A. Daniels, K. Harrington, M. R. Middleton, W. H. Miller Jr, J. S. Zager, Y. Ye, B. Yao, A. Li, S. Doleman, A. VanderWalde, J. Gansert, R. S. Coffin, Talimogene laherparepvec improves durable response rate in patients with advanced melanoma. *J. Clin. Oncol.* **33**, 2780–2788 (2015).
30. S. Champiat, L. Tselikas, S. Farhane, T. Raoult, M. Texier, E. Lanoy, C. Massard, C. Robert, S. Ammari, T. De Baère, A. Marabelle, Intratumoral immunotherapy: From trial design to clinical practice. *Clin. Cancer Res.* **27**, 665–679 (2021).
31. N. Momin, J. R. Palmeri, E. A. Lutz, N. Jailkhani, H. Mak, A. Tabet, M. M. Chinn, B. H. Kang, V. Spanoudaki, R. O. Hynes, K. D. Wittrup, Maximizing response to intratumoral immunotherapy in mice by tuning local retention. *Nat. Commun.* **13**, 109 (2022).
32. N. Momin, N. K. Mehta, N. R. Bennett, L. Ma, J. R. Palmeri, M. M. Chinn, E. A. Lutz, B. Kang, D. J. Irvine, S. Spranger, K. D. Wittrup, Anchoring of intratumorally administered cytokines to collagen safely potentiates systemic cancer immunotherapy. *Sci. Transl. Med.* **11** (2019), doi:10.1126/scitranslmed.aaw2614.
33. R. Danielli, R. Patuzzo, A. M. Di Giacomo, G. Gallino, A. Maurichi, A. Di Florio, O. Cutaia, A. Lazzeri, C. Fazio, C. Miracco, L. Giovannoni, G. Elia, D. Neri, M. Maio, M. Santinami, Intralesional administration of L19-IL2/L19-TNF in stage III or stage IVM1a melanoma patients: results of a phase II study. *Cancer Immunol. Immunother.* **64**, 999–1009 (2015).
34. B. Weide, T. K. Eigentler, A. Pflugfelder, H. Zelba, A. Martens, G. Pawelec, L. Giovannoni, P. A. Ruffini, G. Elia, D. Neri, R. Gutzmer, J. C. Becker, C. Garbe, Intralesional treatment of stage III metastatic melanoma patients with L19-IL2 results in sustained clinical and systemic immunologic responses. *Cancer Immunol. Res.* **2**, 668–678 (2014).
35. R. K. Yang, N. A. Kalogriopoulos, A. L. Rakhmilevich, E. A. Ranheim, S. Seo, K. Kim, K. L. Alderson, J. Gan, R. A. Reisfeld, S. D. Gillies, J. A. Hank, P. M. Sondel, Intratumoral hu14.18-IL-2 (IC) induces local and systemic antitumor effects that involve both activated T and NK cells as well as enhanced IC retention. *J. Immunol.* **189**, 2656–2664 (2012).
36. E. E. Johnson, H. D. Lum, A. L. Rakhmilevich, B. E. Schmidt, M. Furlong, I. N. Buhtoiarov, J. A. Hank, A. Raubitschek, D. Colcher, R. A. Reisfeld, S. D. Gillies, P. M. Sondel, Intratumoral immunocytokine treatment results in enhanced antitumor effects. *Cancer Immunol. Immunother.* **57**, 1891–1902 (2008).
37. T. J. Aiken, D. Komjathy, M. Rodriguez, A. Stuckwisch, A. Feils, V. Subbotin, J. Birstler, S. D. Gillies, A. L. Rakhmilevich, A. K. Erbe, P. M. Sondel, Short-course neoadjuvant in situ vaccination for murine melanoma. *J. Immunother. Cancer*. **10**, e003586 (2022).
38. Y. Agarwal, L. E. Milling, J. Y. H. Chang, L. Santollani, A. Sheen, E. A. Lutz, A. Tabet, J. Stinson, K. Ni, K. A. Rodrigues, T. J. Moyer, M. B. Melo, D. J. Irvine, K. D. Wittrup, Intratumourally injected alum-tethered cytokines elicit potent and safer local and systemic anticancer immunity. *Nat Biomed Eng* (2022), doi:10.1038/s41551-021-00831-9.
39. G. W. Bos, J. J. L. Jacobs, J. W. Koten, S. Van Tomme, T. Veldhuis, C. F. van Nostrum, W. Den Otter, W. E. Hennink, In situ crosslinked biodegradable hydrogels loaded with IL-2 are effective tools for local IL-2 therapy. *Eur. J. Pharm. Sci.* **21**, 561–567 (2004).
40. Y. Hori, P. J. Stern, R. O. Hynes, D. J. Irvine, Engulfing tumors with synthetic extracellular matrices for cancer immunotherapy. *Biomaterials*. **30**, 6757–6767 (2009).

41. D. A. Zaharoff, K. W. Hance, C. J. Rogers, J. Schlom, J. W. Greiner, Intratumoral immunotherapy of established solid tumors with chitosan/IL-12. *J. Immunother.* **33**, 697–705 (2010).
42. M. B. Fuertes, A. K. Kacha, J. Kline, S.-R. Woo, D. M. Kranz, K. M. Murphy, T. F. Gajewski, Host type I IFN signals are required for antitumor CD8+ T cell responses through CD8{alpha}+ dendritic cells. *J. Exp. Med.* **208**, 2005–2016 (2011).
43. M. S. Diamond, M. Kinder, H. Matsushita, M. Mashayekhi, G. P. Dunn, J. M. Archambault, H. Lee, C. D. Arthur, J. M. White, U. Kalinke, K. M. Murphy, R. D. Schreiber, Type I interferon is selectively required by dendritic cells for immune rejection of tumors. *J. Exp. Med.* **208**, 1989–2003 (2011).
44. L. Corrales, V. Matson, B. Flood, S. Spranger, T. F. Gajewski, Innate immune signaling and regulation in cancer immunotherapy. *Cell Res.* **27**, 96–108 (2017).
45. E. C. Borden, Interferons α and β in cancer: therapeutic opportunities from new insights. *Nat. Rev. Drug Discov.* **18**, 219–234 (2019).
46. M. Musella, G. Manic, R. De Maria, I. Vitale, A. Sistigu, Type-I-interferons in infection and cancer: Unanticipated dynamics with therapeutic implications. *Oncoimmunology*. **6**, e1314424 (2017).
47. R. M. Spaapen, M. Y. K. Leung, M. B. Fuertes, J. P. Kline, L. Zhang, Y. Zheng, Y.-X. Fu, X. Luo, K. S. Cohen, T. F. Gajewski, Therapeutic activity of high-dose intratumoral IFN-β requires direct effect on the tumor vasculature. *J. Immunol.* **193**, 4254–4260 (2014).
48. C. Rozera, D. Carlei, P. L. Lollini, C. De Giovanni, P. Musiani, E. Di Carlo, F. Belardelli, M. Ferrantini, Interferon (IFN)-β gene transfer into TS/A adenocarcinoma cells and comparison with IFN-α. *Am. J. Pathol.* **154**, 1211–1222 (1999).
49. M. Ohashi, K. Yoshida, M. Kushida, Y. Miura, S. Ohnami, Y. Ikarashi, Y. Kitade, T. Yoshida, K. Aoki, Adenovirus-mediated interferon alpha gene transfer induces regional direct cytotoxicity and possible systemic immunity against pancreatic cancer. *Br. J. Cancer*. **93**, 441–449 (2005).
50. K. Narumi, A. Kondoh, T. Udagawa, H. Hara, N. Goto, Y. Ikarashi, S. Ohnami, T. Okada, M. Yamagishi, T. Yoshida, K. Aoki, Administration route-dependent induction of antitumor immunity by interferon-alpha gene transfer. *Cancer Sci.* **101**, 1686–1694 (2010).
51. N. Jacquelot, T. Yamazaki, M. P. Roberti, C. P. M. Duong, M. C. Andrews, L. Verlingue, G. Ferrere, S. Becharef, M. Vétizou, R. Daillère, M. Messaoudene, D. P. Enot, G. Stoll, S. Ugel, I. Marigo, S. Foong Ngiow, A. Marabelle, A. Prevost-Blondel, P.-O. Gaudreau, V. Gopalakrishnan, A. M. Eggermont, P. Opolon, C. Klein, G. Madonna, P. A. Ascierto, A. Sucker, D. Schadendorf, M. J. Smyth, J.-C. Soria, G. Kroemer, V. Bronte, J. Wargo, L. Zitvogel, Sustained Type I interferon signaling as a mechanism of resistance to PD-1 blockade. *Cell Res.* **29**, 846–861 (2019).
52. J. L. Benci, B. Xu, Y. Qiu, T. J. Wu, H. Dada, C. Twyman-Saint Victor, L. Cucolo, D. S. M. Lee, K. E. Pauken, A. C. Huang, T. C. Gangadhar, R. K. Amaravadi, L. M. Schuchter, M. D. Feldman, H. Ishwaran, R. H. Vonderheide, A. Maity, E. J. Wherry, A. J. Minn, Tumor interferon signaling regulates a multigenic resistance program to immune checkpoint blockade. *Cell*. **167**, 1540-1554.e12 (2016).
53. J. L. Benci, L. R. Johnson, R. Choa, Y. Xu, J. Qiu, Z. Zhou, B. Xu, D. Ye, K. L. Nathanson, C. H. June, E. J. Wherry, N. R. Zhang, H. Ishwaran, M. D. Hellmann, J. D. Wolchok, T.

Kambayashi, A. J. Minn, Opposing functions of interferon coordinate adaptive and innate immune responses to cancer immune checkpoint blockade. *Cell*. **178**, 933-948.e14 (2019).
54. G. Schreiber, J. Piehler, The molecular basis for functional plasticity in type I interferon signaling. *Trends Immunol.* **36**, 139–149 (2015).
55. L. E. Fox, M. C. Locke, D. J. Lenschow, Context is key: Delineating the unique functions of IFNα and IFNβ in disease. *Front. Immunol.* **11**, 606874 (2020).
56. C. Thomas, I. Moraga, D. Levin, P. O. Krutzik, Y. Podoplelova, A. Trejo, C. Lee, G. Yarden, S. E. Vleck, J. S. Glenn, G. P. Nolan, J. Piehler, G. Schreiber, K. C. Garcia, Structural linkage between ligand discrimination and receptor activation by type I interferons. *Cell*. **146**, 621–632 (2011).
57. V. van Pesch, H. Lanaya, J.-C. Renauld, T. Michiels, Characterization of the murine alpha interferon gene family. *J. Virol.* **78**, 8219–8228 (2004).
58. G. L. Morefield, D. Jiang, I. Z. Romero-Mendez, R. L. Geahlen, H. Hogenesch, S. L. Hem, Effect of phosphorylation of ovalbumin on adsorption by aluminum-containing adjuvants and elution upon exposure to interstitial fluid. *Vaccine*. **23**, 1502–1506 (2005).
59. T. J. Moyer, Y. Kato, W. Abraham, J. Y. H. Chang, D. W. Kulp, N. Watson, H. L. Turner, S. Menis, R. K. Abbott, J. N. Bhiman, M. B. Melo, H. A. Simon, S. Herrera-De la Mata, S. Liang, G. Seumois, Y. Agarwal, N. Li, D. R. Burton, A. B. Ward, W. R. Schief, S. Crotty, D. J. Irvine, Engineered immunogen binding to alum adjuvant enhances humoral immunity. *Nat. Med.* **26**, 430–440 (2020).
60. F. Vignaux, I. Gresser, Differential effects of interferon on the expression of H-2K, H-2D, and Ia antigens on mouse lymphocytes. *J. Immunol.* **118**, 721–723 (1977).
61. S. C. Eisenbarth, O. R. Colegio, W. O'Connor, F. S. Sutterwala, R. A. Flavell, Crucial role for the Nalp3 inflammasome in the immunostimulatory properties of aluminium adjuvants. *Nature*. **453**, 1122–1126 (2008).
62. E. F. Zhu, S. A. Gai, C. F. Opel, B. H. Kwan, R. Surana, M. C. Mihm, M. J. Kauke, K. D. Moynihan, A. Angelini, R. T. Williams, M. T. Stephan, J. S. Kim, M. B. Yaffe, D. J. Irvine, L. M. Weiner, G. Dranoff, K. D. Wittrup, Synergistic innate and adaptive immune response to combination immunotherapy with anti-tumor antigen antibodies and extended serum half-life IL-2. *Cancer Cell*. **27**, 489–501 (2015).
63. A. Tzeng, M. J. Kauke, E. F. Zhu, K. D. Moynihan, C. F. Opel, N. J. Yang, N. Mehta, R. L. Kelly, G. L. Szeto, W. W. Overwijk, D. J. Irvine, K. D. Wittrup, Temporally programmed CD8α + DC activation enhances combination cancer immunotherapy. *Cell Rep.* **17**, 2503–2511 (2016).
64. A. M. Rothschilds, K. D. Wittrup, What, why, where, and when: Bringing timing to immuno-oncology. *Trends Immunol.* **40**, 12–21 (2019).
65. M. B. Atkins, J. Sparano, R. I. Fisher, G. R. Weiss, K. A. Margolin, K. I. Fink, L. Rubinstein, A. Louie, J. W. Mier, R. Gucalp, Randomized phase II trial of high-dose interleukin-2 either alone or in combination with interferon alfa-2b in advanced renal cell carcinoma. *J. Clin. Oncol.* **11**, 661–670 (1993).
66. D. F. McDermott, M. M. Regan, J. I. Clark, L. E. Flaherty, G. R. Weiss, T. F. Logan, J. M. Kirkwood, M. S. Gordon, J. A. Sosman, M. S. Ernstoff, C. P. G. Tretter, W. J. Urba, J. W. Smith, K. A. Margolin, J. W. Mier, J. A. Gollob, J. P. Dutcher, M. B. Atkins, Randomized

phase III trial of high-dose interleukin-2 versus subcutaneous interleukin-2 and interferon in patients with metastatic renal cell carcinoma. *J. Clin. Oncol.* **23**, 133–141 (2005).
67. S. Negrier, B. Escudier, C. Lasset, J. Y. Douillard, J. Savary, C. Chevreau, A. Ravaud, A. Mercatello, J. Peny, M. Mousseau, T. Philip, T. Tursz, Recombinant human interleukin-2, recombinant human interferon alfa-2a, or both in metastatic renal-cell carcinoma. Groupe Français d'Immunothérapie. *N. Engl. J. Med.* **338**, 1272–1278 (1998).
68. A. Rothschilds, A. Tzeng, N. K. Mehta, K. D. Moynihan, D. J. Irvine, K. D. Wittrup, Order of administration of combination cytokine therapies can decouple toxicity from efficacy in syngeneic mouse tumor models. *Oncoimmunology*. **8**, e1558678 (2019).
69. S. A. Rosenberg, J. C. Yang, D. J. Schwartzentruber, P. Hwu, F. M. Marincola, S. L. Topalian, C. A. Seipp, J. H. Einhorn, D. E. White, S. M. Steinberg, Prospective randomized trial of the treatment of patients with metastatic melanoma using chemotherapy with cisplatin, dacarbazine, and tamoxifen alone or in combination with interleukin-2 and interferon alfa-2b. *J. Clin. Oncol.* **17**, 968–975 (1999).
70. A. Amouzegar, M. Chelvanambi, J. N. Filderman, W. J. Storkus, J. J. Luke, STING agonists as cancer therapeutics. *Cancers (Basel)*. **13**, 2695 (2021).
71. Y. Zhu, M. Chen, D. Xu, T.-E. Li, Z. Zhang, J.-H. Li, X.-Y. Wang, X. Yang, L. Lu, H.-L. Jia, Q.-Z. Dong, L.-X. Qin, The combination of PD-1 blockade with interferon-α has a synergistic effect on hepatocellular carcinoma. *Cell. Mol. Immunol.* (2022), doi:10.1038/s41423-022-00848-3.
72. S. M. Kaech, J. T. Tan, E. J. Wherry, B. T. Konieczny, C. D. Surh, R. Ahmed, Selective expression of the interleukin 7 receptor identifies effector CD8 T cells that give rise to long-lived memory cells. *Nat. Immunol.* **4**, 1191–1198 (2003).
73. N. S. Joshi, W. Cui, A. Chandele, H. K. Lee, D. R. Urso, J. Hagman, L. Gapin, S. M. Kaech, Inflammation directs memory precursor and short-lived effector CD8(+) T cell fates via the graded expression of T-bet transcription factor. *Immunity*. **27**, 281–295 (2007).
74. N. S. Joshi, S. M. Kaech, Effector CD8 T cell development: a balancing act between memory cell potential and terminal differentiation. *J. Immunol.* **180**, 1309–1315 (2008).
75. F. Baharom, R. A. Ramirez-Valdez, K. K. S. Tobin, H. Yamane, C.-A. Dutertre, A. Khalilnezhad, G. V. Reynoso, V. L. Coble, G. M. Lynn, M. P. Mulè, A. J. Martins, J. P. Finnigan, X. M. Zhang, J. A. Hamerman, N. Bhardwaj, J. S. Tsang, H. D. Hickman, F. Ginhoux, A. S. Ishizuka, R. A. Seder, Intravenous nanoparticle vaccination generates stem-like TCF1+ neoantigen-specific CD8+ T cells. *Nat. Immunol.* **22**, 41–52 (2021).
76. L. K. Selin, M. A. Brehm, Y. N. Naumov, M. Cornberg, S.-K. Kim, S. C. Clute, R. M. Welsh, Memory of mice and men: CD8+ T-cell cross-reactivity and heterologous immunity. *Immunol. Rev.* **211**, 164–181 (2006).
77. V. Kalia, S. Sarkar, S. Subramaniam, W. N. Haining, K. A. Smith, R. Ahmed, Prolonged interleukin-2Ralpha expression on virus-specific CD8+ T cells favors terminal-effector differentiation in vivo. *Immunity*. **32**, 91–103 (2010).
78. K. Xu, F. Lee, S. J. Gao, J. E. Chung, H. Yano, M. Kurisawa, Injectable hyaluronic acid-tyramine hydrogels incorporating interferon-α2a for liver cancer therapy. *J. Control. Release*. **166**, 203–210 (2013).
79. K. Ueda, J. Akiba, S. Ogasawara, K. Todoroki, M. Nakayama, A. Sumi, H. Kusano, S. Sanada, S. Suekane, K. Xu, K. H. Bae, M. Kurisawa, T. Igawa, H. Yano, Growth inhibitory

effect of an injectable hyaluronic acid-tyramine hydrogels incorporating human natural interferon-α and sorafenib on renal cell carcinoma cells. *Acta Biomater.* **29**, 103–111 (2016).
80. J.-G. Hu, J.-K. Pi, Y.-L. Jiang, X.-F. Liu, J. Li-Ling, H.-Q. Xie, Collagen hydrogel functionalized with collagen-targeting IFNA2b shows apoptotic activity in nude mice with xenografted tumors. *ACS Biomater. Sci. Eng.* **5**, 272–282 (2019).
81. Q. Liu, D. Zhang, H. Qian, Y. Chu, Y. Yang, J. Shao, Q. Xu, B. Liu, Superior antitumor efficacy of IFN-α2b-incorporated photo-cross-linked hydrogels combined with T cell transfer and low-dose irradiation against gastric cancer. *Int. J. Nanomedicine*. **15**, 3669–3680 (2020).
82. M. Buttmann, F. Berberich-Siebelt, E. Serfling, P. Rieckmann, Interferon-beta is a potent inducer of interferon regulatory factor-1/2-dependent IP-10/CXCL10 expression in primary human endothelial cells. *J. Vasc. Res.* **44**, 51–60 (2007).
83. R. M. Strieter, J. A. Belperio, R. J. Phillips, M. P. Keane, CXC chemokines in angiogenesis of cancer. *Semin. Cancer Biol.* **14**, 195–200 (2004).
84. S. I. S. Mosely, J. E. Prime, R. C. A. Sainson, J.-O. Koopmann, D. Y. Q. Wang, D. M. Greenawalt, M. J. Ahdesmaki, R. Leyland, S. Mullins, L. Pacelli, D. Marcus, J. Anderton, A. Watkins, J. Coates Ulrichsen, P. Brohawn, B. W. Higgs, M. McCourt, H. Jones, J. A. Harper, M. Morrow, V. Valge-Archer, R. Stewart, S. J. Dovedi, R. W. Wilkinson, Rational selection of syngeneic preclinical tumor models for immunotherapeutic drug discovery. *Cancer Immunol. Res.* **5**, 29–41 (2017).
85. E. Duong, T. B. Fessenden, E. Lutz, T. Dinter, L. Yim, S. Blatt, A. Bhutkar, K. D. Wittrup, S. Spranger, Type I interferon activates MHC class I-dressed CD11b+ conventional dendritic cells to promote protective anti-tumor CD8+ T cell immunity. *Immunity*. **55**, 308-323.e9 (2022).
86. M. G. Lechner, S. S. Karimi, K. Barry-Holson, T. E. Angell, K. A. Murphy, C. H. Church, J. R. Ohlfest, P. Hu, A. L. Epstein, Immunogenicity of murine solid tumor models as a defining feature of in vivo behavior and response to immunotherapy. *J. Immunother.* **36**, 477–489 (2013).
87. M. Wiesel, J. Crouse, G. Bedenikovic, A. Sutherland, N. Joller, A. Oxenius, Type-I IFN drives the differentiation of short-lived effector CD8+ T cells in vivo. *Eur. J. Immunol.* **42**, 320–329 (2012).
88. K. D. Moynihan, C. F. Opel, G. L. Szeto, A. Tzeng, E. F. Zhu, J. M. Engreitz, R. T. Williams, K. Rakhra, M. H. Zhang, A. M. Rothschilds, S. Kumari, R. L. Kelly, B. H. Kwan, W. Abraham, K. Hu, N. K. Mehta, M. J. Kauke, H. Suh, J. R. Cochran, D. A. Lauffenburger, K. D. Wittrup, D. J. Irvine, Eradication of large established tumors in mice by combination immunotherapy that engages innate and adaptive immune responses. *Nat. Med.* **22**, 1402–1410 (2016).
89. S. C. Liang, Y. E. Latchman, J. E. Buhlmann, M. F. Tomczak, B. H. Horwitz, G. J. Freeman, A. H. Sharpe, Regulation of PD-1, PD-L1, and PD-L2 expression during normal and autoimmune responses. *Eur. J. Immunol.* **33**, 2706–2716 (2003).
90. M. Lo, H. S. Kim, R. K. Tong, T. W. Bainbridge, J.-M. Vernes, Y. Zhang, Y. L. Lin, S. Chung, M. S. Dennis, Y. J. Y. Zuchero, R. J. Watts, J. A. Couch, Y. G. Meng, J. K. Atwal,

R. J. Brezski, C. Spiess, J. A. Ernst, Effector-attenuating substitutions that maintain antibody stability and reduce toxicity in mice. *J. Biol. Chem.* **292**, 3900–3908 (2017).
91. S. A. Rosenberg, M. T. Lotze, J. C. Yang, P. M. Aebersold, W. Marston Linehan, C. A. Seipp, D. E. White., Experience with the Use of High-Dose Interleukin-2 in the Treatment of 652 Cancer Patients. *Ann. Surg.* **210**, 474–485 (1989).
92. A. Tang, F. Harding, The challenges and molecular approaches surrounding interleukin-2-based therapeutics in cancer. *Cytokine: X*. **1**, 100001 (2019).
93. J. E. Schwarzbauer, R. S. Patel, D. Fonda, R. O. Hynes, Multiple sites of alternative splicing of the rat fibronectin gene transcript. *EMBO J.* **6**, 2573–2580 (1987).
94. B. Carnemolla, L. Borsi, E. Balza, P. Castellani, R. Meazza, A. Berndt, S. Ferrini, H. Kosmehl, D. Neri, L. Zardi, Enhancement of the antitumor properties of interleukin-2 by its targeted delivery to the tumor blood vessel extracellular matrix. *Blood*. **99**, 1659–1665 (2002).
95. D. Neri, R. Bicknell, Tumour vascular targeting. *Nat. Rev. Cancer*. **5**, 436–446 (2005).
96. N. Jailkhani, J. R. Ingram, M. Rashidian, S. Rickelt, C. Tian, H. Mak, Z. Jiang, H. L. Ploegh, R. O. Hynes, Noninvasive imaging of tumor progression, metastasis, and fibrosis using a nanobody targeting the extracellular matrix. *Proc. Natl. Acad. Sci. U. S. A.* **116**, 14181–14190 (2019).
97. Y. J. Xie, M. Dougan, N. Jailkhani, J. Ingram, T. Fang, L. Kummer, N. Momin, N. Pishesha, S. Rickelt, R. O. Hynes, H. Ploegh, Nanobody-based CAR T cells that target the tumor microenvironment inhibit the growth of solid tumors in immunocompetent mice. *Proc. Natl. Acad. Sci. U. S. A.* **116**, 7624–7631 (2019).
98. G. Chao, W. L. Lau, B. J. Hackel, S. L. Sazinsky, S. M. Lippow, K. D. Wittrup, Isolating and engineering human antibodies using yeast surface display. *Nat. Protoc.* **1**, 755–768 (2006).
99. J. Dunbar, K. Krawczyk, J. Leem, C. Marks, J. Nowak, C. Regep, G. Georges, S. Kelm, B. Popovic, C. M. Deane, SAbPred: a structure-based antibody prediction server. *Nucleic Acids Res.* **44**, W474-8 (2016).
100. J. Leem, J. Dunbar, G. Georges, J. Shi, C. M. Deane, ABodyBuilder: Automated antibody structure prediction with data-driven accuracy estimation. *MAbs*. **8**, 1259–1268 (2016).
101. E. F. Pettersen, T. D. Goddard, C. C. Huang, G. S. Couch, D. M. Greenblatt, E. C. Meng, T. E. Ferrin, UCSF Chimera--a visualization system for exploratory research and analysis. *J. Comput. Chem.* **25**, 1605–1612 (2004).
102. R. Vazquez-Lombardi, C. Loetsch, D. Zinkl, J. Jackson, P. Schofield, E. K. Deenick, C. King, T. G. Phan, K. E. Webster, J. Sprent, D. Christ, Potent antitumour activity of interleukin-2-Fc fusion proteins requires Fc-mediated depletion of regulatory T-cells. *Nat. Commun.* **8**, 15373 (2017).
103. D. V. Liu, L. M. Maier, D. A. Hafler, K. D. Wittrup, Engineered interleukin-2 antagonists for the inhibition of regulatory T cells. *J. Immunother.* **32**, 887–894 (2009).
104. Y. Li, Z. Su, W. Zhao, X. Zhang, N. Momin, C. Zhang, K. D. Wittrup, Y. Dong, D. J. Irvine, R. Weiss, Multifunctional oncolytic nanoparticles deliver self-replicating IL-12 RNA to eliminate established tumors and prime systemic immunity. *Nat Cancer*. **1**, 882–893 (2020).

105. M. Dougan, J. R. Ingram, H.-J. Jeong, M. M. Mosaheb, P. T. Bruck, L. Ali, N. Pishesha, O. Blomberg, P. M. Tyler, M. M. Servos, M. Rashidian, Q.-D. Nguyen, U. H. von Andrian, H. L. Ploegh, S. K. Dougan, Targeting Cytokine Therapy to the Pancreatic Tumor Microenvironment Using PD-L1–Specific VHHs. *Cancer Immunol Res*. **6**, 389–401 (2018).
106. M. M. Schmidt, K. D. Wittrup, A modeling analysis of the effects of molecular size and binding affinity on tumor targeting. *Mol. Cancer Ther.* **8**, 2861–2871 (2009).
107. C. M. L. Zegers, N. H. Rekers, D. H. F. Quaden, N. G. Lieuwes, A. Yaromina, W. T. V. Germeraad, L. Wieten, E. A. L. Biessen, L. Boon, D. Neri, E. G. C. Troost, L. J. Dubois, P. Lambin, Radiotherapy combined with the immunocytokine L19-IL2 provides long-lasting antitumor effects. *Clin. Cancer Res.* **21**, 1151–1160 (2015).
108. E. Balza, B. Carnemolla, L. Mortara, P. Castellani, D. Soncini, R. S. Accolla, L. Borsi, Therapy-induced antitumor vaccination in neuroblastomas by the combined targeting of IL-2 and TNFalpha. *Int. J. Cancer*. **127**, 101–110 (2010).
109. W. W. Overwijk, M. A. Tagliaferri, J. Zalevsky, Engineering IL-2 to Give New Life to T Cell Immunotherapy. *Annu. Rev. Med.* **72**, 281–311 (2021).
110. I. S. Pires, P. T. Hammond, D. J. Irvine, Engineering strategies for immunomodulatory cytokine therapies - challenges and clinical progress. *Adv. Ther.* **4**, 2100035 (2021).
111. J. L. Perez-Gracia, A. R. Hansen, R. H. L. Eefsen, C. A. Gomez-Roca, S. Negrier, P. Pedrazzoli, J.-L. Lee, T. Alonso Gordoa, C. Suarez Rodriguez, B. Mellado, V. Moreno, A. Rodriguez-Vida, A. Hussain, N. Getzmann, D. Dejardin, C. Boetsch, A. Kraxner, T. Vardar, V. Teichgräber, T. Powles, Randomized phase Ib study to evaluate safety, pharmacokinetics and therapeutic activity of simlukafusp α in combination with atezolizumab ± bevacizumab in patients with unresectable advanced/ metastatic renal cell carcinoma (RCC) (NCT03063762). *J. Clin. Oncol.* **39**, 4556–4556 (2021).
112. E. M. J. van Brummelen, M. C. Huisman, L. J. de Wit-van der Veen, T. K. Nayak, M. P. M. Stokkel, E. R. Mulder, O. S. Hoekstra, D. J. Vugts, G. A. M. S. Van Dongen, H. M. Verheul, S. Evers, J. J. L. Tessier, J. Saro, J. H. M. Schellens, C. W. Menke-van der Houven van Oordt, 89Zr-labeled CEA-targeted IL-2 variant immunocytokine in patients with solid tumors: CEA-mediated tumor accumulation and role of IL-2 receptor-binding. *Oncotarget*. **9**, 24737–24749 (2018).
113. P. Umaña, L. C. Deak, M. Hashimoto, R. Ahmed, C. Klein, V. Nicolini, L. Lauener, M. Karagianni, M. Richard, E. Bommer, Others, Differentiating PD-1+ stem-like CD8 T cells towards distinct effectors with enhanced therapeutic potential by an engineered IL-2 cis-targeted to PD-1 (2021) (available at https://europepmc.org/article/ppr/ppr297911).
114. Y. Xu, L. C. Carrascosa, Y. A. Yeung, M. L.-H. Chu, W. Yang, I. Djuretic, D. C. Pappas, J. Zeytounian, Z. Ge, V. de Ruiter, G. R. Starbeck-Miller, J. Patterson, D. Rigas, S.-H. Chen, E. Kraynov, P. P. Boor, L. Noordam, M. Doukas, D. Tsao, J. N. Ijzermans, J. Guo, D. J. Grünhagen, J. Erdmann, J. Verheij, M. E. van Royen, P. G. Doornebosch, R. Feldman, T. Park, S. Mahmoudi, M. Dorywalska, I. Ni, S. M. Chin, T. Mistry, L. Mosyak, L. Lin, K. A. Ching, K. C. Lindquist, C. Ji, L. M. Londono, B. Kuang, R. Rickert, J. Kwekkeboom, D. Sprengers, T.-H. Huang, J. Chaparro-Riggers, An Engineered IL15 Cytokine Mutein Fused to an Anti-PD1 Improves Intratumoral T-cell Function and Antitumor Immunity. *Cancer Immunol Res*. **9**, 1141–1157 (2021).

115. C. C. Baniel, E. G. Sumiec, J. A. Hank, A. M. Bates, A. K. Erbe, A. A. Pieper, A. G. Hoefges, R. B. Patel, A. L. Rakhmilevich, Z. S. Morris, P. M. Sondel, Intratumoral injection reduces toxicity and antibody-mediated neutralization of immunocytokine in a mouse melanoma model. *J. Immunother. Cancer*. **8**, e001262 (2020).
116. B. Weide, E. Derhovanessian, A. Pflugfelder, T. K. Eigentler, P. Radny, H. Zelba, C. Pföhler, G. Pawelec, C. Garbe, High response rate after intratumoral treatment with interleukin-2: results from a phase 2 study in 51 patients with metastasized melanoma. *Cancer*. **116**, 4139–4146 (2010).
117. L. Mortara, E. Balza, A. Bruno, A. Poggi, P. Orecchia, B. Carnemolla, Anti-cancer therapies employing IL-2 cytokine tumor targeting: Contribution of innate, adaptive and immunosuppressive cells in the anti-tumor efficacy. *Front. Immunol.* **9**, 2905 (2018).
118. K. D. Orcutt, J. J. Rhoden, B. Ruiz-Yi, J. V. Frangioni, K. Dane Wittrup, Effect of Small-Molecule–Binding Affinity on Tumor Uptake In Vivo: A Systematic Study Using a Pretargeted Bispecific Antibody. *Mol. Cancer Ther.* **11**, 1365–1372 (2012).
119. G. Sgouros, L. Bodei, M. R. McDevitt, J. R. Nedrow, Radiopharmaceutical therapy in cancer: clinical advances and challenges. *Nat. Rev. Drug Discov.* **19**, 589–608 (2020).
120. L. Bloom, K. C. Ingham, R. O. Hynes, Fibronectin regulates assembly of actin filaments and focal contacts in cultured cells via the heparin-binding site in repeat III13. *Mol. Biol. Cell*. **10**, 1521–1536 (1999).
121. J. H. Peters, J. E. Trevithick, P. Johnson, R. O. Hynes, Expression of the Alternatively Spliced EIIIB Segment of Fibronectin. *Cell Adhes. Commun.* **3**, 67–89 (1995).
122. J. A. Van Deventer, K. D. Wittrup, Yeast surface display for antibody isolation: library construction, library screening, and affinity maturation. *Methods Mol. Biol.* **1131**, 151–181 (2014).
123. A. Angelini, T. F. Chen, S. de Picciotto, N. J. Yang, A. Tzeng, M. S. Santos, J. A. Van Deventer, M. W. Traxlmayr, K. D. Wittrup, Protein Engineering and Selection Using Yeast Surface Display. *Methods Mol. Biol.* **1319**, 3–36 (2015).
124. M. Schoof, B. Faust, R. A. Saunders, S. Sangwan, V. Rezelj, N. Hoppe, M. Boone, C. B. Billesbølle, C. Puchades, C. M. Azumaya, H. T. Kratochvil, M. Zimanyi, I. Deshpande, J. Liang, S. Dickinson, H. C. Nguyen, C. M. Chio, G. E. Merz, M. C. Thompson, D. Diwanji, K. Schaefer, A. A. Anand, N. Dobzinski, B. S. Zha, C. R. Simoneau, K. Leon, K. M. White, U. S. Chio, M. Gupta, M. Jin, F. Li, Y. Liu, K. Zhang, D. Bulkley, M. Sun, A. M. Smith, A. N. Rizo, F. Moss, A. F. Brilot, S. Pourmal, R. Trenker, T. Pospiech, S. Gupta, B. Barsi-Rhyne, V. Belyy, A. W. Barile-Hill, S. Nock, Y. Liu, N. J. Krogan, C. Y. Ralston, D. L. Swaney, A. García-Sastre, M. Ott, M. Vignuzzi, QCRG Structural Biology Consortium, P. Walter, A. Manglik, An ultrapotent synthetic nanobody neutralizes SARS-CoV-2 by stabilizing inactive Spike. *Science*. **370**, 1473–1479 (2020).
125. C. P. Guimaraes, M. D. Witte, C. S. Theile, G. Bozkurt, L. Kundrat, A. E. M. Blom, H. L. Ploegh, Site-specific C-terminal and internal loop labeling of proteins using sortase-mediated reactions. *Nat. Protoc.* **8**, 1787–1799 (2013).
126. M. L. Broz, M. Binnewies, B. Boldajipour, A. E. Nelson, J. L. Pollack, D. J. Erle, A. Barczak, M. D. Rosenblum, A. Daud, D. L. Barber, S. Amigorena, L. J. Van't Veer, A. I. Sperling, D. M. Wolf, M. F. Krummel, Dissecting the tumor myeloid compartment reveals

rare activating antigen-presenting cells critical for T cell immunity. *Cancer Cell*. **26**, 638–652 (2014).
127. K.-P. Hopfner, V. Hornung, Molecular mechanisms and cellular functions of cGAS-STING signalling. *Nat. Rev. Mol. Cell Biol.* **21**, 501–521 (2020).
128. S.-R. Woo, M. B. Fuertes, L. Corrales, S. Spranger, M. J. Furdyna, M. Y. K. Leung, R. Duggan, Y. Wang, G. N. Barber, K. A. Fitzgerald, M.-L. Alegre, T. F. Gajewski, STING-dependent cytosolic DNA sensing mediates innate immune recognition of immunogenic tumors. *Immunity*. **41**, 830–842 (2014).
129. L. Sun, J. Wu, F. Du, X. Chen, Z. J. Chen, Cyclic GMP-AMP synthase is a cytosolic DNA sensor that activates the type I interferon pathway. *Science*. **339**, 786–791 (2013).
130. J. Wu, L. Sun, X. Chen, F. Du, H. Shi, C. Chen, Z. J. Chen, Cyclic GMP-AMP is an endogenous second messenger in innate immune signaling by cytosolic DNA. *Science*. **339**, 826–830 (2013).
131. J. Klarquist, C. M. Hennies, M. A. Lehn, R. A. Reboulet, S. Feau, E. M. Janssen, STING-mediated DNA sensing promotes antitumor and autoimmune responses to dying cells. *J. Immunol.* **193**, 6124–6134 (2014).
132. L. Corrales, L. H. Glickman, S. M. McWhirter, D. B. Kanne, K. E. Sivick, G. E. Katibah, S.-R. Woo, E. Lemmens, T. Banda, J. J. Leong, K. Metchette, T. W. Dubensky Jr, T. F. Gajewski, Direct activation of STING in the tumor microenvironment leads to potent and systemic tumor regression and immunity. *Cell Rep.* **11**, 1018–1030 (2015).
133. C. R. Ager, M. J. Reilley, C. Nicholas, T. Bartkowiak, A. R. Jaiswal, M. A. Curran, Intratumoral STING activation with T-cell checkpoint modulation generates systemic antitumor immunity. *Cancer Immunol. Res.* **5**, 676–684 (2017).
134. J. Le Naour, L. Zitvogel, L. Galluzzi, E. Vacchelli, G. Kroemer, Trial watch: STING agonists in cancer therapy. *Oncoimmunology*. **9**, 1777624 (2020).
135. W. Zhou, A. T. Whiteley, C. C. de Oliveira Mann, B. R. Morehouse, R. P. Nowak, E. S. Fischer, N. S. Gray, J. J. Mekalanos, P. J. Kranzusch, Structure of the human cGAS–DNA complex reveals enhanced control of immune surveillance. *Cell*. **174**, 300-311.e11 (2018).
136. E. Karayel, T. Bürckstümmer, M. Bilban, G. Dürnberger, S. Weitzer, J. Martinez, G. Superti-Furga, The TLR-independent DNA recognition pathway in murine macrophages: Ligand features and molecular signature. *Eur. J. Immunol.* **39**, 1929–1936 (2009).
137. X. Li, C. Shu, G. Yi, C. T. Chaton, C. L. Shelton, J. Diao, X. Zuo, C. C. Kao, A. B. Herr, P. Li, Cyclic GMP-AMP synthase is activated by double-stranded DNA-induced oligomerization. *Immunity*. **39**, 1019–1031 (2013).
138. D. B. Stetson, R. Medzhitov, Recognition of cytosolic DNA activates an IRF3-dependent innate immune response. *Immunity*. **24**, 93–103 (2006).
139. A.-M. Herzner, C. A. Hagmann, M. Goldeck, S. Wolter, K. Kübler, S. Wittmann, T. Gramberg, L. Andreeva, K.-P. Hopfner, C. Mertens, T. Zillinger, T. Jin, T. S. Xiao, E. Bartok, C. Coch, D. Ackermann, V. Hornung, J. Ludwig, W. Barchet, G. Hartmann, M. Schlee, Sequence-specific activation of the DNA sensor cGAS by Y-form DNA structures as found in primary HIV-1 cDNA. *Nat. Immunol.* **16**, 1025–1033 (2015).
140. F. Eckstein, Phosphorothioates, essential components of therapeutic oligonucleotides. *Nucleic Acid Ther.* **24**, 374–387 (2014).

141. S. H. Ku, S. D. Jo, Y. K. Lee, K. Kim, S. H. Kim, Chemical and structural modifications of RNAi therapeutics. *Adv. Drug Deliv. Rev.* **104**, 16–28 (2016).
142. C. Vanpouille-Box, J. A. Hoffmann, L. Galluzzi, Pharmacological modulation of nucleic acid sensors - therapeutic potential and persisting obstacles. *Nat. Rev. Drug Discov.* **18**, 845–867 (2019).
143. J. B. Ulmer, C. M. DeWitt, M. Chastain, A. Friedman, J. J. Donnelly, W. L. McClements, M. J. Caulfield, K. E. Bohannon, D. B. Volkin, R. K. Evans, Enhancement of DNA vaccine potency using conventional aluminum adjuvants. *Vaccine*. **18**, 18–28 (1999).
144. L. Andreeva, B. Hiller, D. Kostrewa, C. Lässig, C. C. de Oliveira Mann, D. Jan Drexler, A. Maiser, M. Gaidt, H. Leonhardt, V. Hornung, K.-P. Hopfner, cGAS senses long and HMGB/TFAM-bound U-turn DNA by forming protein–DNA ladders. *Nature*. **549**, 394–398 (2017).
145. F. Steinhagen, T. Zillinger, K. Peukert, M. Fox, M. Thudium, W. Barchet, C. Putensen, D. Klinman, E. Latz, C. Bode, Suppressive oligodeoxynucleotides containing TTAGGG motifs inhibit cGAS activation in human monocytes. *Eur. J. Immunol.* **48**, 605–611 (2018).
146. H. Lian, J. Wei, R. Zang, W. Ye, Q. Yang, X.-N. Zhang, Y.-D. Chen, Y.-Z. Fu, M.-M. Hu, C.-Q. Lei, W.-W. Luo, S. Li, H.-B. Shu, ZCCHC3 is a co-sensor of cGAS for dsDNA recognition in innate immune response. *Nat. Commun.* **9**, 3349 (2018).
147. P. J. Kranzusch, A. S.-Y. Lee, J. M. Berger, J. A. Doudna, Structure of human cGAS reveals a conserved family of second-messenger enzymes in innate immunity. *Cell Rep.* **3**, 1362–1368 (2013).
148. M. F. Laursen, E. Christensen, L. L. T. Degn, K. Jønsson, M. R. Jakobsen, R. Agger, E. Kofod-Olsen, CD11c-targeted delivery of DNA to dendritic cells leads to cGAS- and STING-dependent maturation. *J. Immunother.* **41**, 9–18 (2018).
149. K. M. Garland, J. C. Rosch, C. S. Carson, L. Wang-Bishop, A. Hanna, S. Sevimli, C. Van Kaer, J. M. Balko, M. Ascano, J. T. Wilson, Pharmacological activation of cGAS for cancer immunotherapy. *Front. Immunol.* **12**, 753472 (2021).
150. W. O. Hemphill, S. R. Simpson, M. Liu, F. R. Salsbury Jr, T. Hollis, J. M. Grayson, F. W. Perrino, TREX1 as a novel immunotherapeutic target. *Front. Immunol.* **12**, 660184 (2021).
151. W. Zhou, L. Mohr, J. Maciejowski, P. J. Kranzusch, cGAS phase separation inhibits TREX1-mediated DNA degradation and enhances cytosolic DNA sensing. *Mol. Cell*. **81**, 739-755.e7 (2021).
152. H. Konno, S. Yamauchi, A. Berglund, R. M. Putney, J. J. Mulé, G. N. Barber, Suppression of STING signaling through epigenetic silencing and missense mutation impedes DNA damage mediated cytokine production. *Oncogene*. **37**, 2037–2051 (2018).
153. K. W. Ng, E. A. Marshall, J. C. Bell, W. L. Lam, CGAS–STING and cancer: Dichotomous roles in tumor immunity and development. *Trends Immunol.* **39**, 44–54 (2018).